

# The LMT 2 millimeter receiver system (B4R). II. Science demonstration observations toward Orion-KL / OMC-1

Teppei YONETSU,<sup>1,\*</sup> Ryohei KAWABE,<sup>2,3</sup> Yuki YOSHIMURA,<sup>4</sup> Kotomi TANIGUCHI,<sup>2</sup> Yoshito SHIMAJIRI,<sup>2,5</sup> Omar Sergio ROJAS-GARCÍA,<sup>6</sup> Arturo I. GÓMEZ-RUIZ,<sup>6,7</sup> Takeshi SAKAI,<sup>8</sup> Kunihiro TANAKA,<sup>9</sup> Bunyo HATSUKADE,<sup>2,3,4</sup> Akio TANIGUCHI,<sup>10,11</sup> Yoichi TAMURA,<sup>11</sup> Tatsuya TAKEKOSHI,<sup>10</sup> Tai OSHIMA,<sup>2,3</sup> Kotaro KOHNO,<sup>4,12</sup> Masato HAGIMOTO,<sup>11</sup> David H. HUGHES,<sup>6</sup> F. Peter SCHLOERB,<sup>13</sup> David SÁNCHEZ-ARGÜELLES,<sup>6,7</sup> Kamal SOUCCAR,<sup>13</sup> Gopal NARAYANAN,<sup>13</sup> Min S. YUN,<sup>13</sup> Víctor GÓMEZ-RIVERA,<sup>6,14</sup> Iván RODRÍGUEZ-MONTOYA,<sup>6,7</sup> Edgar COLÍN-BELTRÁN,<sup>6,7</sup> Miguel CHÁVEZ DAGOSTINO,<sup>6</sup> Javier ZARAGOZA-CARDIEL,<sup>6,7</sup> Shinji FUJITA,<sup>15</sup> and Hiroyuki MAEZAWA<sup>1</sup>

<sup>1</sup>Department of Physics, Graduate School of Science, Osaka Metropolitan University, 1-1 Gakuen-cho, Naka-ku, Sakai, Osaka 599-8531, Japan

<sup>2</sup>National Astronomical Observatory of Japan, National Institutes of Natural Sciences, 2-21-1 Osawa, Mitaka, Tokyo 181-8588, Japan

<sup>3</sup>Graduate Institute for Advanced Studies, SOKENDAI, Osawa, Mitaka, Tokyo 181-8588, Japan

<sup>4</sup>Institute of Astronomy, Graduate School of Science, The University of Tokyo, 2-21-1 Osawa, Mitaka, Tokyo 181-0015, Japan

<sup>5</sup>Kyushu Kyoritsu University, 1-8 Jiyugaoka, Yahatanishi-ku, Kitakyushu, Fukuoka, Fukuoka 807-8585, Japan

<sup>6</sup>Instituto Nacional de Astrofísica, Óptica y Electrónica, Luis Enrique Erro 1, Tonantzintla C.P. 72840, Puebla, México

<sup>7</sup>Consejo Nacional de Ciencia y Tecnología, Av. Insurgentes Sur 1582, Col. Crédito Constructor, Demarcación Territorial Benito Juárez C.P. 03940, Ciudad de México, México

<sup>8</sup>Graduate School of Informatics and Engineering, The University of Electro-Communications, 1-5-1 Chofugaoka, Chofu, Tokyo 182-8585, Japan

<sup>9</sup>Department of Physics, Faculty of Science and Technology, Keio University, 3-14-1 Hiyoshi, Yokohama, Kanagawa 223-8522, Japan

<sup>10</sup>Kitami Institute of Technology, 165, Koen-cho, Kitami, Hokkaido 090-8507, Japan

<sup>11</sup>Department of Physics, Graduate School of Science, Nagoya University, Furocho, Chikusa-ku, Nagoya, Aichi 464-8602, Japan

<sup>12</sup>Research Center for the Early Universe, Graduate School of Science, The University of Tokyo, 7-3-1 Hongo, Bunkyo-ku, Tokyo 113-0033, Japan

<sup>13</sup>Department of Astronomy, University of Massachusetts, Amherst, MA 01003, USA

<sup>14</sup>Corporación Mexicana de Investigación en Materiales S.A. de C.V., México

<sup>15</sup>The Institute of Statistical Mathematics, 10-3 Midori-cho, Tachikawa, Tokyo, 190-8562, Japan

\*E-mail: s.t.yonetsu@omu.ac.jp

ORCID: 0000-0003-2386-7427, 0000-0002-8049-7525, 0000-0002-1413-1963, 0000-0003-4402-6475, 0000-0001-9368-3143, 0000-0003-1054-4637, 0000-0001-9395-1670, 0000-0003-4521-7492, 0000-0001-8153-1986, 0000-0001-6469-8725, 0000-0002-9695-6183, 0000-0003-4807-8117, 0000-0002-4124-797X, 0009-0005-5915-1035, 0000-0002-4052-2394, 0000-0001-8083-5814, , 0000-0002-7344-9920, 0000-0001-7915-5272, 0000-0002-4723-6569, 0000-0001-7095-7543, 0009-0003-9025-6121, , 0000-0002-0758-3160, , 0000-0001-8216-9800, 0000-0002-6375-7065, 0009-0007-6017-8395

## Abstract

We present the results of mapping and single-point spectral scans toward Orion-KL/OMC-1 performed as science demonstrations of a 2 mm superconductor-insulator-superconductor receiver, named the Band 4 Receiver (B4R), installed on the Large Millimeter Telescope (LMT), with a diameter of 50 m. To prove the capabilities of mapping and spectral scans with the B4R on the LMT, commissioning observations were conducted employing the On-The-Fly mapping technique toward Orion-KL/OMC-1, which covers a map size of  $5' \times 5'$ . These mapping observations were performed with two frequency settings providing 10 GHz in total (131.4–133.9 GHz and 145.1–147.6 GHz, 136.2–138.7 GHz and 149.9–152.4 GHz) with a frequency resolution of 76.293 kHz. In this study, we conducted spectral line identification analysis for the hot core and compact ridge regions in the Orion-KL with a beam size of  $11''$ – $12''$ . We detected nearly 400 emission lines and identified two recombination lines and 29 molecular species, including isotopologues, deuterated molecules, and vibrational excited states, despite the short integration time. These results of line detection are consistent with those of previous studies. The 29 molecular species include nitrogen (N)-bearing complex organic molecules (COMs) and oxygen (O)-bearing COMs. To demonstrate the capability of the B4R in astrochemistry, we conducted detailed analyses of column densities, rotational temperatures, and relative abundances with respect to  $\text{H}_2$  on two representative COMs, N-bearing  $\text{C}_2\text{H}_5\text{CN}$  and O-bearing  $\text{CH}_3\text{OCHO}$  in the central  $40'' \times 40''$  area of the map. The wide bandwidth of 10 GHz enabled the use of 8 and 34 emission lines, respectively. The spatial differences in the physical and chemical properties between the above two molecules were derived at a spatial resolution of  $\sim 12''$ . The B4R on the LMT was successfully demonstrated to be powerful for mapping and spectral scans and to have high potential for the

Received: 2024 December 16, Accepted: 2025 August 27

© 2024. Astronomical Society of Japan.

study of interstellar chemistry.

**Keywords:** astrochemistry — instrumentation: detectors — ISM: abundances — submillimeter: ISM

## 1 Introduction

A 2 mm band receiver plays an important role not only in determining the redshift ( $z$ ) of dusty star-forming galaxies (DSFGs) or submillimeter galaxies (SMGs) through synergy with a 3 mm band receiver (e.g., Bakx & Dannerbauer 2022) but also in astrochemistry. The interstellar medium or circumstellar shells host more than 300 molecular species<sup>1</sup>, including complex organic molecules (COMs), which are defined as carbon-containing species composed of six or more atoms (Herbst & van Dishoeck 2009). The 2 mm band, which covers molecular species of deuterated molecules (e.g.,  $\text{DCO}^+$ ,  $\text{N}_2\text{D}^+$ ,  $\text{DCN}$ , and  $\text{DNC}$ )<sup>2</sup> and many COMs, is a critical frequency band in astrochemistry (e.g., Ziurys & McGonagle 1993; Martin et al. 2006; Belloche et al. 2014).

The Band 4 Receiver (B4R), a 2 mm band superconductor-insulator-superconductor (SIS) receiver, was installed onto the Large Millimeter Telescope (LMT)-50 m situated at the summit of the Sierra Negra Mountain in Mexico at an altitude of 4600 m. We conducted the On-The-Fly (OTF) mapping observations toward the Orion Kleinmann-Low (Orion-KL) region (Kleinmann & Low 1967) at a distance of  $418 \pm 6$  pc (Kim et al. 2008) in the Orion molecular cloud-1 (OMC-1) to test the observational capabilities of the B4R on the LMT (Kawabe et al. 2024). We obtained demonstration maps with a spatial resolution of  $\sim 11''$ , covering an area of  $10' \times 10'$  in 2018, and  $5' \times 5'$  and  $1.5' \times 1.5'$  in 2019 (Kawabe et al. 2024; Taniguchi et al. 2024). The capability for the OTF mapping using the B4R on the LMT was successfully demonstrated, and high-quality maps covering large regions of major molecular lines (e.g., CS and  $\text{H}_2\text{CO}$ ) were obtained (Kawabe et al. 2024). Moreover, the B4R is capable of spectral scan observations over a wide frequency range, which makes it valuable and highly competitive in advancing molecular identification efforts and essential for understanding chemical reactions and enrichments. The spatial variation in the chemical and physical properties of COMs (e.g., column densities and rotational temperatures) is key to understanding interstellar chemistry and its variety. The Orion-KL region, which is rich in COMs, is one of the most suitable targets for testing the observational capabilities of the B4R on the LMT, such as spectral scans over the 2 mm band and physical and chemical analysis/studies based on mapping spectral scan data.

The Orion-KL region stands as a nearby high-mass star-forming region (HMSFR), harboring protostars, a compact H II region associated with Source I, infrared sources N and Becklin-Nuegebauer (BN) (Becklin & Neugebauer 1967), and dense cores known as the hot core (HC) and compact ridge (CR). The HC region is located close to the southeast of Source I and is presumed to be externally heated by Source I (Zapata et al. 2011). The CR region is located at a separate distance southwest of Source I. The existence of  $\text{H}_2\text{O}$  masers and  $\text{HCOOH}$  in the CR implies the presence of regions of interaction between the Orion-KL outflow and surrounding quiescent gas clouds (e.g., Genzel et al. 1981; Gaume et al. 1998; Liu et al. 2002). The Orion-KL region exhibits distinct chemical properties across its various sub-regions.

The spatial differences between nitrogen (N)-bearing and oxygen (O)-bearing COMs in the HC and CR have also been confirmed by observations toward Orion-KL using single-dish tele-

scopes and interferometers for line surveys and high-resolution imaging (e.g., Blake et al. 1987; Turner 1989; Turner 1991; Crockett et al. 2015; Liu et al. 2022; Widicus Weaver & Friedel 2012; Friedel & Widicus Weaver 2012; Feng et al. 2015; Tercero et al. 2018; Yamamoto 2016; Peng et al. 2013). The HC region is rich in N-bearing COMs, and the CR region is characterized by abundant O-bearing COMs. The presence of saturated O-bearing species suggests interactions between outflows and quiescent ambient molecular material (Blake et al. 1987). Meanwhile, among O-bearing COMs,  $\text{CH}_3\text{COCH}_3$  has a distribution similar to that of N-bearing COMs, unlike other O-bearing molecules such as  $\text{CH}_3\text{OCHO}$  (Widicus Weaver & Friedel 2012; Peng et al. 2013). Tercero et al. (2018) discussed the spatial distribution differences among O-bearing molecules, focusing on C-O-C and C-O-H bonds.

Observations and chemical modeling have been performed to investigate the origins responsible for the chemical differentiation of N- and O-bearing COMs. Suzuki et al. (2018) evaluated parameters that could influence chemical evolution using the NAUTILUS gas-grain chemical model (Ruaud et al. 2016). Simulations under different physical conditions (e.g., initial densities, warm-up speed, peak density, timescale of the collapsing phase, and peak temperature) revealed that different temperatures play a significant role, whereas the influence of other parameters is relatively minor. Under the assumption that the temperature structures and ages of the cores differ, the observed abundances of NGC 6334F (poor in N-bearing species) and G10.47+0.03 (rich in N-bearing species) were consistent with the chemical model. This suggests that both the different temperature structures inside the core and their evolutionary stages contributed to the observed molecular correlations (Suzuki et al. 2018). Furthermore, Garrod et al. (2022) incorporated nondiffusive reaction processes occurring on dust grain surfaces and within ice mantles into simulations based on the three-phase astrochemical model MAGICKAL (Garrod 2013). The observational results of the hot molecular core (HMC) G31.41+0.31, one of the HMSFRs (Mininni et al. 2023), were consistent within a factor of ten with the abundance ratios predicted by the final chemical models of Garrod et al. (2022). Garrod et al. (2022) suggested that the observed differences in the abundances of N- and O-bearing species may be related to the efficient formation of nitriles in the gas phase during and after ice mantle desorption. They also proposed that the possible duration of chemical reactions in the gas phase after desorption and the thermal history of each source play a significant role in determining its chemical characteristics.

Understanding the chemical differentiation between such N- and O-bearing COMs in the Orion-KL regions and other HMSFRs is also important for comprehending the formation environments and processes of molecules that are considered precursors to prebiotic molecules (e.g.,  $\text{HNCHCN}$  (Zaleski et al. 2013a; Rivilla et al. 2018),  $\text{NH}_2\text{CH}_2\text{CN}$  (Li et al. 2020; Manna & Pal 2022),  $\text{NH}_2\text{CH}_2\text{CH}_2\text{OH}$  (Rivilla et al. 2021), and  $\text{HOCOOH}$  (Sanz-Novo et al. 2023)). Therefore, to evaluate the spectral scan capability, we extracted spectra from the OTF mapping data for the HC and CR regions of Orion-KL, where differences in the abundances of N- and O-bearing COMs have been observed. In addition, we analyzed the spatial distribution of physical quantities to demonstrate the capability of resolving spatial distributions in mapping obser-

<sup>1</sup> <https://cdms.astro.uni-koeln.de/classic/molecules>

<sup>2</sup> <https://splatalogue.online>

vations. We used a  $5' \times 5'$  dataset in 2019 with wide frequency coverage for rotation diagram analysis (Turner 1991) to test the observational capabilities. In addition, observations of distant HMSFRs using interferometers and the nearby Orion-KL region using the B4R on the LMT-50 m have nearly equivalent spatial scales of angular resolution. A comparison of observations on the same spatial scales between distant and nearby objects is pivotal for elucidating the universality of the chemical and physical environments conducive to COMs formation.

This paper is organized as follows. We describe the B4R and report observations and data reductions in Section 2. Section 3 delves into the details of the line identification and the chemical analysis of  $\text{C}_2\text{H}_5\text{CN}$  (N-bearing) and  $\text{CH}_3\text{OCHO}$  (O-bearing). Section 4 presents a comparative analysis of our results with previous results of observations toward Orion-KL and other distant HMSFRs observed with single-dish telescopes and interferometers and discusses their implications. Finally, the main conclusions of this study are summarized in Section 5.

## 2 Observations and data reductions

### 2.1 Band 4 receiver (B4R)

The B4R is a 2 mm single-beam two-polarization heterodyne SIS receiver with 4 K-cooled two sideband (2SB) mixers designed based on the work of Asayama et al. (2014). It was installed in the receiver cabin of the LMT-50 m, marking the commencement of scientific operations (Hughes et al. 2020). The radio frequency (RF) and intermediate frequency (IF) ranges of the B4R are 125–163 GHz and 4–8 GHz, respectively. The receiver noise temperature ( $T_{\text{RX}}$ ) is below 60 K, satisfying the specifications of the Atacama Large Millimeter/submillimeter Array (ALMA) Band 4. The aperture efficiency was measured to be 48% to 33% for 130 to 160 GHz, which is in good agreement with previous measurements for other receivers installed on the LMT (Hughes et al. 2020; Kawabe et al. 2024). The sideband image rejection ratio surpassed 13 dB. Further details can be found in Kawabe et al. (2024).

### 2.2 Observations

This paper presents the results of mapping observations in the spectral line OTF mode conducted using the B4R/LMT-50 m from November 10 to November 29, 2019, encompassing a map size of  $5' \times 5'$  (Kawabe et al. 2024) for testing observational capabilities. Before the OTF observations, the focus, astigmatism, and pointing were corrected using the SiO maser of Orion-KL. The pointing drift between calibrations was typically 3–5'' under stable weather conditions (e.g., wind speed < 10 m/s) (Kawabe et al. 2024). Intensity calibration was performed using the chopper-wheel calibration method, and its accuracy is approximately 10%. The observations were conducted at two 2SB mode frequency settings (set A: 131.4–133.9 GHz and 145.1–147.6 GHz; set B: 136.2–138.7 GHz and 149.9–152.4 GHz). The beam sizes in full width at half maximum (FWHM) were 11.9'' and 10.9'' for set A, and 11.6'' and 10.6'' for set B, as listed in table 1. These beam sizes correspond to approximately 0.02 pc at the distance of Orion-KL ( $\sim 418$  pc; Kim et al. 2008). An eXtended bandwidth Fast Fourier Transform Spectrometer (XFFTS, Radiometer Physics GmbH Co.; Klein et al. 2012) was employed to achieve a frequency resolution of 76.293 kHz, corresponding to a velocity resolution of  $\sim 0.15$ – $0.17$  km/s (2.5 GHz and 32768 channel). The center coordinate of the observation field of view was

$(\alpha, \delta)_{\text{J2000.0}} = (5^{\text{h}}35^{\text{m}}14.^{\text{s}}16, -5^{\circ}22'21''.50)$ , with the OFF point located at  $(\alpha, \delta)_{\text{J2000.0}} = (5^{\text{h}}36^{\text{m}}15.^{\text{s}}50, -5^{\circ}02'34''.40)$ . The total on-source time was approximately 42 min with 3'' scan separations in each frequency set. The telescope elevation range was 65.97–58.84 degrees for set A and 66.05–60.42 degrees for set B, whereas the optical depth  $\tau_{225\text{ GHz}}$  was 0.22 for set A and 0.11 for set B. The system temperatures ( $T_{\text{SYS}}$ ) were measured to be 119 K for set A and 112 K for set B on average for both sidebands, respectively. These observation parameters (observed frequency range, main beam efficiency ( $\eta_{\text{MB}}$ ), beam size ( $\theta_{\text{beam}}$ , FWHM), telescope elevation range,  $\tau_{225\text{ GHz}}$ , and  $T_{\text{SYS}}$ ) for each frequency set are summarized in table 1.

### 2.3 Data reductions

We generated measurement sets from the raw B4R data using the B4R pipeline (b4rpipe), developed by our team<sup>3</sup>. Subsequently, we created FITS datacubes with a grid size of 3'' and a Gaussian grid function using the Common Astronomy Software Applications (CASA) package (The Casa Team et al. 2022).

In OTF observations, which require a relatively long time for mapping, a slight pointing offset can occur owing to the time interval before the next pointing calibration. In sets A and B observations, although pointing calibrations were performed using the SiO maser of Orion-KL before OTF observations, a slight pointing offset was identified in sets A and B OTF maps. By taking advantage of the wide bandwidth, which enables the simultaneous observation of multiple emission lines, it is possible to select the emission lines that are most suitable for pointing offset correction after observations. The procedure for pointing correction is as follows. The HDO and  $\text{HC}_3\text{N}$  ( $v_7 = 2$ ) emission lines were used to calibrate for the pointing offset. The offset relative to the HC was measured using the HDO line, in which the OTF maps showed a point-like distribution, as shown in figure 1. Because HDO is associated with nearly the HC region (e.g., Plambeck & Wright 1987; Neill et al. 2013), the peak coordinates were obtained from the integrated intensity map of the HDO (6(1,6)–5(2,3), upper-level energy  $E_u = 444.03\text{ K}^{4,5}$ ) in set B using 2D Gaussian fitting and then calibrated to the HC coordinates  $(\alpha, \delta)_{\text{J2000.0}} = (5^{\text{h}}35^{\text{m}}14.^{\text{s}}60, -5^{\circ}22'31''.00)$ . The coordinates of each substructure are summarized in table 2 with the CR, BN, and Source I. The calibration shift value for set B was  $(\Delta\alpha, \Delta\delta)_{\text{J2000.0}} = (0.^{\text{s}}455, 4''.811)$ . Then, by using the  $\text{HC}_3\text{N}$  ( $v_7 = 2$ ) emission lines, which are compact distributions and highly excited lines in both set A (16-15,  $l = 0$ ,  $E_u = 701.44\text{ K}^{4,6}$ ) and set B (15-14,  $l = 2f$ ,  $E_u = 697.69\text{ K}^{4,6}$ ), as shown in figure 1, we calibrated set A by matching  $\text{HC}_3\text{N}$  ( $v_7 = 2$ ) peaks coordinate to set B. The calibration shift value for set A was  $(\Delta\alpha, \Delta\delta)_{\text{J2000.0}} = (0.^{\text{s}}360, 9''.73)$ . From the error of the 2D Gaussian fitting and the slight offset between the peaks of HDO and the position of HC (e.g., Plambeck & Wright 1987; Neill et al. 2013), the accuracy of this pointing correction was estimated to be approximately 2–3''. This remained within approximately 30% of the beam size ( $\sim 11''$ ). The baseline calibration over the entire 2.5 GHz bandwidth was performed using the CASA imcontsub task, with a 5th-order polynomial function fitted to line-free channels selected by intensities below  $3\sigma$ .

The HC and CR spectral data were extracted by aver-

<sup>3</sup> <https://github.com/b4r-dev/b4rpipe>

<sup>4</sup> <https://splatalogue.online>

<sup>5</sup> <https://spec.jpl.nasa.gov/home.html>

<sup>6</sup> <https://cdms.astro.uni-koeln.de/classic/molecules>

**Table 1.** Observational parameters.

set	sideband	frequency [GHz]	$\eta_{\text{MB}}$	$\theta_{\text{beam}}$ FWHM["]	elevation range* [degrees]	$\tau_{225 \text{ GHz}}$	$T_{\text{SYS}}$ [K]	RMS [K] <sup>†</sup> (HC)	RMS [K] <sup>†</sup> (CR)
A	lower sideband (LSB)	131.4–133.9	0.69	11.9	65.97–58.84	0.22	119	0.31	0.29
	upper sideband (USB)	145.1–147.6	0.66	10.9				0.37	0.39
B	LSB	136.2–138.7	0.69	11.6	66.05–60.42	0.11	112	0.25	0.25
	USB	149.9–152.4	0.65	10.6				0.28	0.26

\* telescope elevation range. <sup>†</sup> root mean square (RMS) of noise level calculated from the spectra extracted from the HC and CR regions ( $T_{\text{MB}}$  scale, non-channel binning)

aging over circles with diameters corresponding to the each beam size in table 1 and centered on the HC at  $(\alpha, \delta)_{\text{J2000.0}} = (5^{\text{h}}35^{\text{m}}14^{\text{s}}.60, -5^{\circ}22'31''.00)$  and the CR at  $(\alpha, \delta)_{\text{J2000.0}} = (5^{\text{h}}35^{\text{m}}14^{\text{s}}.00, -5^{\circ}22'36''.90)$  (Feng et al. 2015) from maps corresponding to each frequency set. The root mean square (RMS) values of the noise level for the HC and CR ( $T_{\text{MB}}$  scale, non-channel binning) were calculated from spectral data, as shown in table 1.

**Table 2.** Coordinates of substructures.

Source	RA $\alpha_{\text{J2000}}$	Dec $\delta_{\text{J2000}}$	Reference*
HC	$5^{\text{h}}35^{\text{m}}14^{\text{s}}.60$	$-5^{\circ}22'31''.00$	(1)
CR	$5^{\text{h}}35^{\text{m}}14^{\text{s}}.00$	$-5^{\circ}22'36''.90$	(1)
BN	$5^{\text{h}}35^{\text{m}}14^{\text{s}}.11$	$-5^{\circ}22'22''.70$	(2)
Source I	$5^{\text{h}}35^{\text{m}}14^{\text{s}}.51$	$-5^{\circ}22'30''.53$	(3)

\* (1) (Feng et al. 2015); (2) (Beckwith et al. 1978); (3) (Menten & Reid 1995)

### 3 Results

#### 3.1 Line identification and OTF maps

Line identification was performed to test the observational capabilities of spectral scans using the eXtended CASA Line Analysis Software Suite (XCLASS) (Möller et al. 2017) and by referring to the splatalogue<sup>4</sup> database and previous studies. XCLASS refers to two molecular information databases, the Cologne Database for Molecular Spectroscopy (CDMS<sup>6</sup>) (Endres et al. 2016; Müller et al. 2001; Müller et al. 2005) and the Jet Propulsion Laboratory molecular databases (JPL<sup>5</sup>) (Pickett et al. 1998). We performed identifications with a detection threshold of  $3\sigma$  using 0.15–0.17 km/s resolution spectra (non-channel binning). In this analysis, as described in Section 2.3, spectra were extracted by averaging each beam size (table 1) centered on the HC and CR from maps. The effective angular resolution is degraded to approximately 1.4 times the original resolution. As a result, the spectra of HC and CR, which are separated by approximately  $11''$ , are slightly contaminated by each other. However, to perform line identification and evaluate the spatial resolution capability using spectra with improved signal-to-noise ratio (SNR), we adopted the beam size as the averaging region.

As a result, 404 emission lines are detected in the observed frequency ranges, as shown in figures 8–11 in the Appendix. In this study, molecules with more than two emission lines (i.e., two transitions) in the observation frequency ranges are defined as identified. On the other hand, molecules with only one emission line in the observation frequency ranges, with the exception of the recombination line, are defined as tentatively identified. Among the 404 emission lines, 337 lines corresponded to identified or tentatively identified lines. Among the remaining 67 lines, 16 lines were attributed to leakage from the second downconversion or aliasing

from the analog-to-digital converter (ADC) owing to the absence of anti-aliasing filters during this observation. In addition, two lines are ascribed to the leakage of stronger OCS and SO lines from the image sideband to the signal sideband. These 18 leakage emission lines were labeled as X-lines. The remaining 49 lines were labeled as unidentified lines (U-lines). Figures 8–11 and tables 6–8 in the Appendix show detailed information on the spectra of each frequency band, alongside the identified lines, tentatively identified lines, X-lines, and U-lines.

CS and  $\text{C}^{33}\text{S}$  were detected for only one line each. However, we classified them as identified because these lines exhibit sufficient intensity in figures 8–11 in the Appendix, which is consistent with previous studies (Tercero et al. 2010). In the spectra extracted from the HC and CR, only one transition (150.8519 GHz) of cyclic (*c*)- $\text{C}_3\text{H}_2$  was detected, excluding a transition that is blended with a U-line. However, the detection of this transition (150.8519 GHz) is consistent with that of Ziurys & McGonagle (1993), and other transitions (150.8207 GHz) buried in noise in the HC and CR were detected in different regions (e.g., regions west and north of the HC and CR) (Kawabe et al. 2024). Therefore, *c*- $\text{C}_3\text{H}_2$  was classified as an identified species. Second excited torsional states of  $\text{CH}_3\text{OCHO}$  ( $v_t = 2$ ) were identified through comparison with previous studies (Takano et al. 2012; Kobayashi et al. 2013). Consequently,  $\text{H}_3\text{S}\alpha$ ,  $\text{H}_5\text{I}\gamma$  and 29 molecular species, including isotopologues, deuterated molecules, and vibrational excited states, were identified ( $\text{NO}$ ,  $\text{CS}$ ,  $\text{C}^{33}\text{S}$ ,  $\text{SO}$ ,  $^{33}\text{SO}$ ,  $\text{SO}_2$  ( $v = 0, v_2 = 1$ ),  $^{34}\text{SO}_2$ ,  $^{33}\text{SO}_2$ ,  $\text{OCS}$ ,  $\text{O}^{13}\text{CS}$ ,  $\text{HDO}$ ,  $\text{HNCO}$ ,  $\text{H}_2\text{CO}$ ,  $\text{H}_2^{13}\text{CO}$ ,  $\text{H}_2\text{CS}$ , cyclic *c*- $\text{C}_3\text{H}_2$ ,  $\text{HC}_3\text{N}$  ( $v = 0, v_6 = 1, v_7 = 1, v_7 = 2$ ), *t*- $\text{HCOOH}$ ,  $\text{CH}_3\text{CN}$  ( $v = 0, v_8 = 1$ ),  $\text{CH}_3\text{OH}$  ( $v = 0$ ),  $^{13}\text{CH}_3\text{OH}$ ,  $\text{CH}_3\text{CHO}$ ,  $\text{CH}_3\text{CCH}$ ,  $\text{CH}_3\text{NCO}$ ,  $\text{C}_2\text{H}_3\text{CN}$ ,  $\text{CH}_3\text{OCHO}$  ( $v = 0, v_{18} = 1, v_t = 2$ ),  $\text{C}_2\text{H}_5\text{CN}$ ,  $\text{CH}_3\text{OCH}_3$ , and  $\text{CH}_3\text{COCH}_3$ ). A total of 12 molecular species, including excited states, were tentatively identified ( $\text{S}^{18}\text{O}$ ,  $\text{OC}^{33}\text{S}$ ,  $^{18}\text{OCS}$ ,  $^{18}\text{O}^{13}\text{CS}$ ,  $\text{SiS}$ ,  $\text{H}_2\text{C}^{34}\text{S}$ ,  $\text{H}^{13}\text{CCCN}$  ( $v = 0$ ),  $\text{H}(\text{C})\text{OCN}$ ,  $\text{CH}_2\text{DCN}$ ,  $\text{CH}_3^{13}\text{CN}$ ,  $\text{CH}_3\text{OH}$  ( $v_{12} = 1$ ), and  $\text{CH}_3^{18}\text{OH}$ ). The results are summarized in table 3.

O-bearing COMs ( $\text{CH}_3\text{OH}$  ( $v = 0$ ),  $^{13}\text{CH}_3\text{OH}$ ,  $\text{CH}_3\text{CHO}$ ,  $\text{CH}_3\text{OCHO}$  ( $v = 0, v_{18} = 1, v_t = 2$ ),  $\text{CH}_3\text{OCH}_3$ , and  $\text{CH}_3\text{COCH}_3$ ) and N-bearing COMs ( $\text{CH}_3\text{CN}$  ( $v = 0, v_8 = 1$ ),  $\text{C}_2\text{H}_5\text{CN}$ , and  $\text{C}_2\text{H}_3\text{CN}$ ) are detected, as shown in figure 8–11. Notably, N-bearing COMs, such as  $\text{C}_2\text{H}_5\text{CN}$ , exhibit a strong spectral intensity in the HC (blue line), whereas O-bearing COMs, such as  $\text{CH}_3\text{OCHO}$  ( $v = 0$ ) and  $\text{CH}_3\text{OCH}_3$ , exhibit a strong spectral intensity in the CR (red line), as shown in figure 2. Although the spectra of HC and CR are slightly contaminated by each other, the difference in the spectral intensity indicates that the chemical differences between the HC and CR regions are clearly resolved in these observations.

The integrated intensity maps of  $\text{C}_2\text{H}_5\text{CN}$  ( $v = 0$ ) and  $\text{CH}_3\text{OCHO}$  ( $v = 0$ ) are shown in figure 3. The RMSs of the map noise level are  $2.8 \text{ K km s}^{-1}$  and  $0.8 \text{ K km s}^{-1}$  for the observa-

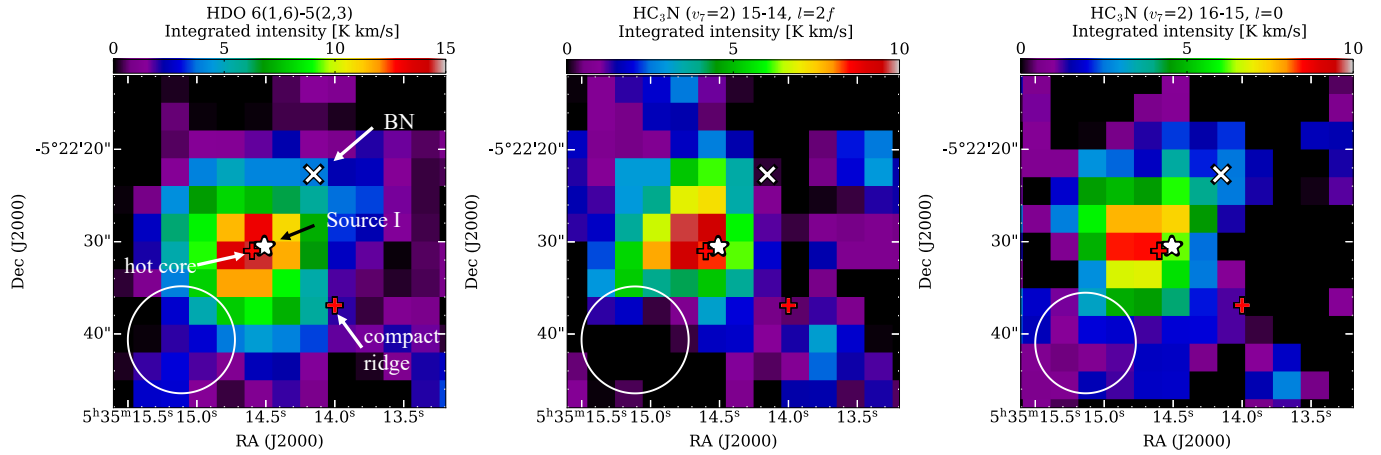


**Fig. 1.** Integrated intensity maps of HDO (left panel) and  $\text{HC}_3\text{N}$  ( $v_7 = 2$ ) (center) in the 136.2–138.7 GHz band and  $\text{HC}_3\text{N}$  ( $v_7 = 2$ ) (right) in the 146.1–147.6 GHz band, after correcting for the main beam efficiency and pointing. The velocity ranges of integrals are  $-5.8$ – $22$   $\text{km s}^{-1}$ ,  $-23$ – $11$   $\text{km s}^{-1}$ , and  $-2.3$ – $22$   $\text{km s}^{-1}$ , respectively. The red cross (+) denotes the hot core and compact ridge. The white cross (x) and star indicate the position of BN and Source I, respectively. The coordinates of each substructure are summarized in table 2. The lower left circle in each panel denotes the beam size in table 1. Alt text: The integrated intensity maps of the three panels. The x axis is the right ascension, and the y axis is the declination at the map size of approximately  $40'' \times 40''$ .

**Table 3.** Identified and tentatively identified species, including exited states.

Identified species and exited states*
$\text{H}35\alpha$ , $\text{H}51\gamma$ , NO, CS, $\text{C}^{33}\text{S}$ , SO, $^{33}\text{SO}$ , $\text{SO}_2$ ( $v = 0, v_2 = 1$ ), $^{34}\text{SO}_2$ , $^{33}\text{SO}_2$ , OCS, $\text{O}^{13}\text{CS}$ , HDO, HNC, $\text{H}_2\text{CO}$ , $\text{H}_2^{13}\text{CO}$ , $\text{H}_2\text{CS}$ , $c\text{-C}_3\text{H}_2$ , $\text{HC}_3\text{N}$ ( $v = 0, v_6 = 1, v_7 = 1, v_7 = 2$ ), $t\text{-HCOOH}$ , $\text{CH}_3\text{CN}$ ( $v = 0, v_8 = 1$ ), $\text{CH}_3\text{OH}$ ( $v = 0$ ), $^{13}\text{CH}_3\text{OH}$ , $\text{CH}_3\text{CHO}$ , $\text{CH}_3\text{NCO}$ , $\text{CH}_3\text{CCH}$ , $\text{C}_2\text{H}_3\text{CN}$ , $\text{CH}_3\text{OCHO}$ ( $v = 0, v_{18} = 1, v_t = 2$ ), $\text{C}_2\text{H}_5\text{CN}$ , $\text{CH}_3\text{OCH}_3$ , $\text{CH}_3\text{COCH}_3$
Tentatively identified species and exited states†
$\text{S}^{18}\text{O}$ , $\text{OC}^{33}\text{S}$ , $^{18}\text{OCS}$ , $^{18}\text{O}^{13}\text{CS}$ , SiS, $\text{H}_2\text{C}^{34}\text{S}$ , $\text{H}^{13}\text{CCCN}$ ( $v = 0$ ), $\text{H}(\text{C})\text{OCN}$ , $\text{CH}_2\text{DCN}$ , $\text{CH}_3^{13}\text{CN}$ , $\text{CH}_3\text{OH}$ ( $v_{12} = 1$ ), $\text{CH}_3^{18}\text{OH}$

\* Species or exited states with more than two detections of the emission lines in the observation frequency ranges. † Species or exited states with only one detection of the emission lines in the observation frequency ranges, except the recombination line.

tion settings A and B, respectively. The distributions of  $\text{C}_2\text{H}_5\text{CN}$  ( $v = 0$ ) and  $\text{CH}_3\text{OCHO}$  ( $v = 0$ ) are different.  $\text{C}_2\text{H}_5\text{CN}$  exhibit a peak near the HC, whereas  $\text{CH}_3\text{OCHO}$  exhibit a peak between the HC and CR, as shown in figure 3. The differences in the spectral intensity and the spatial distribution shown in figures 2 and 3 are consistent with those in previous studies (e.g., Feng et al. 2015; Friedel & Widicus Weaver 2012; Tercero et al. 2018) and indicate that the B4R installed on the LMT-50 m can distinguish between the N-bearing COM-rich HC and O-bearing COM-rich CR.

### 3.2 Chemical analysis of $\text{C}_2\text{H}_5\text{CN}$ and $\text{CH}_3\text{OCHO}$

As shown in figure 2, the difference in spectral intensity between N- and O-bearing COMs suggests their spatial segregation across our two regions of interest.  $\text{C}_2\text{H}_5\text{CN}$  and  $\text{CH}_3\text{OCHO}$  are representative N- and O-bearing COMs that have been observed not only in the Orion-KL region but also in distant HMSFRs (e.g., Coletta et al. 2020; Bonfand et al. 2017; Bonfand et al. 2019). In addition,

these lines do not seem to be strongly blended with other molecular lines in our observational data. Therefore, we visualized the spatial distributions as the maps of column densities and rotational temperatures of  $\text{C}_2\text{H}_5\text{CN}$  and  $\text{CH}_3\text{OCHO}$  using the rotation diagram method (Turner 1991) with the advantage of the B4R on the LMT in terms of spatial resolution (i.e., beam size  $\sim 11$ – $12''$ ). The application of the rotation diagram method to maps has also been reported by Bell et al. (2014). The following equations were used in this calculation.

$$\log_{10} \left[ \frac{3kW}{(8\pi^3\nu S\mu^2 g_{\text{I}} g_{\text{K}})} \right] = \log_{10} \left[ \frac{N}{Q(T_{\text{rot}})} \right] - E_{\text{u}} \frac{\log_{10} e}{T_{\text{rot}}}, \quad (1)$$

$$Q(T_{\text{rot}} : \text{C}_2\text{H}_5\text{CN}) = \left[ \frac{\pi(kT_{\text{rot}})^3}{h^3 ABC} \right]^{1/2}, \quad (2)$$

$$Q(T_{\text{rot}} : \text{CH}_3\text{OCHO}) = 2 \left[ \frac{\pi(kT_{\text{rot}})^3}{h^3 ABC} \right]^{1/2}, \quad (3)$$

where  $W$ ,  $\nu$ ,  $k$ ,  $h$ ,  $\mu$ ,  $S$ ,  $E_{\text{u}}$ ,  $g_{\text{I}}$ ,  $g_{\text{K}}$ ,  $N$ ,  $Q$ , and  $T_{\text{rot}}$  represent the integrated intensity, frequency, Boltzmann constant, Planck constant, dipole moment, line strength, upper-level energy, nuclear spin degeneracy,  $K$ -level degeneracy, column density, partition function, and rotational temperature, respectively.  $A$ ,  $B$ , and  $C$  in equations (2) and (3) indicate the rotational constants for the three principal axes of each molecule.

To apply the rotation diagram method to the maps, we used the spectra of  $\text{C}_2\text{H}_5\text{CN}$  and  $\text{CH}_3\text{OCHO}$  extracted by averaging each beam size at the HC and CR (Section 3.1) as a reference. In this reference spectrum, transitions with a spectral intensity of more than  $4\sigma$  in both the HC and CR regions, and that are not blended with other emission lines, were used in the calculations for all pixels.  $\text{CH}_3\text{OCHO}$  has two types of rotational transitions, ground torsional states ( $v = 0$ ) and first excited torsional states ( $v_{18} = 1$ ), in the emission lines above  $4\sigma$ . Therefore, calculations were performed using only the ground torsional state ( $v = 0$ ) and both torsional states ( $v = 0$  and  $v_{18} = 1$ ). Consequently, 8  $\text{C}_2\text{H}_5\text{CN}$ , 25  $\text{CH}_3\text{OCHO}$  ( $v = 0$ ), and 34  $\text{CH}_3\text{OCHO}$  ( $v = 0$  and  $v_{18} = 1$ ) transitions were used in this calculation. The degeneracies of  $\text{C}_2\text{H}_5\text{CN}$  are  $g_{\text{I}} = g_{\text{K}} = 1$ . Both A- and E-type transitions were observed

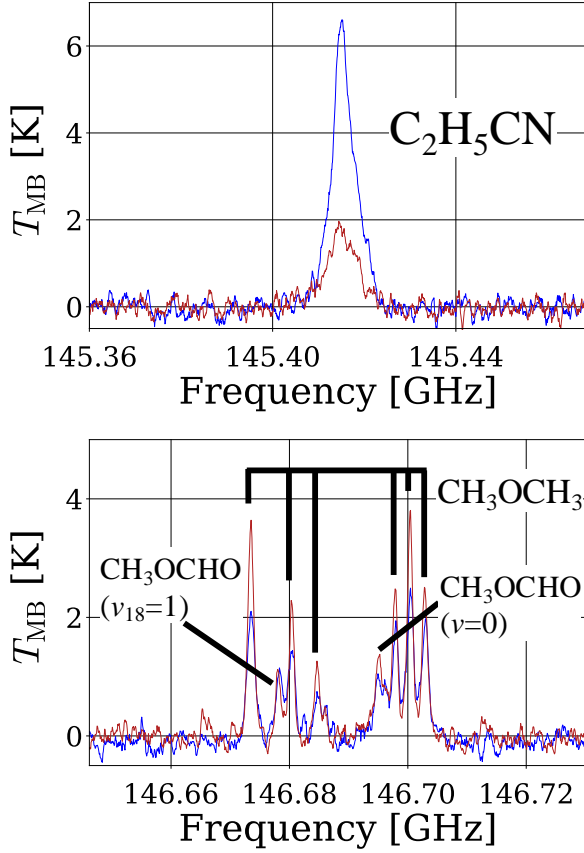


**Fig. 2.** Spectra of  $\text{C}_2\text{H}_5\text{CN}$ ,  $\text{CH}_3\text{OCHO}$  ( $v=0$ ,  $v_{18}=1$ ), and  $\text{CH}_3\text{OCH}_3$  in the 145.1–147.6 GHz band. The blue and red lines represent spectra with 10-channel binning, averaging in circles with diameters corresponding to the beam size of  $10.9''$  centered at the HC and CR (Feng et al. 2015), respectively. Alt text: The molecular emission line spectra of the two panels. The x axis is the frequency in gigahertz, and the y axis is the intensity at kelvin on the  $T_{\text{MB}}$  scale.

for  $\text{CH}_3\text{OCHO}$ .  $g_{\text{I}} = 2$  and  $g_{\text{K}} = 1$  for A-type transitions, whereas  $g_{\text{I}} = 1$  and  $g_{\text{K}} = 2$  for E-type transitions (Turner 1991). In this study, both A- and E-type transitions were used together for fitting; thus, the column density includes contributions from both types. The formulation of  $Q$  (equations (2) and (3)) was adopted from Turner (1991). Because  $\text{CH}_3\text{OCHO}$  has A- and E-type transitions, the partition function of  $\text{CH}_3\text{OCHO}$  (equation (3)) is multiplied by 2. The values of  $A$ ,  $B$ , and  $C$  were obtained from Fukuyama et al. (1996) for  $\text{C}_2\text{H}_5\text{CN}$  and from Karakawa et al. (2001) for  $\text{CH}_3\text{OCHO}$ . The values of  $\nu$ ,  $S\mu^2$ , and  $E_{\text{u}}$  were obtained from the JPL database. The integrated intensity maps calculated from the OTF observations of 8  $\text{C}_2\text{H}_5\text{CN}$  lines and 34  $\text{CH}_3\text{OCHO}$  ( $v=0$  and  $v_{18}=1$ ) lines, which have intensities above  $4\sigma$  in the spectra extracted by averaging each beam size at the HC and CR, were fitted pixel-by-pixel using equation (1), resulting in maps of  $N$  and  $T_{\text{rot}}$ . The beam size of these maps was aligned to  $12''$  using CASA.

The relative abundances with respect to  $\text{H}_2$  ( $X = N/N(\text{H}_2)$ ) were calculated. The values of  $N(\text{H}_2)$  are acquired from the FITS maps reported by Schuller et al. (2021). The  $N(\text{H}_2)$  map has an angular resolution of  $8''$ . This map was calculated using SPIRE 160, 250, 350, and  $500 \mu\text{m}$  data from the Herschel Gould Belt Survey (André et al. 2010) and ArTéMiS 350 and  $450 \mu\text{m}$

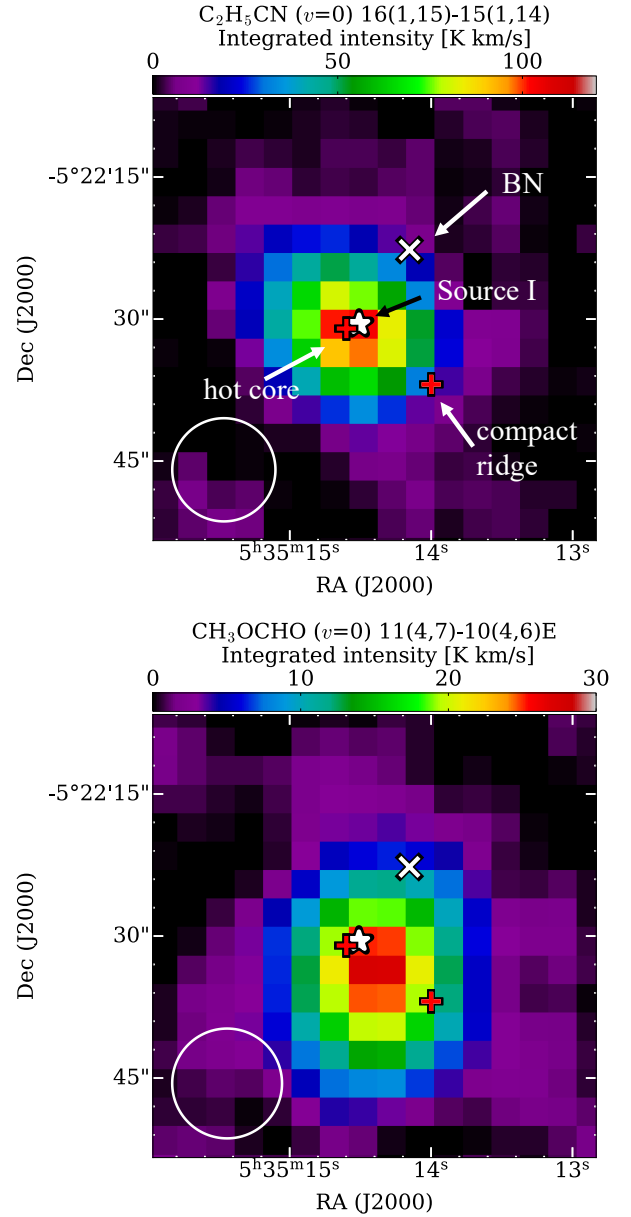


**Fig. 3.** Integrated intensity maps of  $\text{C}_2\text{H}_5\text{CN}$  ( $v=0$ ) (upper panel) in the 145.1–147.6 GHz band and  $\text{CH}_3\text{OCHO}$  ( $v=0$ ) (lower) in the 136.2–138.7 GHz band, after correcting for the main beam efficiency and pointing. The velocity ranges of integrals are  $-40$ – $40 \text{ km s}^{-1}$  and  $0$ – $20 \text{ km s}^{-1}$ , respectively. The various sources indicated on each map are described in figure 1 and table 2. The lower left circle in each panel denotes the beam size in table 1. Alt text: Integrated intensity maps of the two panels. The x axis is the right ascension, and the y axis is the declination at the map size of approximately  $40'' \times 40''$ .

data. Previous studies (e.g., Suzuki et al. 2018; Suzuki et al. 2016; Comito et al. 2005) have shown that assuming a conservative  $10''$  source size is an effective method for estimating the relative abundances, because the results agree well with other previous studies within the margin of error. In this study, we also assumed a  $10''$  source size to compare with the results of Suzuki et al. (2018) and to evaluate the observational capability of the B4R on the LMT-50 m. In addition to  $N$ ,  $T_{\text{rot}}$ , and  $X$ , which were calculated from data with a beam size of  $12''$ ,  $N'$ ,  $T'_{\text{rot}}$ , and  $X'$  in the

HC and CR were calculated assuming a source size of  $10''$  based on Suzuki et al. (2018). We adjusted the beam size of the  $N(\text{H}_2)$  map from  $8''$  to  $12''$  and  $10''$  using CASA and calculated the  $1\sigma$  error from the standard deviations of  $12''$  and  $10''$ . The  $N(\text{H}_2)$  values in the HC and CR regions are  $(5.5 \pm 0.1) \times 10^{23} \text{ cm}^{-2}$  and  $(4.0 \pm 0.2) \times 10^{23} \text{ cm}^{-2}$ , at  $12''$ , respectively. At  $10''$ , the  $N(\text{H}_2)$  values in the HC and CR regions are  $(5.8 \pm 0.1) \times 10^{23} \text{ cm}^{-2}$  and  $(4.1 \pm 0.3) \times 10^{23} \text{ cm}^{-2}$ , respectively. The maps of  $N$ ,  $T_{\text{rot}}$ , and  $X$  for  $\text{C}_2\text{H}_5\text{CN}$  and  $\text{CH}_3\text{OCHO}$  ( $v = 0$  and  $v_{18} = 1$ ) are shown in figure 4, whereas the rotation diagram plots for the HC and CR are shown in figure 5. The column density, the rotational temperature, and the relative abundance maps are masked above the maximum around the HC and CR, as shown in figure 4. The  $1\sigma$  noise of  $W$  is expressed as error bars in the rotation diagram plots (figure 5). The  $N$ ,  $T_{\text{rot}}$ ,  $X$ ,  $N'$ ,  $T'_{\text{rot}}$ , and  $X'$  values in the HC and CR regions of  $\text{C}_2\text{H}_5\text{CN}$ ,  $\text{CH}_3\text{OCHO}$  ( $v = 0$ ), and  $\text{CH}_3\text{OCHO}$  ( $v = 0$  and  $v_{18} = 1$ ) are listed in table 4. In table 4, we show the fitting results for only the 25  $\text{CH}_3\text{OCHO}$  ( $v = 0$ ) transitions as well as the fitting results using data for 34  $\text{CH}_3\text{OCHO}$  ( $v = 0$  and  $v_{18} = 1$ ) transitions. The errors in  $N$ ,  $T_{\text{rot}}$ ,  $N'$ , and  $T'_{\text{rot}}$  were calculated from the  $1\sigma$  error obtained by fitting, considering error propagation and adding 10% of the main values as the absolute calibration error. The errors in  $N$  and  $N'$  also take into account the uncertainty of the rotation temperature in the calculation of the partition function.

Figure 4 shows that the  $X(\text{C}_2\text{H}_5\text{CN})$  and  $X(\text{CH}_3\text{OCHO})$  of Orion-KL observed at the  $0.02 \text{ pc}$  scale differs between the HC and the CR, indicating that the difference is not due to the total gas abundance but to the chemical properties.  $X(\text{C}_2\text{H}_5\text{CN})$  shows a maximum near the HC and is approximately four times stronger than that observed in the CR.  $X(\text{CH}_3\text{OCHO})$  shows a peak in the region between the HC and CR. In addition,  $X(\text{C}_2\text{H}_5\text{CN})$  has a compact distribution, whereas  $X(\text{CH}_3\text{OCHO})$  has a more extended distribution in figure 4. Although previous studies (e.g., Suzuki et al. 2018; Feng et al. 2015) have determined the temperatures in specific regions, such as the HC and CR, the temperature map in figure 4 shows the continuous temperature distributions in COMs around the HC and CR, as shown in the temperature maps of  $\text{CH}_3\text{CN}$  reported by Bell et al. (2014). Figure 4 shows a broad distribution at approximately  $100 \text{ K}$  for the  $T_{\text{rot}}$  of  $\text{CH}_3\text{OCHO}$ ; however, it shows that a high-temperature region exists northeast of the HC for the  $T_{\text{rot}}$  of  $\text{C}_2\text{H}_5\text{CN}$ , i.e.,  $\text{CH}_3\text{OCHO}$  and  $\text{C}_2\text{H}_5\text{CN}$  have different temperature distributions.

## 4 Discussion

### 4.1 Comparison of line identification with previous studies

Sulfur oxide molecules and sulfur carbon chain molecules, such as  $\text{SO}_2$  ( $v = 0, v_2 = 1$ ),  $^{34}\text{SO}_2$ ,  $\text{SO}$ ,  $^{33}\text{SO}$ ,  $^{33}\text{SO}_2$ ,  $\text{O}^{13}\text{CS}$ ,  $\text{OCS}$ ,  $\text{H}_2\text{CS}$ ,  $\text{CS}$ , and  $\text{C}^{33}\text{S}$ , were identified. This identification is consistent with previous studies toward Orion-KL conducted at the Institut de radioastronomie millimétrique (IRAM)-30 m (Tercero et al. 2010; Esplugues et al. 2013).  $\text{S}^{18}\text{O}$ ,  $\text{OC}^{33}\text{S}$ ,  $^{18}\text{OCS}$ ,  $\text{H}_2\text{C}^{34}\text{S}$ , and  $\text{SiS}$  (silicon-bearing molecules) were labeled tentatively identified. However, their detection in previous studies toward Orion-KL (Tercero et al. 2010; Tercero et al. 2011; Esplugues et al. 2013) substantiates the reliability of our detection. The spectra of these molecules, excluding the tentative lines, are shown in figure 6.

Five lines that were unidentified in the Orion-KL region  $2 \text{ mm}$  band line survey by the Taeduk Radio Astronomy Observatory (TRAO)-14 m (Lee et al. 2001) and the Five College Radio

Astronomical Observatory (FCRAO)-14 m (Ziurys & McGonagle 1993), were identified in this study as  $\text{C}_2\text{H}_3\text{CN}$  ( $138.39516 \text{ GHz}$ ),  $\text{HC}_3\text{N}$  ( $v_7 = 1$ ) ( $146.1276387 \text{ GHz}$ ),  $\text{S}^{18}\text{O}$  ( $145.8738078 \text{ GHz}$ , tentatively identified),  $\text{CH}_3\text{OCH}_3$  ( $150.594406 \text{ GHz}$ ), and  $\text{CH}_3\text{OH}$  ( $v_{12} = 1$ ) ( $150.282794 \text{ GHz}$ , tentatively identified), as shown in figure 8–11. In addition, 162 previously undetected lines, with the exception of X-lines (Lee et al. 2001; Ziurys & McGonagle 1993) were newly detected, and 142 lines were identified in this study. The remaining 20 lines were labeled U-lines in this study. The line previously identified as  $\text{CH}_3\text{OCH}_3$  at  $150.4673 \text{ GHz}$  by Lee et al. (2001) was labeled a U-line in this study. Despite the short integration time, these results demonstrate the sufficient performance of the B4R receiver.

### 4.2 Comparison of chemical properties with results from previous studies

#### 4.2.1 Orion-KL

The  $N$ ,  $T_{\text{rot}}$ ,  $N'$ , and  $T'_{\text{rot}}$  values of  $\text{CH}_3\text{OCHO}$  ( $v = 0$ ) and  $\text{C}_2\text{H}_5\text{CN}$  in the HC (table 4) are consistent with the results from the Nobeyama Radio Observatory (NRO)-45 m centered nearly on the HC (assuming a source size of  $10''$ , Suzuki et al. 2018). Their  $X$  and  $X'$  values are lower than those reported by Suzuki et al. (2018). This is likely because the  $N(\text{H}_2)$  values used by Suzuki et al. (2018) were obtained from observations with a large beam size, leading to an underestimation of  $N(\text{H}_2)$ . All values of  $\text{CH}_3\text{OCHO}$  ( $v = 0$  and  $v_{18} = 1$ ) at the HC and CR are lower than those reported by Feng et al. (2015). This difference is expected because their observations were performed using an interferometer, which provided a smaller synthetic beam, approximately  $6'' \times 4''$  (Feng et al. 2015).

The distribution of  $\text{C}_2\text{H}_5\text{CN}$  centered around the HC resembles the integrated intensity maps obtained using interferometers, such as the Submillimeter Array (SMA), IRAM-30 m (Feng et al. 2015), and the Combined Array for Research in Millimeter-wave Astronomy (CARMA, Friedel & Widicus Weaver 2012). The distribution of  $\text{CH}_3\text{OCHO}$  extending between the HC and CR is consistent with the integrated intensity distributions obtained from the SMA and IRAM-30 m (Feng et al. 2015), ALMA (Tercero et al. 2018), and CARMA (Friedel & Widicus Weaver 2012). The existence of a high-temperature region northeast of the HC of  $T_{\text{rot}}$  in  $\text{C}_2\text{H}_5\text{CN}$  is similar to that in  $\text{CH}_3\text{CN}$  observed at IRAM-30 m (Bell et al. 2014). This high-temperature region traced by  $\text{CH}_3\text{CN}$  is thought to be caused by shock heating from northeast-southwest outflow gas (Plambeck et al. 2009), which originates from active star formation near IRc2 (Bell et al. 2014). In addition, the distributions of  $N$  and  $X$  in  $\text{C}_2\text{H}_5\text{CN}$ , which show a peak near the HC, are similar to the distributions of  $N$  and  $X$  in the map of  $\text{CH}_3\text{CN}$  reported by Bell et al. (2014). The formation process of  $\text{C}_2\text{H}_5\text{CN}$  on grains is related to  $\text{CH}_3\text{CN}$  (e.g., Garrod 2013; Garrod et al. 2017; Garrod et al. 2022), and shocks are considered the most plausible mechanism for releasing  $\text{C}_2\text{H}_5\text{CN}$  from dust grain surfaces (e.g., Friedel & Widicus Weaver 2012). The existence of a similar high-temperature region in  $\text{C}_2\text{H}_5\text{CN}$  and  $\text{CH}_3\text{CN}$ , as well as the similarity of the distributions of column density  $N$  and abundance  $X$ , which has a peak around the HC, reinforce the strength of the physical/chemical relationship between  $\text{C}_2\text{H}_5\text{CN}$  and  $\text{CH}_3\text{CN}$ .

#### 4.2.2 Other high-mass star-forming regions

COMs have been detected across various regions, and astrochemical studies, including N- and O-bearing COMs toward distant

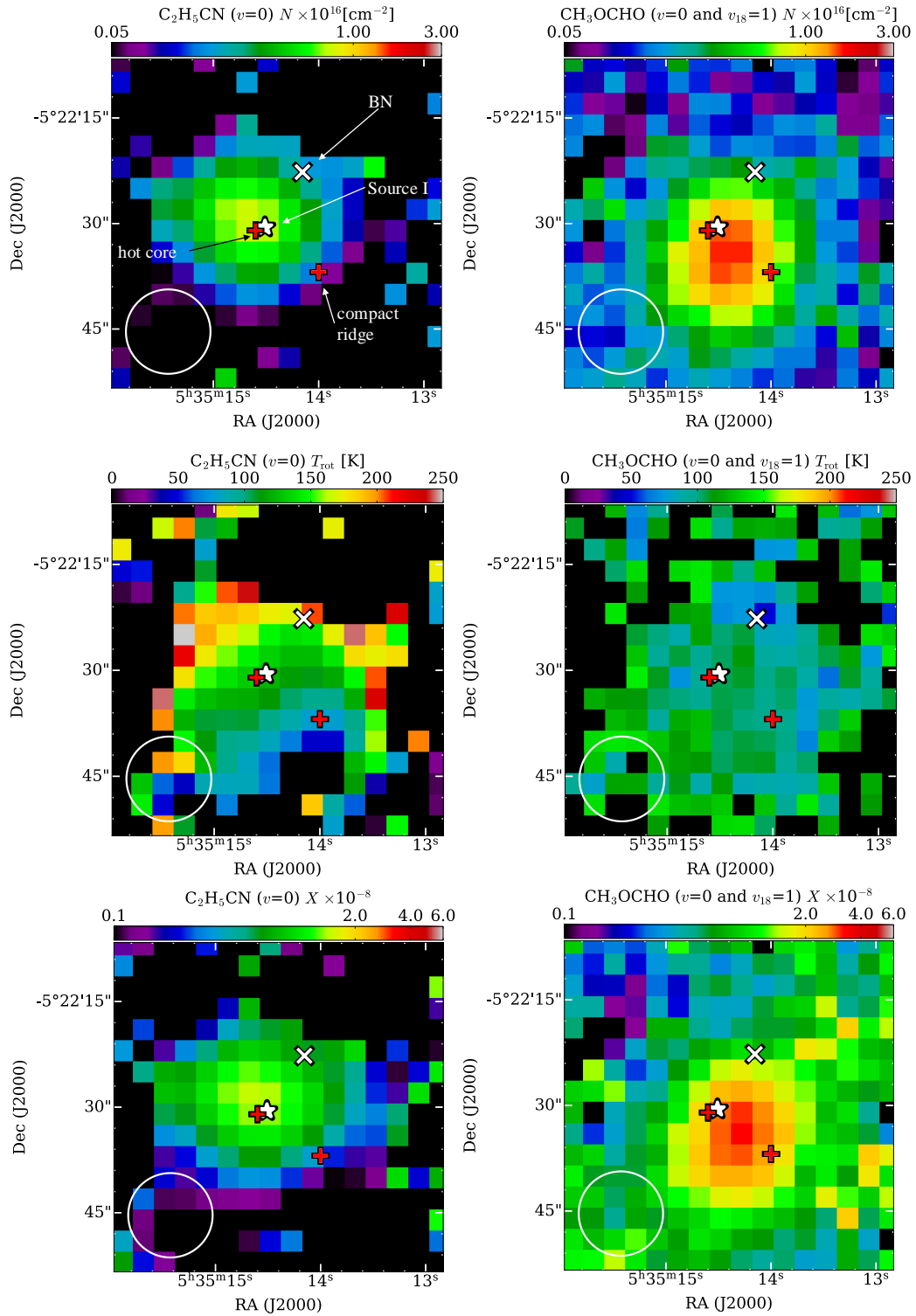


**Fig. 4.** Column density  $N$  (upper row), rotational temperature  $T_{rot}$  (middle), and relative abundance with respect to  $H_2$   $X$  (lower) maps of  $C_2H_5CN$  (left column) and  $CH_3OCHO$  ( $v=0$  and  $v_{18}=1$ ) (right). The various sources indicated on each map are described in figure 1 and table 2. The lower left circle in each panel denotes the beam size (12''). The column density, the rotational temperature, and the abundance maps are masked above the maximum around the HC and CR. Alt text: The column density, rotational temperature, and relative abundance with respect to  $H_2$  maps of the six panels. The x axis is the right ascension, and the y axis is the declination at map size of approximately  $40'' \times 40''$ .

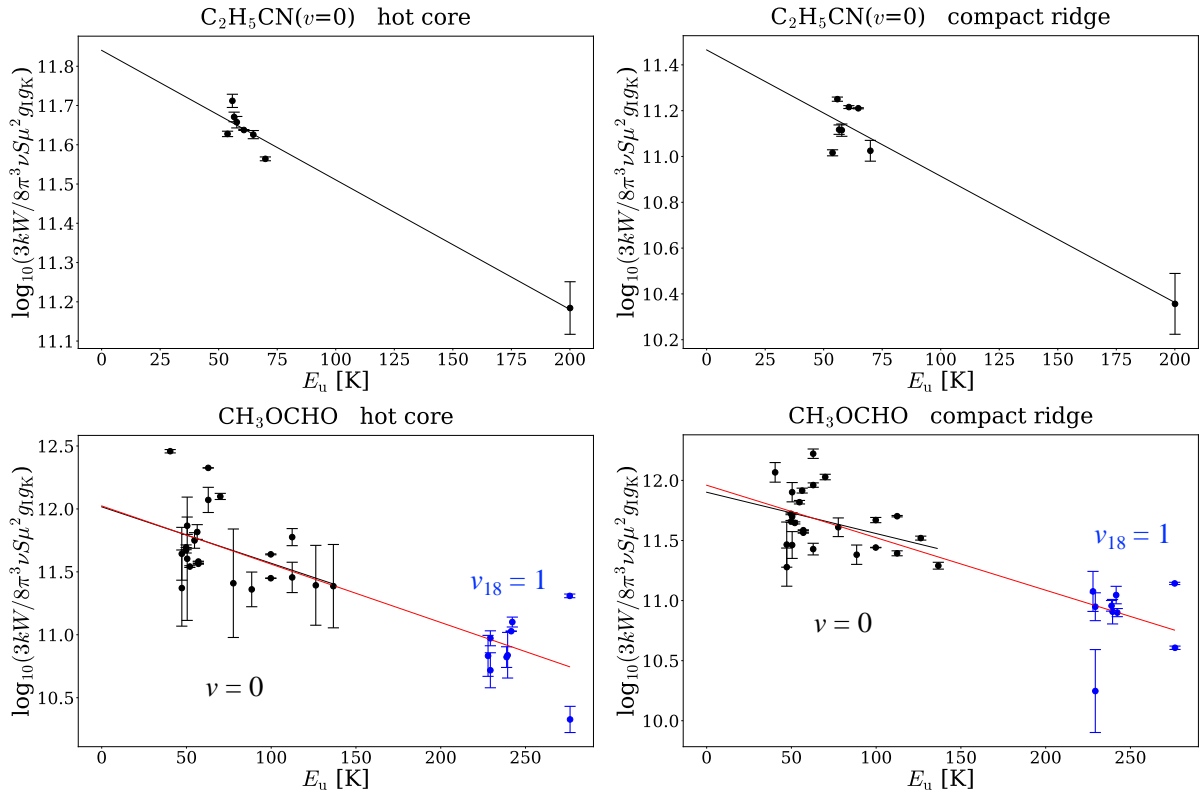


**Fig. 5.** Rotation diagram plots of  $\text{C}_2\text{H}_5\text{CN}$  and  $\text{CH}_3\text{OCHO}$  ( $v = 0$  and  $v_{18} = 1$ ) for the HC and CR ( $12''$ ). The error bars indicate the  $1\sigma$  noise of  $W$ . The upper panels show the plots of  $\text{C}_2\text{H}_5\text{CN}$ . In the lower panels, the black plots are  $\text{CH}_3\text{OCHO}$  ( $v = 0$ ) and the blue plots are  $\text{CH}_3\text{OCHO}$  ( $v_{18} = 1$ ). The black line shows the fitting result using only ( $v = 0$ ) states in each panel. The red line represents the fitting result using both torsional states  $\text{CH}_3\text{OCHO}$  ( $v = 0$  and  $v_{18} = 1$ ). Alt text: The rotation diagram plots of the four panels. The x axis is the upper-level energy at kelvin, and the y axis is the left side of equation (1).

**Table 4.** Column density, rotational temperature, and relative abundance with respect to  $\text{H}_2$  of  $\text{C}_2\text{H}_5\text{CN}$ ,  $\text{CH}_3\text{OCHO}$  ( $v = 0$ ), and  $\text{CH}_3\text{OCHO}$  ( $v = 0$  and  $v_{18} = 1$ ).

no source size assumptions ( $12''$ )	hot core (HC)			compact ridge (CR)		
	$N \times 10^{16}$ [cm $^{-2}$ ]	$T_{\text{rot}}$ [K]	$X \times 10^{-8}$	$N \times 10^{16}$ [cm $^{-2}$ ]	$T_{\text{rot}}$ [K]	$X \times 10^{-8}$
Species						
$\text{C}_2\text{H}_5\text{CN}$	0.8( $\pm 0.2$ )	132( $\pm 17$ )	1.4( $\pm 0.3$ )	0.1( $\pm 0.04$ )	79( $\pm 13$ )	0.4( $\pm 0.1$ )
$\text{CH}_3\text{OCHO}$ ( $v = 0$ )	1.1( $\pm 0.9$ )	97( $\pm 46$ )	2.0( $\pm 1.6$ )	1.3( $\pm 1.1$ )	126( $\pm 65$ )	3.1( $\pm 2.6$ )
$\text{CH}_3\text{OCHO}$ ( $v = 0$ and $v_{18} = 1$ )	1.1( $\pm 0.4$ )	94( $\pm 15$ )	1.9( $\pm 0.6$ )	1.0( $\pm 0.3$ )	99( $\pm 16$ )	2.5( $\pm 0.8$ )
assuming a source size ( $10''$ )	hot core (HC)			compact ridge (CR)		
	$N' \times 10^{16}$ [cm $^{-2}$ ]	$T'_{\text{rot}}$ [K]	$X' \times 10^{-8}$	$N' \times 10^{16}$ [cm $^{-2}$ ]	$T'_{\text{rot}}$ [K]	$X' \times 10^{-8}$
Species						
$\text{C}_2\text{H}_5\text{CN}$	1.1( $\pm 0.2$ )	132( $\pm 17$ )	1.9( $\pm 0.4$ )	0.2( $\pm 0.06$ )	79( $\pm 13$ )	0.5( $\pm 0.2$ )
$\text{CH}_3\text{OCHO}$ ( $v = 0$ )	1.6( $\pm 1.3$ )	97( $\pm 46$ )	2.7( $\pm 2.2$ )	1.8( $\pm 1.5$ )	126( $\pm 65$ )	4.4( $\pm 3.7$ )
$\text{CH}_3\text{OCHO}$ ( $v = 0$ and $v_{18} = 1$ )	1.5( $\pm 0.5$ )	94( $\pm 15$ )	2.6( $\pm 0.9$ )	1.4( $\pm 0.5$ )	99( $\pm 16$ )	3.5( $\pm 1.1$ )

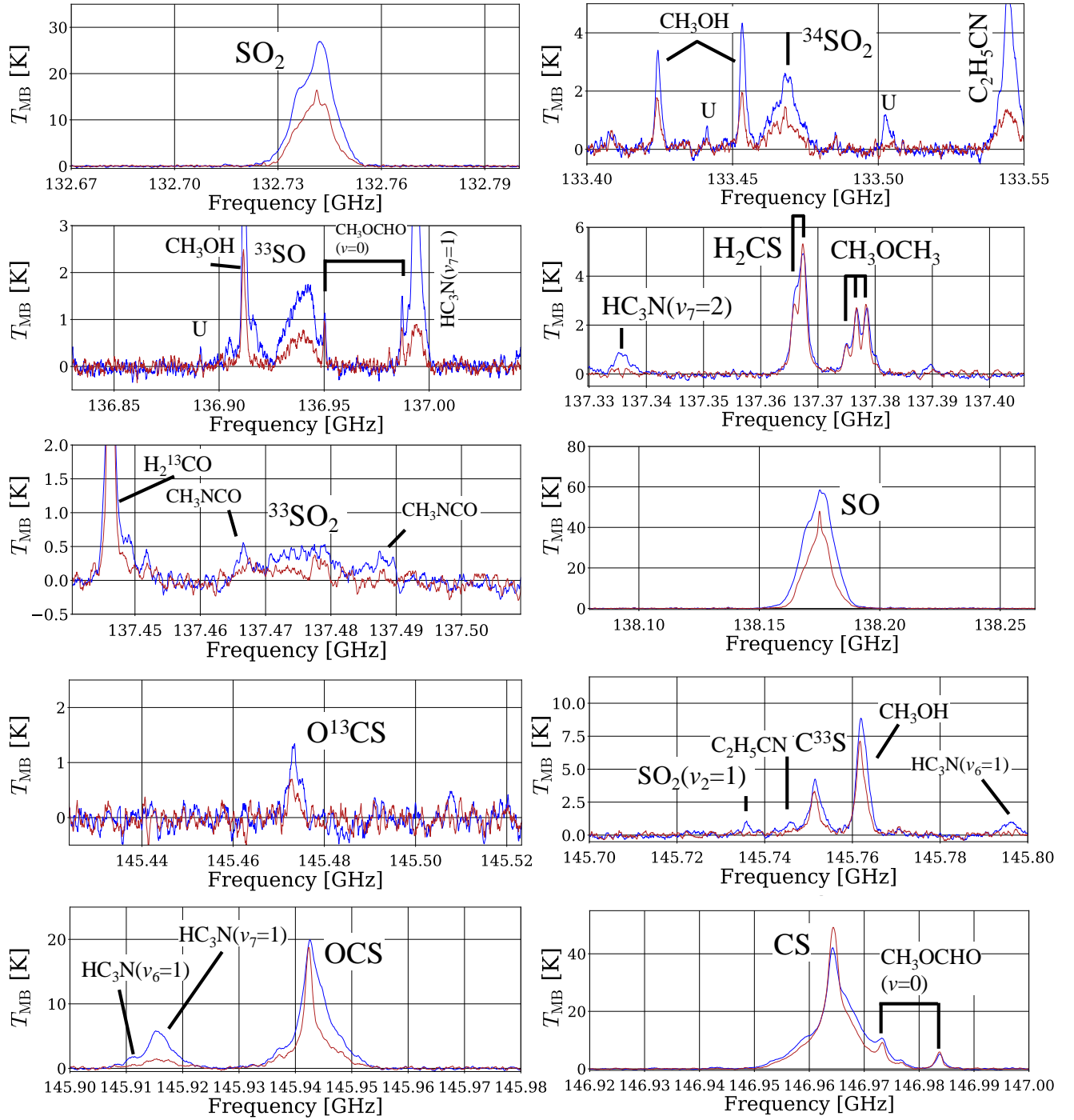


**Fig. 6.** Spectrum of sulfur oxide molecules and sulfur carbon chain molecules ( $\text{SO}_2$  ( $v = 0, v_2 = 1$ ),  $^{34}\text{SO}_2$ ,  $\text{SO}$ ,  $^{33}\text{SO}$ ,  $^{33}\text{SO}_2$ ,  $\text{O}^{13}\text{CS}$ ,  $\text{OCS}$ ,  $\text{H}_2\text{CS}$ ,  $\text{CS}$ , and  $\text{C}^{33}\text{S}$ ) with other lines. The blue and red lines represent spectra with 10-channel binning, averaging in circles with diameters corresponding to the beam size for each frequency band (table 1, 11–12'') centered at the HC and CR (Feng et al. 2015), respectively. Lines labeled with "U" denote undefined lines. Alt text: The molecular emission line spectra of the ten panels. The x axis is the frequency at gigahertz, and the y axis is the intensity at kelvin on the  $T_{\text{MB}}$  scale.

HMSFRs, such as Sgr B2(N) and G10.47+0.03, have been extended (e.g., McGuire 2022; Coletta et al. 2020; Bonfand et al. 2017; Bonfand et al. 2019; Qin et al. 2022; Li et al. 2020; Qin et al. 2015; Belloche et al. 2009; Manna & Pal 2023; Busch et al. 2024; Armijos-Abendaño et al. 2014; Rolffs et al. 2011; Mininni

et al. 2023; Zeng et al. 2018). Spatial distribution differences between N- and O-bearing COMs have been observed in some HMSFRs (e.g., Wyrowski et al. 1999; Kalenskii & Johansson 2010; Remijan et al. 2004; Zernickel et al. 2012; Allen et al. 2017; van der Walt et al. 2021; Peng et al. 2022; Mininni et al.

2023).

Figure 4 shows the differences in the distributions and abundances of  $\text{C}_2\text{H}_5\text{CN}$  and  $\text{CH}_3\text{OCHO}$  in the Orion KL region. The difference in spatial distributions between  $\text{C}_2\text{H}_5\text{CN}$  and  $\text{CH}_3\text{OCHO}$  was more pronounced when the spatial resolution was higher ( $\sim 2\text{--}6''$ ) as shown in previous interferometric observations (Feng et al. 2015; Friedel & Widicus Weaver 2012; Tercero et al. 2018). These results contrast with previous 2 mm band observations using the IRAM-30 m telescope, which revealed that  $X(\text{C}_2\text{H}_5\text{CN})$  and  $X(\text{CH}_3\text{OCHO})$  are strongly correlated for eight HMSFRs (18089-1732, G31.41+0.03, G24.78+0.08, W3(OH), G14.33-0.65, W51, G10.47+0.03, and G29.96-0.02) at distances of 2.0–8.9 kpc (Coletta et al. 2020). The beam size in the half power beam width (HPBW,  $\theta_{\text{beam}}$ ) of the IRAM-30 m in the 2 mm band was approximately  $16\text{--}18''$  (Coletta et al. 2020). This beam size corresponds to the spatial scale of the angular resolution ( $S_{\text{beam}}$  [pc]) of approximately 0.16–0.73 pc at distances of 2.0–8.9 kpc, and it is an order of magnitude larger than the 0.02 pc in this study. The beam size that Coletta et al. (2020) ( $16\text{--}18''$ ) used to calculate the column densities is smaller than that of the observation ( $\theta_{\text{H}_2}=20\text{--}60''$ ) used to calculate  $N(\text{H}_2)$  for calculating  $X$ . Therefore, Coletta et al. (2020) rescaled the column densities by  $(\theta_{\text{beam}}/\theta_{\text{H}_2})^2$  to match the spatial scales of  $N$  and  $N(\text{H}_2)$  when  $X$  was derived. Consequently, the apparent  $S_{\text{beam}}$  of  $X(\text{C}_2\text{H}_5\text{CN})$  and  $X(\text{CH}_3\text{OCHO})$  became even larger. We focused on  $S_{\text{beam}}$  to understand the significance of the correlation between  $X(\text{C}_2\text{H}_5\text{CN})$  and  $X(\text{CH}_3\text{OCHO})$ . The good correlation between  $X(\text{C}_2\text{H}_5\text{CN})$  and  $X(\text{CH}_3\text{OCHO})$ , despite the existence of regions with different abundances in the same source, such as Orion-KL, may be due to the observational resolution.

HMSFRs evolve from high-mass starless cores (HMSCs) to high-mass protostellar objects (HMPOs). As protostars form, these evolve into hot molecular cores (HMCs). Subsequently, these protostars heat the surroundings, forming hypercompact H II regions (HCHII). Further evolution results in classification into ultracompact H II regions (UCHII) and eventually H II regions (e.g., van Dishoeck & Blake 1998; Tan et al. 2014; Yamamoto 2016; Coletta et al. 2020). In Coletta et al. (2020), the phase between HMPOs and UCHII, encompassing HCHII and phases containing high-mass sources, is termed the intermediate (INT) phase. Eight sources studied by Coletta et al. (2020), 18089-1732(INT), G31.41+0.03 (INT), G24.78+0.08 (INT), W3(OH) (UCHII), G14.33-0.65 (UCHII), W51 (UCHII), G10.47+0.03 (UCHII), and G29.96-0.02 (UCHII), were selected from previous studies (Fontani et al. 2011; Fontani et al. 2014; Fontani et al. 2015a; Fontani et al. 2015b; Fontani et al. 2016; Fontani et al. 2018; Fontani et al. 2019; Colzi et al. 2018b; Colzi et al. 2018a; Mininni et al. 2018).

A similar linear scale  $S_{\text{beam}}$  with Orion-KL in this study ( $S_{\text{beam}} \approx 0.02$  pc) is expected for a target at a distance of several kpc when it is observed with a spatial resolution of beam sizes of  $\sim 1\text{--}2''$  using interferometers. In this case, a direct comparison is allowed between Orion KL and more distant sources, which are several kpc away. Therefore, we selected Sgr B2 (Bonfand et al. 2017; Bonfand et al. 2019; Busch et al. 2024; Sánchez-Monge et al. 2017; Meng et al. 2022), which was observed by interferometers ( $\theta_{\text{beam}} \approx 1\text{--}2''$ ) and has a similar  $S_{\text{beam}}$  to Orion-KL in this study, as a comparison target to compare  $X(\text{C}_2\text{H}_5\text{CN})$  and  $X(\text{CH}_3\text{OCHO})$  with the eight sources with  $S_{\text{beam}} > 0.1$  from Coletta et al. (2020). The information for each source is presented in table 5. The classification of the evolutionary stage was based on Coletta et al. (2020); Gerner et al. (2014); Gerner et al.

(2015); Bonfand et al. (2017).  $\theta_{\text{beam}}$  and  $\theta_{\text{H}_2}$  represent the beam sizes of the telescopes.  $S_{\text{beam}}$  denotes the spatial scale of the angular resolution calculated from  $\theta_{\text{beam}}$  and the distance.

Figure 7 shows  $X(\text{C}_2\text{H}_5\text{CN})$  and  $X(\text{CH}_3\text{OCHO})$  of the sources listed in table 5. The color scale corresponds to  $S_{\text{beam}}$  [pc]. The results of the eight sources from Coletta et al. (2020) (18089-1732, G31.41+0.03, G24.78+0.08, W3(OH), G14.33-0.65, W51, G10.47+0.03, and G29.96-0.02) are based solely on the transition of  $\text{CH}_3\text{OCHO}$  ( $v = 0$ ). Therefore, the plots for the HC and CR in Orion-KL utilized values of  $X(\text{CH}_3\text{OCHO}$  ( $v = 0$ )) from table 4. The solid black line represents the fitting and correlation for the eight sources with  $S_{\text{beam}} > 0.1$  pc (18089-1732, G31.41+0.03, G24.78+0.08, W3(OH), G14.33-0.65, W51, G10.47+0.03, and G29.96-0.02) (Coletta et al. 2020). The spatial resolutions of the observations for Orion-KL and Sgr B2 ( $S_{\text{beam}} < 0.1$  pc) are similar to each other but smaller than those of the other eight sources ( $S_{\text{beam}} > 0.1$  pc). Therefore, we applied an independent fitting for Orion-KL and Sgr B2. The black dashed line in figure 7 is the result of a linear fit for Orion-KL (HC and CR, not assuming source size) and Sgr B2 (N1:SE1, N1:NW3, N2, N3, N4, N5) simultaneously. Sgr B2(N1:SE1) and Sgr B2(N1:NW3) denote observations performed at approximately 0.1 pc southeast and northwest of Sgr B2 (N1), respectively (Busch et al. 2024). The results for these sources with  $S_{\text{beam}}$  smaller than 0.1 pc show a large dispersion, with a correlation coefficient of  $r = 0.57$ . The correlation coefficient remains similar ( $r = 0.54$ ) even when  $X'$  (assuming a source size of  $10''$ ) is used in place of  $X$ .

This correlation coefficient is lower than the value reported by Coletta et al. (2020) ( $r = 0.92$ ). Additionally, the solid line (Coletta et al. 2020) shifts below the dashed line (in this study) and is closer to the values of  $X(\text{C}_2\text{H}_5\text{CN})$  and  $X(\text{CH}_3\text{OCHO})$  in the CR (inverted triangle) than in the HC (triangle) in Orion-KL, as shown in figure 7. This indicates that the eight sources with  $S_{\text{beam}} > 0.1$  pc tend to have relatively high  $X(\text{CH}_3\text{OCHO})$  values. These considerations highlight the dependence of  $X$  on  $S_{\text{beam}}$ , indicating that coarser resolution observations ( $S_{\text{beam}} > 0.1$  pc) may not adequately resolve regions with distinct chemical properties. In this case,  $\text{CH}_3\text{OCHO}$  (O-bearing COMs), which is more widely distributed and highly abundant, may be predominantly observed, compared with  $\text{C}_2\text{H}_5\text{CN}$  (N-bearing COMs), which is relatively compactly distributed, as shown in figure 4.

The integrated intensity maps obtained from interferometric observations of G10.47+0.03 (Rolfs et al. 2011) and W3(OH) (Wyrowski et al. 1999), which are included among the eight sources, support this suggestion. The integrated intensity distributions of  $\text{C}_2\text{H}_5\text{CN}$  and  $\text{CH}_3\text{OCHO}$  obtained with a beam size of approximately  $4'' \times 2''$  ( $S_{\text{beam}} \approx 0.11 \times 0.06$  pc) using SMA are similar (Rolfs et al. 2011). However, the map observed with a smaller beam size (approximately  $0.5'' \times 0.3''$ , corresponding to  $S_{\text{beam}} \approx 0.01 \times 0.008$  pc) shows that the intensity distribution differs, with  $\text{CH}_3\text{OCHO}$  having a peak on the west side and  $\text{C}_2\text{H}_5\text{CN}$  having a peak on the east side. In addition,  $\text{CH}_3\text{OCHO}$  is more widely distributed than  $\text{C}_2\text{H}_5\text{CN}$  (Rolfs et al. 2011). The differences in the distributions of  $\text{C}_2\text{H}_5\text{CN}$  and  $\text{CH}_3\text{OCHO}$  and the extended distribution of  $\text{CH}_3\text{OCHO}$  at  $S_{\text{beam}} < 0.1$  are similar in this study. Additionally, these features are also observed in the integrated intensity map of W3(OH) from observations with the Plateau de Bure Interferometer (PdBI) ( $\theta_{\text{beam}} \approx 0.8'' \times 0.6''$ , corresponding to  $S_{\text{beam}} \approx 0.008 \times 0.006$  pc) (Wyrowski et al. 1999). Therefore, although a precise analysis of the abundances of  $\text{C}_2\text{H}_5\text{CN}$  and  $\text{CH}_3\text{OCHO}$  in each region is necessary, these detailed maps observed with the SMA and PdBI support the above suggestions.

**Table 5.** High-mass star-forming regions in each observation.

Source	$\alpha_{J2000}$ [h:m:s]	$\delta_{J2000}$ [° : ' : '' ]	distance [kpc]	$\theta_{\text{beam}}$ ['']	$S_{\text{beam}}$ [pc]	$\theta_{\text{H}_2}$ ['']	evolutionary stage	References <sup>†</sup>
18089-1732	18:11:51.4	-17:31:28	3.6	16-18 <sup>(a)</sup>	0.30	28 <sup>(g)</sup>	INT <sup>(a)</sup>	(a,b,c,d,e,f,g,h,i,j)
G31.41+0.31	18:47:34.2	-01:12:45	3.8	16-18 <sup>(a)</sup>	0.31	36.6 <sup>(a)</sup>	INT <sup>(a)</sup>	(a,j,k)
G24.78+0.08	18:36:12.6	-07:12:11	7.7	16-18 <sup>(a)</sup>	0.63	36.6 <sup>(a)</sup>	INT <sup>(a)</sup>	(a,j,k)
W3(OH)	02:27:04.7	+61:52:25	2.0	16-18 <sup>(a)</sup>	0.16	23 <sup>(l)</sup>	UCHII <sup>(a)</sup>	(a,j)
G14.33-0.65	18:18:54.8	-16:47:53	2.6	16-18 <sup>(a)</sup>	0.21	36.6 <sup>(a)</sup>	UCHII <sup>(a)</sup>	(a,j,k)
W51	19:23:43.9	+14:30:32	5.4	16-18 <sup>(a)</sup>	0.45	19 <sup>(l)</sup>	UCHII <sup>(a)</sup>	(a,j)
G10.47+0.03 <sup>(a)</sup>	18:08:38.0	-19:51:50	5.8	16-18 <sup>(a)</sup>	0.48	59 <sup>(m)</sup>	UCHII <sup>(a)</sup>	(a,j)
G29.96-0.02	18:46:03.0	-02:39:22	8.9	16-18 <sup>(a)</sup>	0.73	59 <sup>(m)</sup>	UCHII <sup>(a)</sup>	(a,j)
Orion-KL(HC)*	05:35:14.6	-5:22:31.0	0.418	12	0.02	12 <sup>(o)</sup>	HMC <sup>(p,q)</sup>	(this work,o,p,q,r)
Orion-KL(CR)*	05:35:14.0	-5:22:36.9	0.418	12	0.02	12 <sup>(o)</sup>	HMC <sup>(p,q)</sup>	(this work,o,p,q,r)
Sgr B2(N1)	17:47:19.87	-28:22:16.0	8.34	0.3-0.75 <sup>(i)</sup>	0.01-0.03	0.4-5 <sup>(s)</sup>	UCHII <sup>(u)</sup>	(s,t,u)
Sgr B2(N2)	17:47:19.9	-28:22:13.4	8.34	1.6 <sup>(u,v)</sup>	0.06	0.4-1.2 <sup>(u,v)</sup>	-	(u,v)
Sgr B2(N3)	17:47:19.2	-28:22:14.9	8.34	1.6 <sup>(u,v)</sup>	0.06	0.4-1.2 <sup>(u,v)</sup>	HMC <sup>(u)</sup>	(u,v)
Sgr B2(N4)	17:47:19.5	-28:22:32.4	8.34	1.6 <sup>(u,v)</sup>	0.06	0.4-1.2 <sup>(u,v)</sup>	HMC <sup>(u)</sup>	(u,v)
Sgr B2(N5)	17:47:20.0	-28:22:41.3	8.34	1.6 <sup>(u,v)</sup>	0.06	0.4-1.2 <sup>(u,v)</sup>	UCHII <sup>(u)</sup>	(u,v)

\* HC and CR correspond to the hot core and compact ridge, respectively. <sup>†</sup> References. <sup>(a)</sup> (Coletta et al. 2020) <sup>(b)</sup> (Fontani et al. 2011) <sup>(c)</sup> (Fontani et al. 2014) <sup>(d)</sup> (Fontani et al. 2015a) <sup>(e)</sup> (Fontani et al. 2015b) <sup>(f)</sup> (Fontani et al. 2016) <sup>(g)</sup> (Fontani et al. 2018) <sup>(h)</sup> (Colzi et al. 2018a) <sup>(i)</sup> (Mininni et al. 2018) <sup>(j)</sup> (Fontani et al. 2019) <sup>(k)</sup> (Colzi et al. 2018b) <sup>(l)</sup> (Rivilla et al. 2016) <sup>(m)</sup> (Liu et al. 2010) <sup>(n)</sup> (Rolfs et al. 2011) <sup>(o)</sup> (Schuller et al. 2021), We adjusted the beam size of from 8'' to 12'' using CASA. <sup>(p)</sup> (Gerner et al. 2014) <sup>(q)</sup> (Gerner et al. 2015) <sup>(r)</sup> (Taquet et al. 2015) <sup>(s)</sup> (Sánchez-Monge et al. 2017) <sup>(t)</sup> (Busch et al. 2024) <sup>(u)</sup> (Bonfand et al. 2017) <sup>(v)</sup> (Bonfand et al. 2019)

The comparison of  $X(\text{C}_2\text{H}_5\text{CN})$  and  $X(\text{CH}_3\text{OCHO})$  focusing on  $S_{\text{beam}}$  in this study confirms that  $\text{CH}_3\text{OCHO}$  may be predominantly observed in coarser resolution observations ( $S_{\text{beam}} > 0.1$ ), as suggested by interferometric results. The good correlation between  $X(\text{C}_2\text{H}_5\text{CN})$  and  $X(\text{CH}_3\text{OCHO})$  may be affected by the extent to which the spatial scale of such angular resolution includes each molecular distribution with different spatial coverages due to differences in the physical and chemical environments. To gain a more detailed understanding of the relationship between  $X(\text{C}_2\text{H}_5\text{CN})$  and  $X(\text{CH}_3\text{OCHO})$ , it is necessary to observe the differences in their abundances and spatial distributions across sources by observing distant astronomical objects with a spatial resolution sufficient to resolve individual sources.

In the Sgr B2(N) region, where  $X(\text{C}_2\text{H}_5\text{CN})$  appeared higher (positioned upward in figure 7), some prebiotic molecules, such as  $\text{H}_2\text{C}_2\text{N}_2$  (Z-(E)-HNCHCN) and  $\text{H}_2\text{C}_4\text{N}_2$  ( $\text{NH}_2\text{CH}_2\text{CN}$ ), have also been observed (Zaleski et al. 2013b; Belloche et al. 2008; Li et al. 2020). G10.47+0.03 is expected to contain a region with a high  $X(\text{C}_2\text{H}_5\text{CN})$  (Rolfs et al. 2011), similar to the Sgr B2(N) and Orion-KL HC regions.  $\text{NH}_2\text{CH}_2\text{CN}$  was also detected in G10.47+0.03 (Manna & Pal 2022). In addition, chemical model calculations suggest that the Orion-KL region is a probable source for detecting Z-(E)-HNCHCN (Zhang et al. 2020). The angular resolution of B4R/LMT-50 m enables us to resolve a 0.02 pc structure at the distance of Orion-KL, and owing to the wide bandwidth, many molecular emission lines can be observed simultaneously. These capabilities in nearby star-forming regions such as Orion-KL potentially complement detailed high angular resolution studies on distant sources using interferometers with similar  $S_{\text{beam}}$  at several kpcs and arcseconds. The B4R/LMT-50 m capabilities could help us understand the formation of prebiotic molecules and the observed differences in  $X(\text{C}_2\text{H}_5\text{CN})$  and  $X(\text{CH}_3\text{OCHO})$  across various sources.

### 4.3 Future upgrades and prospects of B4R system

The B4R and observation system are being developed (Kawabe et al. 2024). In May 2024, remote tuning of the LO power at each frequency setting to minimize the receiver noise temperature and monitoring of key parameters (e.g., the temperature of the 4K stage and vacuum gauge output) were integrated and are now ready for future use. The expansion of the IF bandwidth by adding two XFFTS boards has already been prepared and is expected to be integrated in the near future. Furthermore, efforts are being made to improve the observational efficiency and SNR through the introduction of data science methods such as GoDec and frequency-modulated local oscillators (FMLO) (Taniguchi et al. 2021; Taniguchi et al. 2020; Zhou & Tao 2011).

These updates are expected to contribute not only to the detection of faint prebiotic molecules and COMs but also to the detection of atomic line emissions from high- $z$  objects. In addition, the B4R and LMT, a single-dish telescope with a wide bandwidth, high frequency resolution, and high spatial resolution in the 2 mm band, have the potential to make significant contributions to unbiased survey observations. Observations of interstellar molecules, including COMs associated with protostars, have also been conducted in nearby low-mass star-forming regions. Detailed observations with ALMA have enabled studies that approach the issues of material transport and angular momentum transfer from protostellar envelopes to disks (e.g., Sakai et al. 2014). The factors behind the chemical diversity observed in astronomical objects during the course of star and planet formation are not yet fully understood, and it is essential to conduct survey observations of the environments surrounding protoplanetary disks using various tracer molecules. In addition, AGB stars, for which a large number of samples have been obtained through survey observations with infrared space telescopes (e.g., Spitzer; Blum et al. 2006), are known to be associated with dense molecular gas. Follow-up millimeter-wave survey observations targeting such dense molecular gas are also crucial for deepening our understanding of the chemical and physical environments of protoplanetary disks of high- and low-

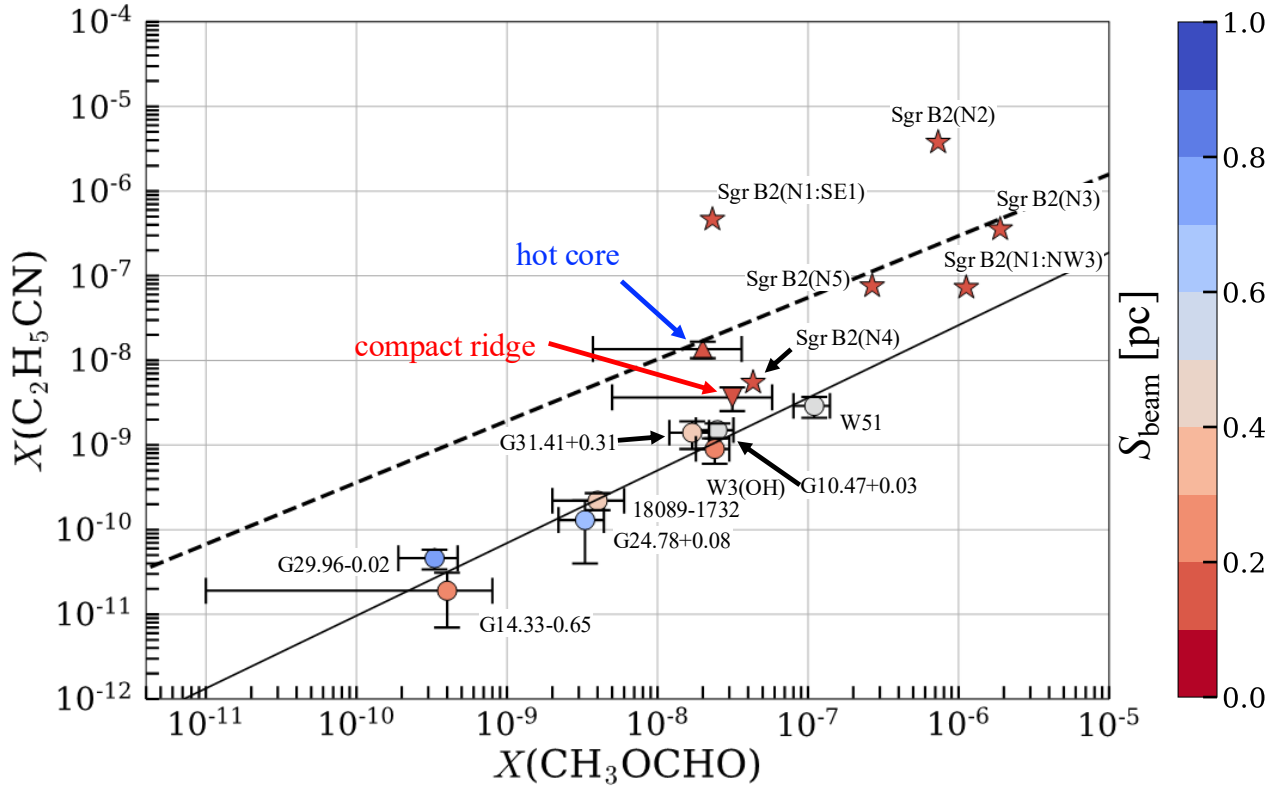


**Fig. 7.** Comparison of  $X(\text{C}_2\text{H}_5\text{CN})$  and  $X(\text{CH}_3\text{OCHO})$  among other HMSFRs and the Orion-KL HC, CR. The triangle and inverted triangle represent  $X$  of the HC and CR in this study, respectively (see table 4). The circles show the eight sources observed by Coletta et al. (2020). The stars denote observations of Sgr B2(N1:SE1, N1:NW3, N2, N3, N4, N5) from Busch et al. (2024); Bonfand et al. (2017); Bonfand et al. (2019). The solid black line represents the correlation from Coletta et al. (2020), while the dashed black line represents the fitting results using the plots of the HC, CR (not assuming source size  $10''$ ) in this study, and Sgr B2(N) observed with a resolution  $S_{\text{beam}}$  below 0.1 pc (Bonfand et al. 2017; Bonfand et al. 2019; Busch et al. 2024; Sánchez-Monge et al. 2017). The color scale corresponds to  $S_{\text{beam}}$  [pc]. Alt text: The scatter plots and fitting results. The x axis is the relative abundance with respect to  $\text{H}_2$  of  $\text{CH}_3\text{OCHO}$  (methyl formate), and the y axis is the the relative abundance with respect to  $\text{H}_2$  of  $\text{C}_2\text{H}_5\text{CN}$  (ethyl cyanide, propionitrile).

mass stars that develop from the scale of molecular cloud cores and filaments, which include environments where AGB stars disperse carbon and nitrogen as stellar winds.

## 5 Conclusion

A 2 mm band SIS receiver, the B4R, was installed on the LMT-50 m atop the Sierra Negra Mountain in Mexico, at an altitude of 4600 m. This study analyzed the results of test observations conducted in November 2019 using the OTF observation technique, with a spatial resolution of  $11\text{--}12''$  and an observed area of  $5' \times 5'$ . The main findings are summarized as follows:

1. Emission lines from  $\text{H}35\alpha$ ,  $\text{H}51\gamma$  and 29 molecular species, including isotopologues, deuterated molecules, and vibrational states, were identified with a total bandwidth of 10 GHz using XCLASS (Möller et al. 2017). A total of 337 spectra were identified, and 49 spectra were labeled as unidentified. These detections and identifications were consistent with previous studies and confirmed the observational capabilities of spectral scans achieved by B4R/LMT-50 m. Concurrently, the difference in spectral intensity between N- and O-bearing COMs in the Orion-KL HC and CR regions has demonstrated the competitive spatial resolution achieved by the B4R optics within the LMT facility. In addition to the IRAM-30 m with the

2 mm band receiver Eight MIXER Receiver (EMIR) E150, the B4R/LMT-50 m offers wide bandwidth, high frequency resolution, and higher spatial resolution observations in the 2 mm band in the Northern Hemisphere.

2. We computed the maps of column density, rotational temperature, and relative abundance with respect to  $\text{H}_2$ , focusing on representative N- and O-bearing COMs, namely,  $\text{C}_2\text{H}_5\text{CN}$  and  $\text{CH}_3\text{OCHO}$ , by a rotation diagram using a two-dimensional method based on OTF observations using the B4R/LMT-50 m. The spatial distributions and values of the column density and rotational temperature were consistent with previous studies.
3. We compared  $X(\text{C}_2\text{H}_5\text{CN})$  and  $X(\text{CH}_3\text{OCHO})$  ( $v = 0$ ) in Orion-KL, our targeted observation region, with previously reported HMSFRs. The abundance ( $X$ ) was found to be dependent on the spatial scale of the source and, therefore, very sensitive to the angular resolution ( $S_{\text{beam}}$ ). This was confirmed by comparing  $\text{CH}_3\text{OCHO}$  (O-bearing COMs), which are more widely distributed and highly abundant, and  $\text{C}_2\text{H}_5\text{CN}$  (N-bearing COMs), which are relatively compactly distributed and could dominate central core observations. This suggests that the good correlation between  $X(\text{C}_2\text{H}_5\text{CN})$  and  $X(\text{CH}_3\text{OCHO})$  reported in a previous study (Coletta et al. 2020) may be affected by the extent to which the spatial scale of such angular resolution includes each molecular distribution with different

spatial coverages due to differences in the physical and chemical environments.

## Acknowledgments

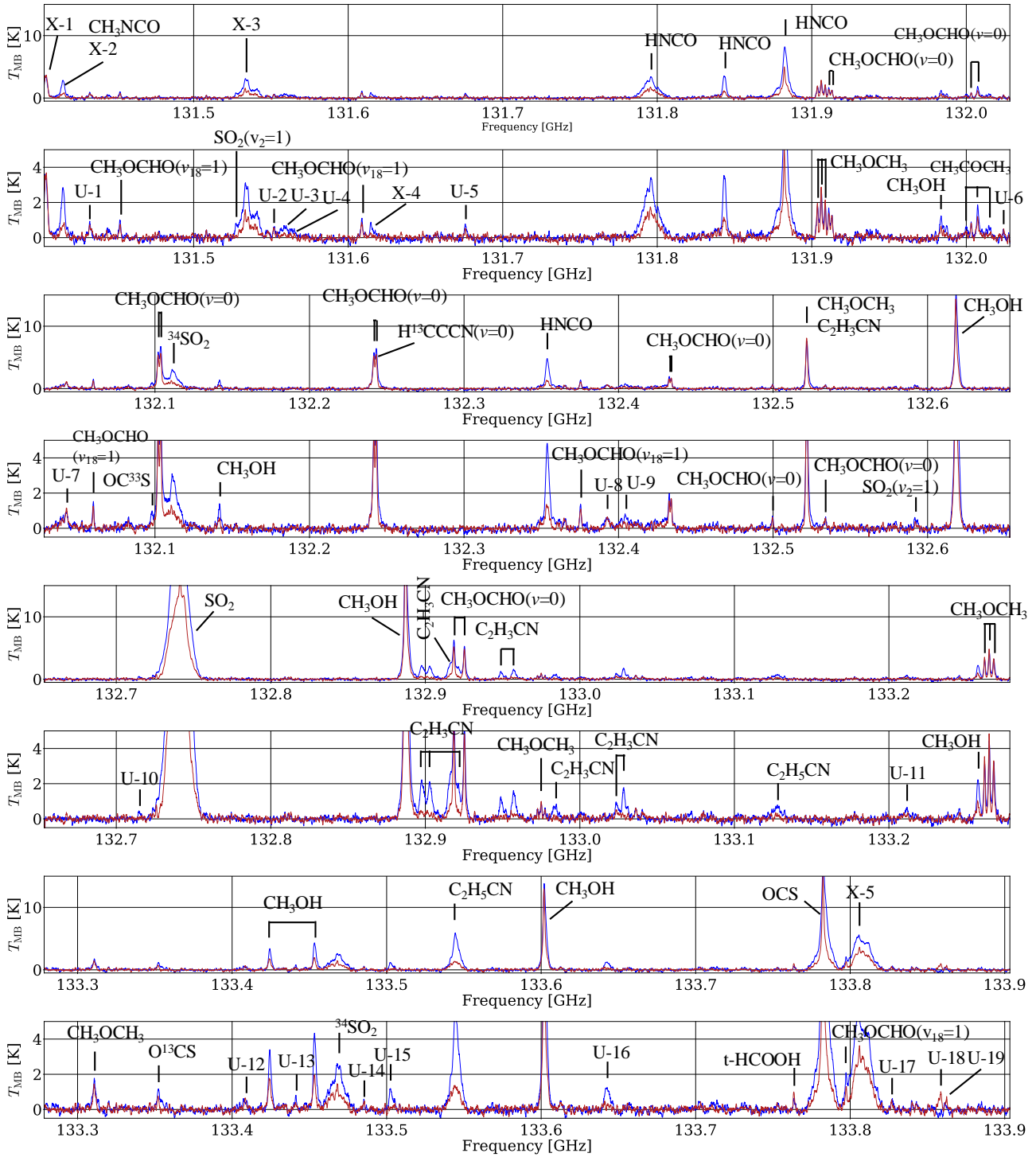
This work was financially supported by JSPS KAKENHI grant Numbers, JP15H02073, 17H06130 (RK, YT, KK), JP19K14754 (TT), 22H04939 (TS, KT, AT, YT, KK), JP19K21885, and JP25K01060 (HM). TY is supported by JSPS KAKENHI grant No. JP22J22889 and JP22KJ2625. KT is supported by JSPS KAKENHI Grant Numbers 20K14523 and 24K17096. TT is supported by MEXT Leading Initiative for Excellent Young Researchers Grant Number JPMXS0320200188. This paper makes use of data taken by the Large Millimeter Telescope Alfonso Serrano (LMT) in Mexico. The LMT project is a joint effort of the Instituto Nacional de Astrófisica, Óptica, y Electrónica (INAOE) and the University of Massachusetts at Amherst (UMASS). We also appreciate the support of the technical staff and the support scientists of the LMT during the commissioning campaign of the B4R. We would like to thank Editage (www.editage.jp) for English language editing.

## Appendix 1 Details of observed spectra

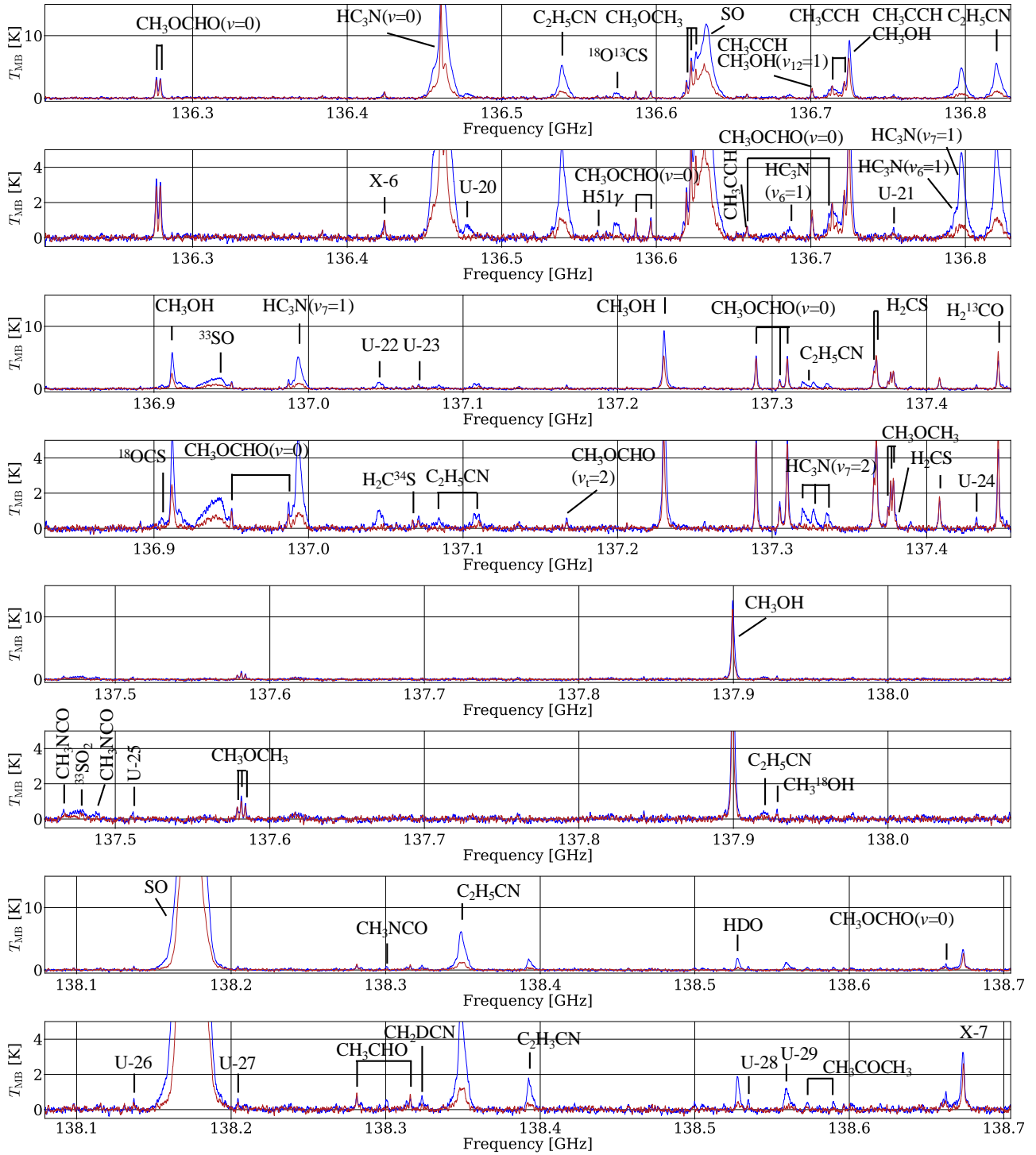
This section provides additional details of the observed spectra, as Section 3.1 outlines. The spectra within the frequency bands of 131.4–133.9 GHz, 136.2–138.7 GHz, 145.1–147.6 GHz, and 149.9–152.4 GHz, are shown in figures 8–11. Among the 404 lines detected, molecular names are assigned to 337 of the identified and tentatively identified lines, with the identified lines listed in table 6 and the tentatively identified lines listed in table 7. Tables 6 and 7 present the observed frequency (Obs. freq.),  $V_{\text{LSR}}$ , and  $T_a$  obtained from the peak tops, with values provided for both the HC and CR spectra (HC/CR). The line widths were determined by fitting using CASSIS (Vastel et al. 2015). When fitting with multiple components was appropriate, the widths of each component were listed together. The transition information and rest frequency (Rest. freq.) predominantly relied on the JPL values sourced from Splatalogue, whereas data exclusively available in the CDMS was obtained from the CDMS. The transition information and rest frequency (Rest. freq.) of recombination lines was obtained from Splatalogue. The 18 X-lines are indicated as (X-1)–(X-18) in figures 8–11, with details about the candidate molecules summarized in table 8. Lines resulting from the second downconversion or aliasing from the ADC and image sideband leakage are labeled as DC, ADC, and Image in table 8, respectively. The 49 U-lines are indicated by (U-1)–(U-49) in figures 8–11 and are listed in table 9. The observed frequency (Obs. freq.) is obtained from the peak tops, with values provided for both the HC and CR spectra (HC/CR) in tables 8 and 9. As with tables 6 and 7, the transition information and rest frequency (Rest. freq.) listed in table 8 are sourced from the JPL and CDMS catalogues. The values of  $T_a$  and the line widths in table 9 were obtained using the same method as described for tables 6 and 7.

## References

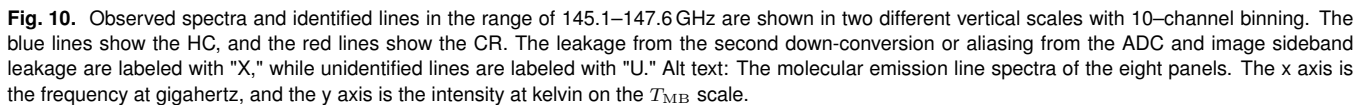
- Allen, V., van der Tak, F. F. S., Sánchez-Monge, Á., Cesaroni, R., & Beltrán, M. T. 2017, *A&AS*, 603, A133
- André, P., et al. 2010, *A&AS*, 518, L102
- Armijos-Abendaño, J., Martín-Pintado, J., Requena-Torres, M. A., Martín, S., & Rodríguez-Franco, A. 2014, *MNRAS*, 446, 3842
- Asayama, S., et al. 2014, *PASJ*, 66, 57
- Bakx, T. J. L. C., & Dannerbauer, H. 2022, *MNRAS*, 515, 678
- Becklin, E., & Neugebauer, G. 1967, *ApJ*, 147, 799
- Beckwith, S., Persson, S. E., Neugebauer, G., & Becklin, E. E. 1978, *ApJ*, 223, 464
- Bell, T. A., Cernicharo, J., Viti, S., Marcelino, N., Palau, A., Esplugues, G. B., & Tercero, B. 2014, *A&A*, 564, A114
- Belloche, A., Garrod, R. T., Müller, H. S. P., Menten, K. M., Comito, C., & Schilke, P. 2009, *A&AS*, 499, 215
- Belloche, A., Menten, K. M., Comito, C., Müller, H. S. P., Schilke, P., Ott, J., Thorwirth, S., & Hieret, C. 2008, *A&AS*, 492, 769
- Belloche, A., Müller, H. S. P., Menten, K. M., Schilke, P., & Comito, C. 2014, *A&A*, 561, C1
- Blake, G. A., Sutton, E. C., Masson, C. R., & Phillips, T. G. 1987, *ApJ*, 315, 621
- Blum, R. D., et al. 2006, *AJ*, 132, 2034
- Bonfand, M., Belloche, A., Garrod, R. T., Menten, K. M., Willis, E., Stéphan, G., & Müller, H. S. P. 2019, *A&AS*, 628, A27
- Bonfand, M., Belloche, A., Menten, K. M., Garrod, R. T., & Müller, H. S. P. 2017, *A&A*, 604, A60
- Busch, L. A., Belloche, A., Garrod, R. T., Müller, H. S. P., & Menten, K. M. 2024, *A&A*, 681, A104
- Coletta, A., Fontani, F., Rivilla, V. M., Mininni, C., Colzi, L., Sánchez-Monge, Á., & Beltrán, M. T. 2020, *A&A*, 641, A54
- Colzi, L., Fontani, F., Caselli, P., Ceccarelli, C., Hily-Blant, P., & Bizzocchi, L. 2018a, *A&AS*, 609, A129
- Colzi, L., Fontani, F., Rivilla, V. M., Sánchez-Monge, A., Testi, L., Beltrán, M. T., & Caselli, P. 2018b, *MNRAS*, 478, 3693
- Comito, C., Schilke, P., Phillips, T. G., Lis, D. C., Motte, F., & Mehninger, D. 2005, *ApJS*, 156, 127
- Crockett, N. R., Bergin, E. A., Neill, J. L., Favre, C., Blake, G. A., Herbst, E., Anderson, D. E., & Hassel, G. E. 2015, *ApJ*, 806, 239
- Endres, C. P., Schlemmer, S., Schilke, P., Stutzki, J., & Müller, H. S. P. 2016, *J. Mol. Spectrosc.*, 327, 95
- Esplugues, G. B., Tercero, B., Cernicharo, J., Goicoechea, J. R., Palau, A., Marcelino, N., & Bell, T. A. 2013, *A&AS*, 556, A143
- Feng, S., Beuther, H., Henning, T., Semenov, D., Palau, A., & Mills, E. A. C. 2015, *A&AS*, 581, A71
- Fontani, F., Busquet, G., Palau, A., Caselli, P., Sánchez-Monge, Á., Tan, J. C., & Audard, M. 2015a, *A&AS*, 575, A87
- Fontani, F., Caselli, P., Palau, A., Bizzocchi, L., & Ceccarelli, C. 2015b, *ApJL*, 808, L46
- Fontani, F., Rivilla, V. M., Caselli, P., Vasyunin, A., & Palau, A. 2016, *ApJL*, 822, L30
- Fontani, F., Rivilla, V. M., van der Tak, F. F. S., Mininni, C., Beltrán, M. T., & Caselli, P. 2019, *MNRAS*, 489, 4530
- Fontani, F., Sakai, T., Furuya, K., Sakai, N., Aikawa, Y., & Yamamoto, S. 2014, *MNRAS*, 440, 448
- Fontani, F., Vagnoli, A., Padovani, M., Colzi, L., Caselli, P., & Rivilla, V. M. 2018, *MNRAS Lett.*, 481, L79
- Fontani, F., et al. 2011, *A&AS*, 529, L7
- Friedel, D. N., & Widicus Weaver, S. L. 2012, *ApJS*, 201, 17
- Fukuyama, Y., Odashima, H., Takagi, K., & Tsunekawa, S. 1996, *ApJS*, 104, 329
- Garrod, R. T. 2013, *ApJ*, 765, 60
- Garrod, R. T., Belloche, A., Müller, H. S. P., & Menten, K. M. 2017, *A&A*, 601, A48
- Garrod, R. T., Jin, M., Matis, K. A., Jones, D., Willis, E. R., & Herbst, E. 2022, *ApJS*, 259, 1
- Gaume, R. A., Wilson, T. L., Vrba, F. J., Johnston, K. J., & Schmid-Burgk, J. 1998, *ApJ*, 493, 940
- Genzel, R., Reid, M., Moran, J., & Downes, D. 1981, *ApJ*, 244, 884
- Gerner, T., Beuther, H., Semenov, D., Linz, H., Vasyunina, T., Bihr, S., Shirley, Y. L., & Henning, T. 2014, *A&AS*, 563, A97
- Gerner, T., Shirley, Y. L., Beuther, H., Semenov, D., Linz, H., Albertsson, T., & Henning, T. 2015, *A&A*, 579, A80
- Herbst, E., & van Dishoeck, E. F. 2009, *ARA&A*, 47, 427



**Fig. 8.** Observed spectra and identified lines in the range of 131.4–133.9 GHz are shown in two different vertical scales with 10-channel binning. The blue lines show the HC, and the red lines show the CR. The leakage from the second down-conversion or aliasing from the ADC and image sideband leakage are labeled with "X," while unidentified lines are labeled with "U." Alt text: The molecular emission line spectra of the eight panels. The x axis is the frequency at gigahertz, and the y axis is the intensity at kelvin on the  $T_{\text{MB}}$  scale.



**Fig. 9.** Observed spectra and identified lines in the range of 136.2–138.7 GHz are shown in two different vertical scales with 10-channel binning. The blue lines show the HC, and the red lines show the CR. The leakage from the second down-conversion or aliasing from the ADC and image sideband leakage are labeled with "X," while unidentified lines are labeled with "U." Alt text: The molecular emission line spectra of the eight panels. The x axis is the frequency at gigahertz, and the y axis is the intensity at kelvin on the  $T_{\text{MB}}$  scale.



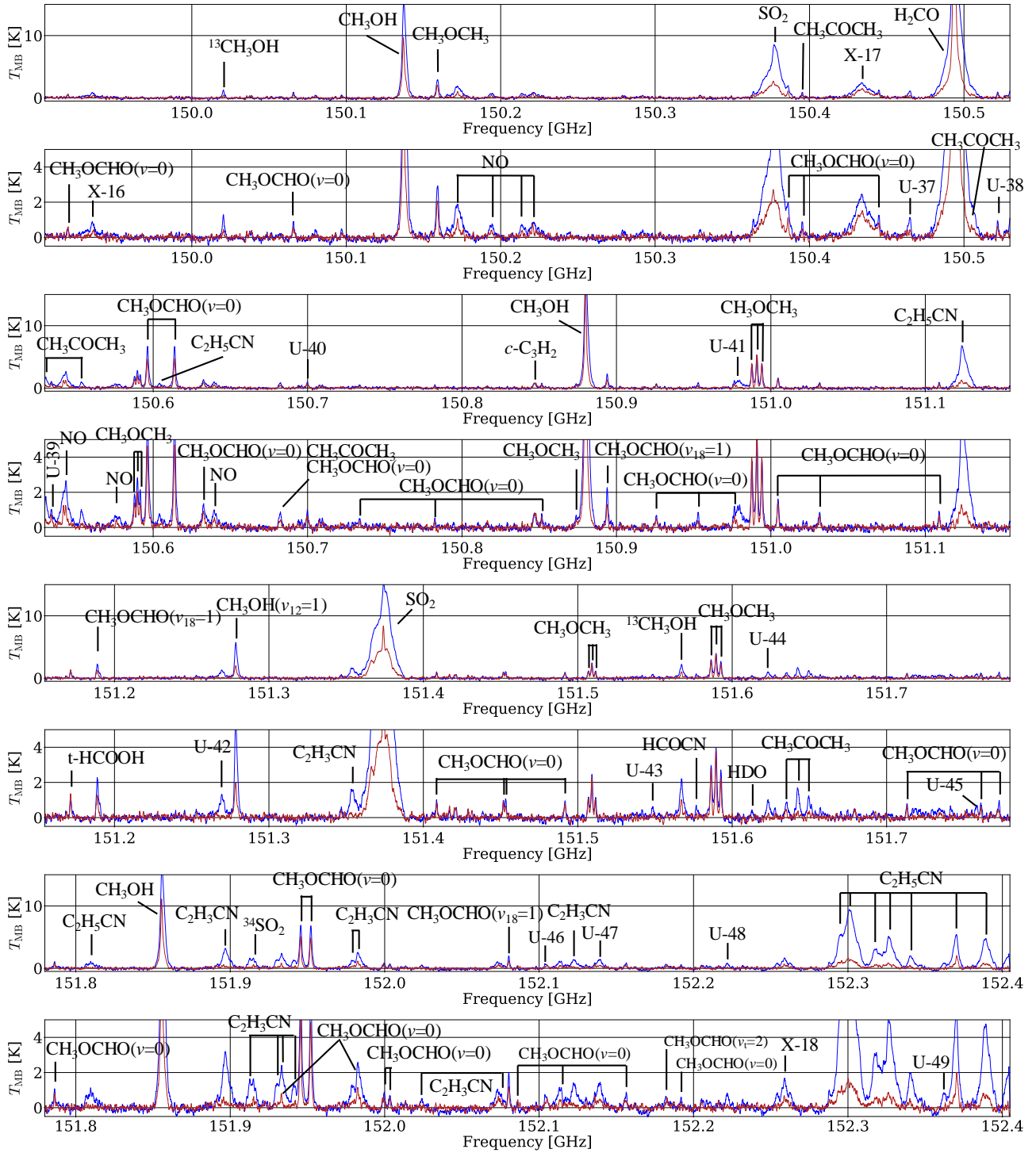


**Fig. 11.** Observed spectra and identified lines in the range 149.9–152.4 GHz are shown in two different vertical scales with 10-channel binning. The blue lines show the HC, and the red lines show the CR. The leakage from the second down-conversion or aliasing from the ADC and image sideband leakage are labeled with "X," while unidentified lines are labeled with "U." Alt text: The molecular emission line spectra of the eight panels. The x axis is the frequency at gigahertz, and the y axis is the intensity at kelvin on the  $T_{MB}$  scale.

- Hughes, D. H., et al. 2020, in *Ground-based and Airborne Telescopes VIII*, Vol. 11445 (International Society for Optics and Photonics), 1144522
- Kalenskii, S. V., & Johansson, L. E. B. 2010, *Astron. Rep.*, 54, 1084
- Karakawa, Y., Oka, K., Odashima, H., Takagi, K., & Tsunekawa, S. 2001, *J. Mol. Spectrosc.*, 210, 196
- Kawabe, R., et al. 2024, *AJ*, submitted
- Kim, M. K., et al. 2008, *PASJ*, 60, 991
- Klein, B., Hochgürtel, S., Krämer, I., Bell, A., Meyer, K., & Güsten, R. 2012, *A&AS*, 542, L3
- Kleinmann, D. E., & Low, F. J. 1967, *ApJL*, 149, L1
- Kobayashi, K., Takamura, K., Sakai, Y., Tsunekawa, S., Odashima, H., & Ohashi, N. 2013, *ApJS*, 205, 9
- Lee, C. W., Cho, S., & Lee, S. 2001, *ApJ*, 551, 333
- Li, J., et al. 2020, *MNRAS*, 492, 556
- Liu, S.-Y., Girart, J. M., Remijan, A., & Snyder, L. E. 2002, *ApJ*, 576, 255
- Liu, T., Wu, Y.-F., & Wang, K. 2010, *Res. Astron. Astrophys.*, 10, 67
- Liu, X., et al. 2022, *ApJS*, 263, 13
- Manna, A., & Pal, S. 2022, *Life Sci. Space Res.*, 34, 9
- . 2023, *Ap&SS*, 368, 44
- Martin, S., Mauersberger, R., Martin-Pintado, J., Henkel, C., & Garcia-Burillo, S. 2006, *ApJS*, 164, 450
- McGuire, B. A. 2022, *ApJS*, 259, 30
- Meng, F., et al. 2022, *A&AS*, 666, A31
- Menten, K. M., & Reid, M. J. 1995, *ApJ*, 445, L157
- Mininni, C., Fontani, F., Rivilla, V. M., Beltrán, M. T., Caselli, P., & Vasyunin, A. 2018, *MNRASLett.*, 476, L39
- Mininni, C., et al. 2023, *A&AS*, 677, A15
- Möller, T., Endres, C., & Schilke, P. 2017, *A&A*, 598, A7
- Müller, H. S. P., Schlöder, F., Stutzki, J., & Winnewisser, G. 2005, *J. Mol. Struct.*, 742, 215
- Müller, H. S. P., Thorwirth, S., Roth, D. A., & Winnewisser, G. 2001, *A&AS*, 370, L49
- Neill, J. L., Wang, S., Bergin, E. A., Crockett, N. R., Favre, C., Plume, R., & Melnick, G. J. 2013, *ApJ*, 770, 142
- Peng, T.-C., et al. 2013, *A&AS*, 554, A78
- Peng, Y., et al. 2022, *MNRAS*, 512, 4419
- Pickett, H. M., Poynter, R. L., Cohen, E. A., Delitsky, M. L., Pearson, J. C., & Müller, H. S. P. 1998, *J. Quant. Spectrosc. Radiat. Transf.*, 60, 883
- Plambeck, R. L., & Wright, M. C. H. 1987, *ApJ*, 317, L101
- Plambeck, R. L., et al. 2009, *ApJ*, 704, L25
- Qin, S.-L., Schilke, P., Wu, J., Wu, Y., Liu, T., Liu, Y., & Sánchez-Monge, Á. 2015, *ApJ*, 803, 39
- Qin, S.-L., et al. 2022, *MNRAS*, 511, 3463
- Remijan, A., Shiao, Y.-S., Friedel, D. N., Meier, D. S., & Snyder, L. E. 2004, *ApJ*, 617, 384
- Rivilla, V. M., Fontani, F., Beltrán, M. T., Vasyunin, A., Caselli, P., Martín-Pintado, J., & Cesaroni, R. 2016, *ApJ*, 826, 161
- Rivilla, V. M., et al. 2018, *MNRASLett.*, 483, L114
- . 2021, *Proceedings of the National Academy of Science*, 118, e2101314118
- Rolfs, R., Schilke, P., Zhang, Q., & Zapata, L. 2011, *A&AS*, 536, A33
- Ruud, M., Wakelam, V., & Hersant, F. 2016, *MNRAS*, 459, 3756
- Sakai, N., et al. 2014, *Nature*, 507, 78
- Sánchez-Monge, Á., et al. 2017, *A&A*, 604, A6
- Sanz-Novo, M., et al. 2023, *ApJ*, 954, 3
- Schuller, F., et al. 2021, *A&A*, 651, A36
- Suzuki, T., Ohishi, M., Hirota, T., Saito, M., Majumdar, L., & Wakelam, V. 2016, *ApJ*, 825, 79
- Suzuki, T., Ohishi, M., Saito, M., Hirota, T., Majumdar, L., & Wakelam, V. 2018, *ApJS*, 237, 3
- Takano, S., Sakai, Y., Kakimoto, S., Sasaki, M., & Kobayashi, K. 2012, *PASJ*, 64, 89
- Tan, J. C., Beltran, M. T., Caselli, P., Fontani, F., Fuente, A., Krumholz, M. R., McKee, C. F., & Stolte, A. 2014, in *Protostars and Planets VI* (University of Arizona Press), 149
- Taniguchi, A., Tamura, Y., Ikeda, S., Takekoshi, T., & Kawabe, R. 2021, *AJ*, 162, 111
- Taniguchi, A., et al. 2020, *PASJ*, 72, 2
- Taniguchi, K., et al. 2024, *ApJ*, 963, 12
- Taquet, V., López-Sepulcre, A., Ceccarelli, C., Neri, R., Kahane, C., & Charnley, S. B. 2015, *ApJ*, 804, 81
- Tercero, B., Cernicharo, J., Pardo, J. R., & Goicoechea, J. R. 2010, *A&AS*, 517, A96
- Tercero, B., Cuadrado, S., López, A., Brouillet, N., Despois, D., & Cernicharo, J. 2018, *A&A*, 620, L6
- Tercero, B., Vincent, L., Cernicharo, J., Viti, S., & Marcelino, N. 2011, *A&AS*, 528, A26
- The Casa Team, et al. 2022, *PASP*, 134, 114501
- Turner, B. E. 1989, *ApJS*, 70, 539
- . 1991, *ApJS*, 76, 617
- van der Walt, S. J., Kristensen, L. E., Jørgensen, J. K., Calcutt, H., Manigand, S., el Akel, M., Garrod, R. T., & Qiu, K. 2021, *A&A*, 655, A86
- van Dishoeck, E. F., & Blake, G. A. 1998, *ARA&A*, 36, 317
- Vastel, C., Bottinelli, S., Caux, E., Glorian, J. M., & Boiziot, M. 2015, in *SF2A-2015: Proceedings of the Annual meeting of the French Society of Astronomy and Astrophysics*, ed. F. Martins, S. Boissier, V. Buat, L. Cambrésy, & P. Petit, 313–316
- Widicus Weaver, S. L., & Friedel, D. N. 2012, *ApJS*, 201, 16
- Wyrowski, F., Schilke, P., Malcolm Walmsley, C., & Menten, K. M. 1999, *ApJ*, 514, L43
- Yamamoto, S. 2016, *Introduction to Astrochemistry: Chemical Evolution from Interstellar Clouds to Star and Planet Formation*, *Astronomy and Astrophysics Library* (Springer Japan)
- Zaleski, D. P., et al. 2013a, *ApJL*, 765, L10
- . 2013b, *ApJL*, 765, L10
- Zapata, L. A., Schmid-Burgk, J., & Menten, K. M. 2011, *A&A*, 529, A24
- Zeng, S., et al. 2018, *MNRAS*, 478, 2962
- Zernickel, A., et al. 2012, *A&AS*, 546, A87
- Zhang, X., Quan, D., Chang, Q., Herbst, E., Esimbek, J., & Webb, M. 2020, *MNRAS*, 497, 609
- Zhou, T., & Tao, D. 2011, in the *28th International Conference on Machine Learning (ICML-11)*, ed. L. Getoor & T. Scheffer, 33–40
- Ziurys, L. M., & McGonagle, D. 1993, *ApJS*, 89, 155

**Table 6.** The detected lines in this observations.

Species	Obs. freq. (HC/CR) [GHz]	Rest. freq. [GHz]	Transition	$V_{\text{LSR}}$ [km/s]	$T_{\text{a}}$ [K]	Width [km/s]	Comments
H35 $\alpha$	147.052859/147.052938	147.046848	-	-	-	-	blend CH <sub>3</sub> C <sup>13</sup> N
H51 $\gamma$	136.561813	136.559284	-	-5.6	0.58/-	0.97/-	
NO	150.172063/150.171844	150.17648	$J=3/2-1/2$ , $\Omega=1/2^+$ , $F=5/2-3/2$	8.8/9.3	1.42/0.88	11.0/4.0	
	150.194500/150.193891	150.19876	$J=3/2-1/2$ , $\Omega=1/2^+$ , $F=3/2-1/2$	8.5/9.7	0.92/0.57	7.0/3.0	
	150.214875/150.214266	150.21873	$J=3/2-1/2$ , $\Omega=1/2^+$ , $F=3/2-3/2$	7.7/8.9	0.75/0.55	7.0/3.5	blend NO
	150.220281/150.220750	150.22566	$J=3/2-1/2$ , $\Omega=1/2^+$ , $F=1/2-1/2$	10.7/9.8	0.90/0.58	12.9/12.6	blend NO
	150.543563/150.543484	150.54652	$J=3/2-1/2$ , $\Omega=1/2^-$ , $F=5/2-3/2$	5.9/6.0	2.09/1.37	1.2,11.5/1.8	blend U-39
	150.575234/150.576297	150.58056	$J=3/2-1/2$ , $\Omega=1/2^-$ , $F=1/2-1/2$	10.6/8.5	0.57/0.58	12.7/2.4	
	150.639328/150.639859	150.64434	$J=3/2-1/2$ , $\Omega=1/2^-$ , $F=3/2-1/2$	10.0/8.9	0.96/0.64	6.3/5.7	
CS	146.964281/146.964516	146.969033	3-2	9.7/9.2	28.4/33.5	9.8,29.3,3.3 /12.4,30.8,3.3	blend CH <sub>3</sub> OCHO( $v=0$ , $v_{18}=1$ )
C <sup>33</sup> S	145.751375/145.751063	145.7557316	3-2	9.0/9.6	3.25/2.72	9.4,2.2/4.9	CDMS, blend C <sub>2</sub> H <sub>5</sub> CN
SO	136.632313/136.631094	136.634799	5(6)-5(5)	5.5/8.1	8.45/3.95	29.7,9.3 /13.0,1.4,29.0	blend CH <sub>3</sub> OCH <sub>3</sub> , CH <sub>3</sub> CCH
	138.175156/138.174844	138.1786	4(3)-3(2)	7.5/8.1	40.8/34.6	-	
<sup>33</sup> SO	136.941172/136.942234	136.934082	4(3)-3(2), $F=5/2-3/2$	-	-	-	CDMS, blend CH <sub>3</sub> OCHO( $v=0$ ), <sup>33</sup> SO
		136.939357	4(3)-3(2), $F=7/2-5/2$	-	-	-	CDMS, blend <sup>33</sup> SO
		136.943672	4(3)-3(2), $F=9/2-7/2$	-	-	-	CDMS, blend <sup>33</sup> SO
		136.946194	4(3)-3(2), $F=11/2-9/2$	-	-	-	CDMS, blend <sup>33</sup> SO
SO <sub>2</sub>	132.741594/132.741141	132.74486	14(2,12)-14(1,13)	7.4/8.4	19.0/12.1	9.7,30.2,6.0 /5.7,2.4,27.3	
	146.547547/146.548531	146.55008	10(4,6)-11(3,9)	5.2/3.2	6.95/2.90	7.7,29.2/25.5	
	146.601484/146.600953	146.60552	4(2,2)-4(1,3)	8.3/9.3	14.9/11.4	20.1,8.9,13.5 /5.9,2.0,29.6	blend CH <sub>3</sub> OCHO( $v=0$ , $v_{18}=1$ ), CH <sub>3</sub> OCH <sub>3</sub> , CH <sub>3</sub> OH
	150.377156/150.376547	150.3811	15(5,11)-16(4,12)	7.9/9.1	5.76/1.98	7.3,2.9,26.7 /19.9,1.4,9.7	
	151.374313/151.374000	151.37863	2(2,0)-2(1,1)	8.5/9.2	10.8/5.81	14.9,10.5, 2.5,20.3 /1.6,22.3,6.8	blend C <sub>2</sub> H <sub>3</sub> CN
SO <sub>2</sub> ( $v_2=1$ )	131.527141/131.526375	131.5305100	12(2,10)-12(1,11)	-	-	-	blend X-3
	132.591516/-	132.594390	10(2,8)-10(1,9)	6.5/-	0.83/-	6.1/-	
	145.735500/-	145.7399920	16(2,14)-16(1,15)	9.2/-	1.08/-	3.8/-	
<sup>33</sup> SO <sub>2</sub>	137.478703	137.4735010	6(2,4)-6(1,5), $F=11/2-9/2$	-	-	-	blend <sup>33</sup> SO <sub>2</sub>
		137.4744968	6(2,4)-6(1,5), $F=13/2-15/2$	-	-	-	blend <sup>33</sup> SO <sub>2</sub>
		137.4754741	6(2,4)-6(1,5), $F=9/2-9/2$	-	-	-	blend <sup>33</sup> SO <sub>2</sub>
		137.4764698	6(2,4)-6(1,5), $F=15/2-15/2$	-	-	-	blend <sup>33</sup> SO <sub>2</sub>
		137.4792202	6(2,4)-6(1,5), $F=13/2-11/2$	-	-	-	blend <sup>33</sup> SO <sub>2</sub>

Table 6. (Continued)

		137.4796866	6(2,4)-6(1,5), F=11/2-11/2	-	-	-	blend <sup>33</sup> SO <sub>2</sub>
		137.4806821	6(2,4)-6(1,5), F=13/2-13/2	-	-	-	blend <sup>33</sup> SO <sub>2</sub>
		137.4811484	6(2,4)-6(1,5), F=11/2-13/2	-	-	-	blend <sup>33</sup> SO <sub>2</sub>
		137.4816598	6(2,4)-6(1,5), F=9/2-11/2	-	-	-	blend <sup>33</sup> SO <sub>2</sub>
		137.4826550	6(2,4)-6(1,5), F=15/2-13/2	-	-	-	blend <sup>33</sup> SO <sub>2</sub>
<sup>34</sup> SO <sub>2</sub>	132.111359/132.110750	132.11404	12(1,11)-12(0,12)	6.1/7.5	2.48/1.32	11.0/20.4	blend CH <sub>3</sub> OCHO( <i>v</i> =0)
	133.469719	133.47147	5(1,5)-4(0,4)	3.9	2.27/0.79	7.8,28.4 /1.5,27.1	
	151.915047/151.914969	151.9175597	4(3,1)-5(2,4)	-	-	-	blend C <sub>2</sub> H <sub>3</sub> CN
OCS	133.782547/133.782234	133.7859	11-10	7.5/8.2	13.2/11.6	24.9,8.5,2.8 /22.3,7.0,2.0	
	145.942578/145.942266	145.946812	12-11	8.7/9.3	13.6/13.8	15.8,8.8,2.2, 8.8/2.6,19.3, 2.6	blend CH <sub>3</sub> OCHO ( <i>v</i> =0, <i>v</i> <sub>18</sub> =1)
O <sup>13</sup> CS	133.352984/133.352063	133.355416	11-10	5.5/7.5	0.93/0.83	7.8/2.7	
	145.473188/145.472125	145.477197	12-11	8.3/10.5	1.25/0.77	6.4/4.5	
HDO	138.528109/138.527734	138.53057	6(1,6)-5(2,3)	5.3/6.1	1.39/0.77	5.2/4.7	
	151.612969/-	151.61619	7(3,4)-7(3,5)	6.4/-	0.67/-	3.1/-	
HNCO	131.795719/131.795797	131.7991113	6(3,4)-5(3,3),F=5-5	7.7/7.5	2.82/1.56	4.2,30.0,6.3 /22.5	
		131.7991114	6(3,3)-5(3,2),F=5-5	7.7/7.5			
		131.7991801	6(3,4)-5(3,3),F=5-6	7.9/7.7			
		131.7991802	6(3,3)-5(3,2),F=5-6	7.9/7.7			
		131.7991942	6(3,4)-5(3,3),F=5-4	7.9/7.7			
		131.7991943	6(3,3)-5(3,2),F=5-4	7.9/7.7			
		131.7992221	6(3,4)-5(3,3),F=7-6	8.0/7.8			
		131.7992222	6(3,3)-5(3,2),F=7-6	8.0/7.8			
		131.799402	6(3,4)-5(3,3),F=6-5	8.4/8.2			
		131.7994021	6(3,3)-5(3,2),F=6-5	8.4/8.2			
		131.7994709	6(3,4)-5(3,3),F=6-6	8.5/8.4			
		131.799471	6(3,3)-5(3,2),F=6-6	8.5/8.4			
	131.843328	131.8453368	6(2,5)-5(2,4),F=5-5	4.6	2.88/1.05	5.8/5.9	
		131.8457502	6(2,5)-5(2,4),F=5-6	5.5			
		131.8458342	6(2,5)-5(2,4),F=7-6	5.7			
		131.8458344	6(2,5)-5(2,4),F=5-4	5.7			
		131.8459184	6(2,5)-5(2,4),F=6-5	5.9			
		131.8460644	6(2,4)-5(2,3),F=5-5	6.2			
		131.8463318	6(2,5)-5(2,4),F=6-6	6.8			
		131.8464777	6(2,4)-5(2,3),F=5-6	7.2			
		131.8465617	6(2,4)-5(2,3),F=7-6	7.4			
		131.8465619	6(2,4)-5(2,3),F=5-4	7.4			
		131.8466459	6(2,4)-5(2,3),F=6-5	7.5			
		131.8470591	6(2,4)-5(2,3),F=6-6	8.5			
	131.882625/131.882156	131.8849274	6(0,6)-5(0,5),F=5-5	5.2/6.3	5.96/3.91	6.3,24.0 /14.7,1.9	
		131.8856165	6(0,6)-5(0,5),F=5-6	6.8/7.9			
		131.8857342	6(0,6)-5(0,5),F=7-6	7.1/8.1			
		131.8857419	6(0,6)-5(0,5),F=6-5	7.1/8.2			
		131.8857569	6(0,6)-5(0,5),F=5-4	7.1/8.2			
		131.886431	6(0,6)-5(0,5),F=6-6	8.7/9.7			
	132.353531/132.353609	132.3561165	6(1,5)-5(1,4),F=5-5	5.9/5.7	3.52/1.41	6.9,2.9/7.1	
		132.3566445	6(1,5)-5(1,4),F=5-6	7.1/6.9			
		132.356738	6(1,5)-5(1,4),F=7-6	7.3/7.1			
		132.3567521	6(1,5)-5(1,4),F=5-4	7.3/7.1			

Table 6. (Continued)

		132.3567638	6(1,5)-5(1,4), $F=6-5$	7.3/7.1			
		132.3572919	6(1,5)-5(1,4), $F=6-6$	8.5/8.3			
H <sub>2</sub> CO	145.598250/145.598328	145.602949	2(0,2)-1(0,1)	9.7/9.5	21.0/27.2	28.0,10.1,3.8 /9.0,26.3,2.7	
	150.493594/150.493516	150.498334	2(1,1)-1(1,0)	9.4/9.6	30.0/31.0	11.0,27.4,3.8 /8.5,25.4,2.8	blend CH <sub>3</sub> COCH <sub>3</sub>
H <sub>2</sub> <sup>13</sup> CO	137.446500/137.446188	137.4499503	2(1,2)-1(1,1)	7.5/8.2	3.55/4.97	3.1/1.9	
	146.631469/146.631016	146.6356717	2(1,1)-1(1,0)	8.6/9.5	2.53/4.25	3.0/2.2	
o-H <sub>2</sub> CS	137.366000	137.36917	4(3,2)-3(3,1)	-	-	-	blend H <sub>2</sub> CS( $v=0$ )
p-H <sub>2</sub> CS	137.367453/137.367375	137.371051	4(0,4)-3(0,3)	7.9/8.0	3.81/4.22	3.5/2.3	blend H <sub>2</sub> CS( $v=0$ )
	137.378750/137.378359	137.382029	4(2,3)-3(2,2)	-	-	-	blend CH <sub>3</sub> OCH <sub>3</sub>
	137.408422	137.41177	4(2,2)-3(2,1)	7.3	1.34/1.65	3.0/2.3	
c-C <sub>3</sub> H <sub>2</sub>	150.847078/150.845938	150.851908	4(1,4)-3(0,3)	9.6/11.9	0.71/0.89	4.4/4.6	
HC <sub>3</sub> N	136.460563	136.4644013	$J=15-14$	8.4	12.5/11.5	10.5,11.4,3.2, 14.0/5.8,24.0, 2.3	
	145.556281	145.560946	$J=16-15$	9.6	14.1/13.8	13.7,13.4,2.7, blend CH <sub>3</sub> OCH <sub>3</sub> 9.5/7.6,24.9, 2.5	
HC <sub>3</sub> N ( $v_6=1$ )	136.685953/-	136.6882521	$J=15-14, l=1e$	5.0/-	0.84/-	8.6/-	CDMS
	136.792547/136.793844	136.7956896	$J=15-14, l=1f$	-	-	-	CDMS, blend HC <sub>3</sub> N( $v_7=1$ )
	145.796234/-	145.799706	$J=16-15, l=1e$	7.1/-	1.09/-	9.5/-	CDMS
	145.911297/145.911219	145.914297	$J=16-15, l=1f$	-	-	-	CDMS, blend HC <sub>3</sub> N( $v_7=1$ )
HC <sub>3</sub> N ( $v_7=1$ )	136.797344/136.797422	136.7997925	$J=15-14, l=1e$	5.4/5.2	3.61/0.68	6.2,20.4/16.3	CDMS, blend HC <sub>3</sub> N( $v_6=1$ )
	136.993203/136.993891	136.9957308	$J=15-14, l=1f$	5.5/4.0	3.69/0.90	14.2,5.2/14.3	CDMS, blend CH <sub>3</sub> OCHO( $v=0$ )
	145.914875/145.915641	145.9186679	$J=16-15, l=1e$	7.8/6.2	4.17/1.36	17.6,6.4,3.3 /13.2	CDMS, blend HC <sub>3</sub> N( $v_6=1$ )
	146.123859/146.123938	146.1276387	$J=16-15, l=1f$	7.8/7.6	4.44/1.18	5.6,11.5/13.0	CDMS, blend C <sub>2</sub> H <sub>5</sub> CN
HC <sub>3</sub> N ( $v_7=2$ )	137.319766/-	137.3225355	$J=15-14, l=0$	6.0/-	0.97/-	7.2/-	CDMS, blend C <sub>2</sub> H <sub>5</sub> CN
	137.326031/-	137.3295712	$J=15-14, l=2e$	7.7/-	0.96/-	6.1/-	CDMS
	137.336250/-	137.3380387	$J=15-14, l=2f$	3.9/-	0.81/-	7.1/-	CDMS
	146.471703/-	146.47495	$J=16-15, l=0$	6.6/-	0.98/-	5.2/-	CDMS
	146.480016/-	146.4837002	$J=16-15, l=2e$	7.5/-	1.03/-	5.6/-	CDMS
	146.490859/-	146.4939773	$J=16-15, l=2f$	6.4/-	0.93/-	6.3/-	CDMS
t-HCOOH	133.763625/133.763391	133.76707	6(0,6)-5(0,5)	7.7/8.2	0.77/1.17	3.2/1.9	
	151.171359/151.171438	151.1762809	7(1,7)-6(1,6)	9.8/9.6	0.95/1.23	3.0/1.6	
CH <sub>3</sub> CN	147.031891/147.031500	147.0358351	8(7)-7(7)	8.0/8.8	1.70/1.17	5.9/4.2	
	147.068516	147.0726021	8(6)-7(6)	8.3	5.69/2.83	13.5,4.9 /13.3,3.7	blend CH <sub>3</sub> <sup>13</sup> CN
	147.099719	147.103738	8(5)-7(5)	8.2	7.33/4.14	5.5,18.3 /2.6,15.1	blend U-33, CH <sub>3</sub> <sup>13</sup> CN
	147.125422/147.124813	147.1292302	8(4)-7(4)	7.8/9.0	8.95/5.74	12.5,5.0 /11.7,2.5	
	147.144813/147.144656	147.1490683	8(3)-7(3)	8.7/9.0	14.0/10.9	19.4,11.0,2.9, blend CH <sub>3</sub> CN( $v=0$ ) 7.6/13.9,2.5	
	147.159000	147.1632441	8(2)-7(2)	8.6	12.70/9.77	10.9,2.8 /11.3,2.3	blend CH <sub>3</sub> CN( $v=0$ )
	147.167547/147.167078	147.1717519	8(1)-7(1)	8.6/9.5	16.1/12.5	2.3,17.2,2.3 /2.1,16.5,2.0	blend CH <sub>3</sub> CN( $v=0$ )
	147.169906/147.170063	147.1745883	8(0)-7(0)	9.5/9.2	18.3/14.1	common with above	blend CH <sub>3</sub> CN( $v=0$ )
CH <sub>3</sub> CN ( $v_8=1$ )	147.472656/147.473047	147.4749743	$J=8-7, K=-6-6$	4.7/3.9	1.35/0.86	6.3/2.6	
		147.4759962	$J=8-7, ^lK=-1-1$	6.8/6.0	1.35/0.86	6.3/2.6	
	147.541016/-	147.5439118	$J=8-7, K=-4-4$	5.9/-	0.79/-	2.9/-	

Table 6. (Continued)

	147.566047/-	147.5698084	$J=8-7, K=-3--3$	7.6/-	0.85/-	5.4/-	
	147.571766/147.571391	147.5755526	$J=8-7, K=5-5$	7.7/8.5	0.82/0.80	3.9/-	
	147.586422/147.585813	147.5898941	$J=8-7, K=-2--2$	7.1/8.3	1.36/1.16	5.1/8.8	blend $\text{CH}_3\text{CN}(v_8=1)$
	147.590844/147.590766	147.5953801	$J=8-7, K=4-4$	9.2/9.4	1.69/0.92	8.5/3.2	
	147.600234	147.6039578	$J=8-7, K=-1--1$	7.6	2.62/1.01	6.5/7.8	
$\text{CH}_3\text{OH}$	131.983797/131.983563	131.986795	$21(5)^+-22(4)^+$	6.8/7.3	1.08/0.65	3.8/2.3	
	132.141953/132.142031	132.144943	$21(5)^--22(4)^-$	6.8/6.6	1.41/0.89	3.7/3.8	
	132.618453/132.618063	132.621824	$6(2)^--7(1)^-$	7.6/8.5	11.3/11.1	7.6,2.5 /7.4,1.9	
	132.887016	132.890759	$6(-1)-5(0)\text{E}2$	8.4	21.2/25.5	15.1,7.0,2.3 /1.1,7.9,1.6	
	133.257453/133.257375	133.260869	$20(4)-19(5)\text{E}1$	7.7/7.9	1.72/0.93	4.3/3.8	
	133.424172	133.427704	$20(0)-20(-1)\text{E}2$	7.9	2.71/1.75	5.4,2.8/4.4	
	133.453000/133.453234	133.456518	$22(-2)-22(1)\text{E}2$	7.9/7.4	3.43/1.80	6.2,3.2/4.4	
	133.601859/133.601641	133.605439	$5(-2)-6(-1)\text{E}2$	8.0/8.5	10.4/9.8	7.8,2.6 /8.4,2.2	
	136.724938/136.724859	136.728343	$16(3)^+-15(4)^+$	7.5/7.6	7.04/4.98	8.0,3.0 /8.0,2.9	blend $\text{CH}_3\text{CCH}$
	136.911641	136.915288	$19(0)-19(-1)\text{E}2$	8.0	4.51/2.22	3.8/5.1	
	137.229969	137.23338	$16(3)^--15(4)^-$	7.5	7.40/4.53	7.6,2.8 /7.4,2.3	
	137.899563/137.899484	137.903064	$7(-4)-8(-3)\text{E}2$	7.6/7.8	9.72/8.62	6.8,2.2 /7.0,1.8	
	145.120234/145.119859	145.124332	$3(2)^--2(2)^-$	8.5/9.2	7.62/7.92	1.9,8.3,2.8 /2.0,11.2,1.9	blend $\text{CH}_3\text{OH}$ , X-8,X-9,X-10
	145.121688/145.121609	145.126191	$3(2)-2(2)\text{E}1$	9.3/9.5	9.28/11.01	common with above	blend $\text{CH}_3\text{OH}$ , X-8,X-9,X-10
	145.127250	145.131864	$3(1)-2(1)\text{E}1$	9.5	7.90/9.21	3.7,11.0,2.1 /1.6,7.7,1.8	blend $\text{CH}_3\text{OH}$
	145.128703	145.133415	$3(2)^+-2(2)^+$	9.7	7.42/7.78	common with above	blend $\text{CH}_3\text{OH}$
	145.761906/145.761672	145.766227	$16(0)-16(-1)\text{E}2$	8.9/9.4	6.33/5.18	6.7,2.8 /1.7,6.8	
	146.152938/-	146.156763	$25(6)^--24(7)^-$	7.8/-	0.90/-	0.89/-	blend $\text{CH}_3\text{OCH}_3$
		146.156825	$25(6)^+-24(7)^+$	8.0/-	0.90/-	0.89/-	blend $\text{CH}_3\text{OCH}_3$
	146.282797	146.286876	$20(6)^+-21(5)^+$	8.4	2.04/1.38	4.7/3.8	
	146.363891/146.363672	146.368328	$3(1)^--2(1)^-$	9.1/9.5	14.7/18.1	7.8,3.2 /8.3,2.1	
	146.614000/146.614078	146.618697	$9(0)^+-8(1)^+$	9.6/9.4	21.4/21.5	4.4,0.47,12.5 /2.0,8.9,1.9	blend $\text{SO}_2$
	147.392844/147.392781	147.396869	$24(-2)-24(1)\text{E}2$	8.2/8.3	3.08/2.39	3.6/3.1	blend $\text{CH}_3\text{OCHO}(v=0)$
	150.137203/150.136969	150.141672	$14(0)-14(-1)\text{E}2$	8.9/9.4	10.81/6.83	7.6,2.9 /7.5,2.0	
	150.880203/150.879813	150.884543	$12(-1)-11(-2)\text{E}2$	8.6/9.4	15.7/12.4	8.1,0.79,3.1 /6.9,1.7	blend $\text{CH}_3\text{OCH}_3$
	151.855828/151.855375	151.860249	$13(0)-13(-1)\text{E}2$	8.7/9.6	11.83/8.17	7.7,2.6/7.2,1.7	
$^{13}\text{CH}_3\text{OH}$	146.053359/-	146.057653	$16(0,16)-16(-1,16)$	8.8/-	0.85/-	1.9/-	CDMS
	150.020391/150.020609	150.024809	$14(0,14)-14(-1,14)$	8.8/8.4	1.11/0.60	3.1/1.7	CDMS
	151.567266/151.567109	151.571517	$13(0,13)-13(-1,13)$	8.4/8.7	2.18/0.91	0.6,6.5/2.8	CDMS
$\text{CH}_3\text{CHO}$	138.281063/138.281281	138.28488	$7(1,6)-6(1,5)\text{E}$	8.3/7.8	0.83/1.04	3.1/2.1	
	138.316469/138.315844	138.31975	$7(1,6)-6(1,5)\text{A}$	7.1/8.5	0.57/0.98	4.0/1.3	
$\text{CH}_3\text{CCH}$	136.658781/136.658719	136.66274	$8(5)-7(5)$	8.7/8.8	0.83/0.90	3.1/1.8	blend $\text{CH}_3\text{OCHO}(v=0)$
	136.700531/136.700750	136.7045016	$8(3)-7(3)$	8.7/8.2	1.19/1.46	3.8/2.2	blend $\text{CH}_3\text{OH}(v_{12}=1)$
	136.713641	136.7175596	$8(2)-7(2)$	8.6	1.70/1.67	-	blend $\text{CH}_3\text{OCHO}(v=0)$
	136.721500/136.721656	136.7253966	$8(1)-7(1)$	8.5/8.2	2.03/2.34	3.5/2.1	blend $\text{CH}_3\text{OH}$

Table 6. (Continued)

	136.724938/136.724859	136.7280098	8(0)-7(0)	6.7/6.9	7.04/4.98	8.0,3.0 /8.0,2.9	blend CH <sub>3</sub> OH
CH <sub>3</sub> NCO ( <i>v</i> =0)	131.415891/131.416281	131.418379	15(-1,0)-14(-1,0), <i>m</i> =-3	5.7/4.8	2.34/0.94	6.4/6.3	CDMS, blend X-2
	137.466797/137.467406	137.469287	16(1,16)-15(1,15), <i>m</i> =0	5.4/4.1	0.55/0.57	3.4/-	CDMS
	137.489688/-	137.491243	16(1,0)-15(1,0), <i>m</i> =1	3.4/-	0.63/-	10.1/-	CDMS
	138.300516/-	138.303496	16(3,14)-15(3,13), <i>m</i> =0	6.5/-	0.64/-	3.4/-	CDMS
		138.304065	16(3,13)-15(3,12), <i>m</i> =0	7.7/7.4	0.64/0.48	3.4/-	CDMS
C <sub>2</sub> H <sub>3</sub> CN	132.521859/132.521781	132.524583	14(2,13)-13(2,12)	6.2/6.3	5.83/6.38	7.9,3.0 /8.5,3.0	blend CH <sub>3</sub> OCH <sub>3</sub>
	132.897703/-	132.90001	14(5,9)-13(5,8)	5.2/-	1.80/-	7.5/-	blend C <sub>2</sub> H <sub>3</sub> CN
		132.90001	14(5,10)-13(5,9)	5.2/-			
	132.902656/-	132.905288	14(6,8)-13(6,7)	5.9/-	1.84/-	7.0/-	blend C <sub>2</sub> H <sub>3</sub> CN
		132.905288	14(6,9)-13(6,8)	5.9/-			
	132.918375/132.918453	132.917752	14(4,11)-13(4,10)	-	-	-	blend CH <sub>3</sub> OCHO( <i>v</i> =0)
		132.918991	14(4,10)-13(4,9)	-	-	-	
	132.921359/132.920359	132.923739	14(7,7)-13(7,6)	-	-	-	blend CH <sub>3</sub> OCHO( <i>v</i> =0)
		132.923739	14(7,8)-13(7,7)	-	-	-	
	132.948594/-	132.951274	14(8,6)-13(8,5)	6.0/-	1.33/-	5.0/-	
		132.951274	14(8,7)-13(8,6)	6.0/-			
	132.957750/-	132.959401	14(3,12)-13(3,11)	3.7/-	1.59/-	6.8/-	
	132.984531/-	132.985953	14(9,5)-13(9,4)	3.2/-	0.82/-	9.2/-	
		132.985953	14(9,6)-13(9,5)	3.2/-			
	133.023672/133.023438	133.0266652	14(10,4)-13(10,3)	6.7/7.3	1.03/0.79	5.5/-	blend C <sub>2</sub> H <sub>3</sub> CN
		133.0266652	14(10,5)-13(10,4)	6.7/7.3			
	133.028328/133.027328	133.030674	14(3,11)-13(3,10)	5.3/7.5	1.68/0.47	4.8/-	blend C <sub>2</sub> H <sub>3</sub> CN
	138.392609/138.393063	138.39516	15(1,15)-14(1,14)	5.5/4.5	1.38/0.61	9.9,5.1/11.7	
	145.138625/145.137703	145.141487	15(1,14)-14(1,13)	5.9/7.8	0.98/0.89	5.6/-	
	147.557578/147.557734	147.5617015	16(1,16)-15(1,15)	8.4/8.1	1.25/0.80	5.7/-	
	151.353406/-	151.356948	16(2,15)-15(2,14)	7.0/-	1.44/-	9.4/-	blend SO <sub>2</sub>
	151.897344/151.897266	151.900284	16(5,12)-15(5,11)	5.8/6.0	2.37/0.52	17.3,5.8/4.2	
		151.900324	16(5,11)-15(5,10)	5.9/6.0			
	151.912672/151.911984	151.915868	16(7,9)-15(7,8)	-	-	-	blend <sup>34</sup> SO <sub>2</sub>
		151.915868	16(7,10)-15(7,9)				
	151.930141/151.928391	151.933608	16(4,13)-15(4,12)	6.8/10.3	1.11/0.50	5.1/-	blend C <sub>2</sub> H <sub>3</sub> CN
	151.933125/151.933203	151.9368513	16(4,12)-15(4,11)	7.4/7.2	1.82/0.94	6.8/1.0	blend CH <sub>3</sub> OCHO( <i>v</i> =0), C <sub>2</sub> H <sub>3</sub> CN
	151.940906/-	151.94455	16(8,8)-15(8,7)	7.2/-	1.20/-	5.6/-	blend CH <sub>3</sub> OCHO( <i>v</i> =0)
		151.94455	16(8,9)-15(8,8)	7.2/-			
	151.978594/-	151.9822606	16(9,7)-15(9,6)	7.2/-	1.22/-	5.3/-	blend CH <sub>3</sub> OCHO( <i>v</i> =0)
		151.9822606	16(9,8)-15(9,7)	7.2/-			
	151.982406	151.986758	16(3,14)-15(3,13)	8.6	2.10/1.10	9.9,3.0/2.8	blend CH <sub>3</sub> OCHO( <i>v</i> =0), C <sub>2</sub> H <sub>3</sub> CN
	152.024078/152.024609	152.027503	16(10,6)-15(10,5)	6.8/5.7	0.84/0.58	4.7/-	
		152.027503	16(10,7)-15(10,6)	6.8/5.7			
	152.075797/152.075500	152.0787312	16(11,5)-15(11,4), <i>F</i> =15-15	5.8/6.4	0.95/0.51	10.8/6.6	
		152.0787312	16(11,6)-15(11,5), <i>F</i> =15-15	5.8/6.4			
		152.079247	16(11,5)-15(11,4),	6.8/7.4			

Table 6. (Continued)

			$F=16-15$				
		152.079247	16(11,6)-15(11,5), $F=16-15$	6.8/7.4			
		152.079505	16(11,5)-15(11,4), $F=17-16$	7.3/7.9			
		152.079505	16(11,6)-15(11,5), $F=17-16$	7.3/7.9			
		152.079505	16(11,5)-15(11,4), $F=15-14$	7.3/7.9			
		152.079505	16(11,6)-15(11,5), $F=15-14$	7.3/7.9			
		152.0799279	16(11,5)-15(11,4), $F=16-16$	8.1/8.7			
		152.0799279	16(11,6)-15(11,5), $F=16-16$	8.1/8.7			
	152.122422/-	152.1255495	16(3,13)-15(3,12)	6.2/-	1.16/-	8.1/-	blend $\text{CH}_3\text{OCHO}(v=0)$
$\text{CH}_3\text{OCHO}$	131.911000/131.911078	131.914524	12(0,12)-11(1,11)E	8.0/7.8	1.58/1.60	2.0/2.2	blend $\text{CH}_3\text{OCH}_3$
	131.913063	131.916432	12(0,12)-11(1,11)A	7.7	1.44	2.0/1.7	blend $\text{CH}_3\text{OCHO}(v=0)$
	132.003250	132.006639	10(2,9)-9(1,8)E	7.7	0.97/0.95	2.2/1.9	blend $\text{CH}_3\text{COCH}_3$
	132.007375/132.007438	132.010774	10(2,9)-9(1,8)A	7.7/7.6	1.74/1.34	3.6/3.2	blend $\text{CH}_3\text{COCH}_3$
	132.102203/132.102063	132.105508	12(1,12)-11(1,11)E	7.5/7.8	4.53/4.26	13.6,2.6,2.8 /2.6,2.5,17.0	blend $\text{OC}^{33}\text{S}$ , $^{34}\text{SO}_2$
	132.103813/132.103891	132.107205	12(1,12)-11(1,11)A	7.7/7.5	5.42/4.47	common with above	blend $^{34}\text{SO}_2$
	132.241766	132.24243	19(6,13)-19(5,14)A	1.5	4.62/4.46	2.7,12.3,2.7 /1.9,8.0,1.5	blend $\text{CH}_3\text{OCHO}(v=0)$ , $\text{H}^{13}\text{CCCN}$
		132.244199	19(6,13)-19(5,14)E	5.5		common with above	
		132.245128	12(0,12)-11(0,11)E	7.6		common with above	
	132.243438/132.243203	132.24673	12(0,12)-11(0,11)A	7.5/8.0	5.01/4.61	common with above	blend $\text{H}^{13}\text{CCCN}$
	132.432656/132.432813	132.436113	12(1,12)-11(0,11)E	7.8/7.5	1.73/1.62	3.1/1.8	blend $\text{CH}_3\text{OCHO}(v=0)$
	132.434109	132.437494	12(1,12)-11(0,11)A	7.7	1.55/1.78	1.8/1.8	blend $\text{CH}_3\text{OCHO}(v=0)$
	132.499719	132.503091	19(5,15)-19(4,16)E	7.6	0.76/0.74	2.1/1.8	
	132.533672/132.533750	132.537122	19(5,15)-19(4,16)A	7.8/7.6	0.80/0.82	2.6/1.0	
	132.918609/132.918453	132.921937	11(1,10)-10(1,9)E	7.5/7.9	4.92/4.33	2.2,13.2 /2.1,8.0	blend $\text{C}_2\text{H}_3\text{CN}$
	132.925391	132.928736	11(1,10)-10(1,9)A	7.5	4.45/4.26	2.0,6.6 /1.4,4.1	blend $\text{C}_2\text{H}_3\text{CN}$
	136.276531	136.280061	11(4,8)-10(4,7)E	7.8	2.92/2.62	2.5/2.4	blend $\text{CH}_3\text{OCHO}(v=0)$
	136.278969/136.279047	136.282597	11(4,8)-10(4,7)A	8.0/7.8	2.56/2.75	3.1/2.3	blend $\text{CH}_3\text{OCHO}(v=0)$
	136.586766/136.586688	136.590238	12(1,11)-11(2,10)E	7.6/7.8	1.30/1.19	2.1/1.3	
	136.596453/136.596375	136.599952	12(1,11)-11(2,10)A	7.7/7.9	1.30/1.09	2.8/1.0	
	136.658781/136.658719	136.662168	19(4,16)-19(3,17)E	7.4/7.6	0.83/0.90	3.1/1.8	blend $\text{CH}_3\text{CCH}$
	136.711594/136.711656	136.715083	19(4,16)-19(3,17)A	7.7/7.5	1.21/0.73	0.8/2.4	blend $\text{CH}_3\text{CCH}$
	136.950328	136.953766	20(5,16)-20(4,17)E	7.5	1.41/1.26	2.3/2.0	blend $^{33}\text{SO}$
	136.987031	136.990512	20(5,16)-20(4,17)A	7.6	1.43/1.28	2.5/2.4	blend $\text{HC}_3\text{N}(v_7=1)$
	137.289703/137.289625	137.293183	11(4,7)-10(4,6)E	7.6/7.8	4.28/4.20	2.0,5.2 /0.88,2.9	
	137.304656	137.308132	18(6,12)-18(5,13)E	7.6	1.44/1.16	3.1/2.8	
		137.308622	18(6,12)-18(5,13)A	8.7			
	137.309844/137.309766	137.31333	11(4,7)-10(4,6)A	7.6/7.8	4.38/4.00	1.1,4.2	

Table 6. (Continued)

					/1.9,7.1	
138.662625/138.662859	138.665944	27(5,22)-27(4,23)E	7.2/6.7	1.13/0.56	2.4/2.6	
146.010859/146.010250	146.014526	4(4,0)-3(3,0)E	7.5/8.8	1.64/1.67	4.9/3.1	blend
	146.015063	4(4,1)-3(3,0)A	8.6/9.9			CH <sub>3</sub> OCHO( <i>v</i> =0)
146.018797/146.018641	146.023024	4(4,0)-3(3,1)A	8.7/9.0	1.69/1.25	4.2/4.8	blend
						CH <sub>3</sub> OCHO( <i>v</i> =0)
146.588141/146.588219	146.59242	31(6,25)-31(5,26)A	8.8/8.6	3.08/1.81	-/2.4	blend SO <sub>2</sub> ,
						CH <sub>3</sub> OCHO( <i>v</i> <sub>18</sub> =1),
						CH <sub>3</sub> OCH <sub>3</sub>
146.695109/146.694953	146.699324	15(6,9)-15(5,10)A	8.6/8.9	0.94/1.29	2.5/2.0	blend
						CH <sub>3</sub> OCHO( <i>v</i> <sub>18</sub> =1)
146.744172/146.744234	146.748494	15(6,9)-15(5,10)E	8.8/8.7	0.58/0.98	-/2.1	
146.973281	146.977678	12(3,10)-11(3,9)E	9.0	7.40/6.99	3.1/2.4	blend CS,
						CH <sub>3</sub> OCHO( <i>v</i> <sub>18</sub> =1)
146.983891/146.983672	146.988047	12(3,10)-11(3,9)A	8.5/8.9	4.24/4.80	0.90,4.7	
					/1.1,3.8	
147.243766/147.243609	147.247965	18(6,13)-18(5,14)E	8.5/8.9	1.86/1.82	5.9,3.4	blend
					/8.8,0.96	CH <sub>3</sub> OCHO( <i>v</i> <sub>18</sub> =1)
147.245297/147.246656	147.250781	12(11,1)-11(11,0)E	-	-	-	blend
						CH <sub>3</sub> OCHO( <i>v</i> <sub>18</sub> =1)
147.250859/147.251469	147.2556572	12(11,2)-11(11,1)A	9.8/8.5	1.19/1.47	3.5/2.2	
	147.255682	12(11,1)-11(11,0)A	9.8/8.6			
147.261078	147.265314	12(11,2)-11(11,1)E	8.6	1.08/1.25	3.8/1.6	
147.276578/147.276875	147.28099	18(6,13)-18(5,14)A	9.0/8.4	0.99/0.98	2.1/1.8	
147.300531/147.300609	147.304789	19(6,14)-19(5,15)E	8.7/8.5	0.98/1.26	2.8/1.7	
147.306250	147.31057	12(10,2)-11(10,1)E	8.8	1.45/1.29	2.5/1.3	
147.313578/147.313500	147.31775	12(10,2)-11(10,1)A	8.5/8.6	2.51/2.70	2.0/1.4	
147.321125/147.321203	147.325392	12(10,3)-11(10,2)E	8.7/8.5	1.84/1.52	3.0/2.5	blend U-34
147.327469/147.327547	147.331633	19(6,14)-19(5,15)A	8.5/8.3	0.97/0.91	5.7/2.2	blend U-34
147.392844/147.392781	147.397073	12(9,3)-11(9,2)E	8.6/8.7	3.08/2.39	3.6/3.1	blend CH <sub>3</sub> OH
147.402156/147.401938	147.406369	12(9,3)-11(9,2)A	8.6/9.0	2.20/2.24	3.3/2.7	
147.407578/147.407500	147.411819	12(9,4)-11(9,3)E	8.6/8.8	1.45/1.86	4.3/2.3	
147.520188/147.519969	147.524311	12(8,4)-11(8,3)E	8.4/8.8	1.53/1.87	2.3/2.1	
147.531406/147.531328	147.535539	12(8,5)-11(8,4)A	8.4/8.6	2.00/2.40	3.2/2.7	blend
	147.5355507	12(8,4)-11(8,3)A	8.4/8.6			CH <sub>3</sub> OCHO( <i>v</i> =0)
147.534766/147.534313	147.538644	12(8,5)-11(8,4)E	7.9/8.8	1.75/1.85	3.5/2.5	blend
						CH <sub>3</sub> OCHO( <i>v</i> =0)
	147.539172	17(6,12)-17(5,13)E	9.0/9.9			
147.581313/147.581000	147.585206	17(6,12)-17(5,13)A	7.9/8.5	0.80	1.7/2.8	
-/149.919969	149.924426	13(6,8)-13(5,9)E	-/8.9	-/0.69	-/1.3	
150.065625/150.065781	150.070143	13(6,8)-13(5,9)A	9.0/8.7	1.01/0.84	2.3/2.4	
150.386078	150.390454	12(6,6)-12(5,7)A	8.7	1.67/1.15	2.0/1.4	blend SO <sub>2</sub>
150.395313/150.395234	150.399678	24(7,17)-24(6,18)E	8.7/8.9	0.98/0.89	1.9/0.58	blend CH <sub>3</sub> COCH <sub>3</sub>
150.444906	150.449202	12(6,6)-12(5,7)E	8.6	1.21/0.92	2.3/1.8	blend X-17
150.596359	150.600762	12(4,8)-11(4,7)E	8.8	5.14/3.69	5.2,1.6	
					/1.9,7.4	
150.613844	150.618303	12(4,8)-11(4,7)A	8.9	5.10/3.76	2.1,6.5	
					/0.96,2.8	
150.632375	150.63674	12(6,7)-12(5,8)A	8.7	1.33	6.1/3.2	
150.682578/150.682438	150.685347	31(8,23)-31(7,24)A	5.5/5.8	0.72/0.53	4.0/3.5	blend CH <sub>3</sub> COCH <sub>3</sub>
150.734016/150.733781	150.738141	31(8,23)-31(7,24)E	8.2/8.7	0.68/0.52	3.6/-	
150.782313/150.781922	150.786711	19(2,17)-19(2,18)A	8.7/9.5	0.64/0.57	1.7/1.5	
150.851578/150.851516	150.855977	19(2,17)-19(1,18)E	8.7/8.9	0.77	2.8/1.5	blend c-C <sub>3</sub> H <sub>2</sub>
150.925828	150.930193	19(2,17)-19(1,18)A	8.7	0.77/0.52	2.4/3.4	
150.952906/-	150.957157	22(6,17)-22(5,18)E	8.4/-	0.79/-	2.1/-	
150.976406	150.980775	22(6,17)-22(5,18)A	8.7	1.42/0.84	0.55/2.7	blend U-41
151.004563	151.009041	11(6,6)-11(5,7)E	8.9	1.38/1.39	2.4/2.0	
151.031656	151.035991	11(6,5)-11(5,6)E	8.6	1.16/0.94	3.2/0.7	
151.108938	151.113186	11(6,6)-11(5,7)A	8.4	1.21/1.04	1.9/1.3	
151.408719	151.413078	10(6,5)-10(5,6)E	8.6	1.27/1.11	2.3/1.2	

Table 6. (Continued)

	151.451906	151.456198	10(6,4)-10(5,5)A	8.5	1.18/0.98	1.1/1.2	blend CH <sub>3</sub> OCHO( <i>v</i> =0)
	151.453438/151.453578	151.457804	10(6,4)-10(5,5)E	8.6/8.4	1.21/0.74	1.5/1.1	blend CH <sub>3</sub> OCHO( <i>v</i> =0)
	151.491578/151.491734	151.496105	10(6,5)-10(5,6)A	9.0/8.6	0.77/0.92	2.2/2.4	
	151.713313/151.713156	151.717477	9(6,4)-9(5,5)E	8.2/8.5	0.92/0.99	2.3/1.2	
	151.761141/151.761063	151.765554	9(6,3)-9(5,4)E	8.7/8.9	0.82/0.63	3.2/1.2	blend U-45
	151.772750	151.777093	9(6,3)-9(5,4)A	8.6	0.86/0.53	2.9/3.2	
	151.786250/151.786172	151.790613	9(6,4)-9(5,5)A	8.6/8.8	1.09/1.08	1.6/1.2	
	151.933125/151.933203	151.937471	8(6,3)-8(5,4)E	8.6/8.4	1.82/0.94	6.8/1.0	blend C <sub>2</sub> H <sub>3</sub> CN
	151.945719/151.945641	151.9500159	13(2,12)-12(2,11)E	8.5/8.6	5.34/3.93	2.0,5.8 /2.8,0.78	
		151.9500751	17(14,3)-18(13,6)A	8.6/8.7			
		151.950079	13(2,12)-12(2,11)E	8.6/8.8			
		151.9502357	17(14,3)-18(13,6)A	8.9/9.1			
		151.9502357	17(14,4)-18(13,5)A	8.9/9.1			
	151.952203/151.952047	151.956555	13(2,12)-12(2,11)A	8.6/8.9	5.15/3.58	5.3,2.1 /3.3,1.3	
	151.982406	151.9866726	8(6,2)-8(5,3)E	8.4	2.10/1.10	9.9,3.0/2.8	blend C <sub>2</sub> H <sub>3</sub> CN
	151.999422/151.998891	152.003958	8(6,2)-8(5,3)A	8.9/10.0	1.00/0.76	2.8/4.2	blend CH <sub>3</sub> OCHO( <i>v</i> =0)
	152.003547	152.007835	8(6,3)-8(5,4)A	8.5	0.77/0.64	3.0/1.1	blend CH <sub>3</sub> OCHO( <i>v</i> =0)
	-/152.086109	152.090375	7(6,2)-7(5,3)E	-/8.4	-/0.56	-/1.3	
	152.112953/-	152.118747	17(1,16)-17(0,17)E	11.4/-	1.04/-	8.1/-	blend C <sub>2</sub> H <sub>3</sub> CN
	152.156609/152.155609	152.15992	7(6,1)-7(5,2)A	6.5/8.5	0.91/0.56	3.5/4.6	
	152.191781/152.192234	152.196627	17(1,16)-17(0,17)A	9.5/8.7	0.67/0.54	2.4/1.4	
CH <sub>3</sub> OCHO ( <i>v</i> <sub>18</sub> =1)	131.452219/131.452375	131.455648	12(1,12)-11(1,11)E	7.8/7.5	1.00/1.06	2.5/2.4	
	131.608938	131.612329	12(0,12)-11(0,11)E	7.7	1.24/0.98	3.2/2.9	
	132.060016	132.063465	11(1,10)-10(1,9)A	7.8	1.58/1.48	2.2/1.0	
	132.375203/132.375281	132.378703	11(1,10)-10(1,9)E	7.9/7.7	1.16/1.03	2.4/3.0	
		132.379528	5(3,2)-4(2,2)E	9.8/9.6	1.16/1.03	2.4/3.0	
	133.797422/133.797266	133.800739	11(3,9)-10(3,8)A	7.4/7.8	1.91/1.27	1.8/2.5	blend X-5
	145.617016/145.616781	145.621125	12(3,10)-11(3,9)A	8.5/8.9	1.71/1.64	2.7/1.7	
	146.101813/146.102047	146.106252	12(8,4)-11(8,3)E	9.1/8.6	0.93/1.47	1.3/0.94	
	146.148047/146.148734	146.1528653	20(4,17)-20(2,18)E	9.9/8.5	0.75/0.89	1.1/0.83	blend CH <sub>3</sub> OCH <sub>3</sub>
		146.152945	12(10,2)-11(10,1)A	10.0/8.6	0.75/0.89	1.1/0.83	blend CH <sub>3</sub> OCH <sub>3</sub>
	146.170859/146.170781	146.174997	12(9,3)-11(9,2)A	8.5/8.6	1.08/0.99	2.2/1.8	
	146.230453/146.230750	146.234988	12(8,5)-11(8,4)A	9.3/8.7	1.07/1.36	3.4/1.8	
	146.333766/146.333828	146.337965	12(7,5)-11(7,4)E	8.6/8.5	1.28/0.82	1.7/2.9	blend U-32
	146.341156	146.345423	12(3,10)-11(3,9)E	8.7	1.43/1.48	2.4/2.3	
	146.353297/146.353141	146.356286	12(11,2)-11(11,1)E	6.1/6.4	2.40/1.16	3.1/3.0	
		146.357492	12(7,6)-11(7,5)A	8.6/8.9	2.40/1.16	3.1/3.0	
	146.583484/146.584094	146.587525	12(6,7)-11(6,6)A	8.3/7.0	1.30/1.31	3.7/1.7	blend SO <sub>2</sub> CH <sub>3</sub> OCH <sub>3</sub>
	146.677938/146.678094	146.682383	12(6,6)-11(6,5)E	9.1/8.8	0.97/1.28	2.7/1.5	blend CH <sub>3</sub> OCH <sub>3</sub>
	147.197688/147.197750	147.201768	12(6,7)-11(6,6)E	8.3/8.2	1.90/2.15	3.1/2.4	blend CH <sub>3</sub> OCH <sub>3</sub>
	147.243766/147.243609	147.247965	12(5,7)-11(5,6)E	8.5/8.9	1.86/1.82	5.9,3.4 /8.8,0.96	blend CH <sub>3</sub> OCHO( <i>v</i> =0)
	147.244750/147.244688	147.248992	12(4,9)-11(4,8)A	-	-	-	blend CH <sub>3</sub> OCHO( <i>v</i> =0)
	150.893938/150.894000	150.898356	13(2,12)-12(2,11)A	8.8/8.7	2.12/1.69	2.5/1.9	
	151.188828/151.188906	151.193305	13(2,12)-12(2,11)E	8.9/8.7	2.01/1.37	3.6/3.0	
	152.080297	152.0847	12(2,10)-11(2,9)A	8.7	1.89/1.20	2.2/1.4	blend C <sub>2</sub> H <sub>3</sub> CN
CH <sub>3</sub> OCHO ( <i>v</i> <sub>t</sub> =2)	137.167172/-	137.170769	11(4,8)-10(4,7)A	7.9/-	0.60/-	2.6/-	
	152.182547/152.182922	152.186983	13(2,12)-12(2,11)A	8.7/8.0	0.66/0.59	7.0/3.8	
C <sub>2</sub> H <sub>5</sub> CN	133.127750/133.128969	133.129943	16(0,16)-15(1,15)	4.9/2.2	0.72/0.67	15.1/-	
	133.544406/133.544031	133.546584	15(2,14)-14(2,13)	4.9/5.7	4.47/1.37	14.9,4.2/16.4	
	136.538766/136.538234	136.54127	15(1,14)-14(1,13)	5.5/6.7	3.91/0.99	15.5,4.6/12.6	
	136.819938/136.821078	136.8224	15(2,13)-14(2,12)	5.4/2.9	4.15/1.00	15.7,4.7/15.9	

Table 6. (Continued)

	137.084078/-	137.08675	28(4,24)-28(3,25)	5.8/-	0.68/-	8.7/-	
	137.108719/-	137.10987	15(1,15)-14(0,14)	2.5/-	0.80/-	11.8/5.4	
	137.320984/137.321906	137.324865	23(2,22)-23(1,23)	-	-	-	blend HC <sub>3</sub> N( $v_7=2$ )
	137.919250/137.919703	137.92213	19(1,18)-18(2,17)	6.3/5.3	0.64/0.60	12.8/10.9	
	138.348969/138.350719	138.35105	16(1,16)-15(1,15)	4.5/0.7	4.47/1.08	15.8,4.7/14.2	
	145.415203/145.414672	145.41801	16(1,15)-15(1,14)	5.8/6.9	4.71/1.92	15.9,4.8	
						/17.2,3.1	
	145.745813/-	145.74911	25(4,21)-25(3,22)	6.8/-	1.00/-	4.2/-	blend C <sup>33</sup> S
	146.116922/146.117984	146.12004	16(2,14)-15(2,13)	6.4/4.2	5.06/1.80	4.3,17.8/14.7	blend HC <sub>3</sub> N( $v_7=1$ )
	146.891109	146.894524	17(1,17)-16(1,16)	7.0	4.89/1.85	14.1,3.4/17.2	
	150.605516/150.605594	150.6068	23(4,19)-23(3,20)	2.6/2.4	0.71/0.56	3.0/1.9	
	151.124438/151.123203	151.127264	17(2,16)-16(2,15)	5.6/8.1	4.63/1.10	15.7,3.9/12.8	
	151.809594/-	151.81285	18(0,18)-17(1,17)	6.4/-	1.00/-	12.7/-	
	152.295766/152.295313	152.297825	17(8,9)-16(8,8)	4.1/4.9	3.88/0.95	5.1/7.2	blend C <sub>2</sub> H <sub>5</sub> CN
	152.301031/152.302406	152.303789	17(7,11)-16(7,10)	5.4/2.7	6.50/1.11	6.8,23.5/19.4	blend C <sub>2</sub> H <sub>5</sub> CN
		152.304641	17(9,8)-16(9,7)	7.1/4.4	6.50/1.11		
	152.317438/152.317906	152.320522	17(10,7)-16(10,6)	6.1/5.1	2.35/0.67	9.6/13.0	blend C <sub>2</sub> H <sub>5</sub> CN
	152.326219/152.325906	152.329886	17(6,12)-16(6,11)	7.2/7.8	3.87/0.83	18.8,4.4/11.3	blend C <sub>2</sub> H <sub>5</sub> CN
	152.340250/152.340328	152.343334	17(11,6)-16(11,5)	6.1/5.9	1.80/0.63	8.1/6.7	
	152.370469/152.370313	152.371939	17(12,5)-16(12,4)	2.9/3.2	3.71/1.61	3.4,9.4/5.3	blend U-49
	152.389391/152.389703	152.3913	17(5,13)-16(5,12)	3.8/3.1	3.40/0.88	14.3,5.0/11.4	
		152.392415	17(5,12)-16(5,11)	5.9/5.3	3.40/0.88	14.3,5.0/11.4	
CH <sub>3</sub> OCH <sub>3</sub>	131.903672/131.903609	131.9071431	15(1,14)-15(0,15)AE	7.9/8.0	1.67/2.06	2.5/2.0	
		131.9071435	15(1,14)-15(0,15)EA	7.9/8.0			
	131.906203	131.9096032	15(1,14)-15(0,15)EE	7.7	2.53/2.71	2.0/2.0	
	131.908641	131.9120632	15(1,14)-15(0,15)AA	7.8	1.76/2.06	2.3/1.7	blend CH <sub>3</sub> OCHO( $v=0$ )
	132.521859/132.521781	132.5247788	8(0,8)-7(1,7)AA	6.6/6.8	5.83/6.38	7.9,3.0	blend C <sub>2</sub> H <sub>3</sub> CN
						/8.5,3.0	
		132.5252393	8(0,8)-7(1,7)EE	7.6/7.8			
		132.5256994	8(0,8)-7(1,7)AE	8.7/8.9			
		132.5257001	8(0,8)-7(1,7)EA	8.7/8.9			
	132.975000	132.97761	34(7,28)-35(0,35)EA	5.9	1.19/1.16	1.2/2.0	
		132.9776411	34(7,28)-35(0,35)AE	6.0			
		132.9785673	18(3,16)-17(4,13)EE	8.0			
	133.261953	133.2653105	11(3,8)-11(2,9)AE	7.6	2.82/3.16	1.8/1.8	
		133.2653487	11(3,8)-11(2,9)EA	7.6			
	133.264859	133.2683191	11(3,8)-11(2,9)EE	7.8	4.04/4.25	2.2/1.8	
	133.267906/133.267750	133.2713086	11(3,8)-11(2,9)AA	7.7/8.0	3.00/3.20	3.0/1.9	
	133.310781/133.310859	133.3135771	24(3,21)-24(2,22)EE	6.3/6.1	1.58/1.62	6.3/4.5	
		133.3147226	24(3,21)-24(2,22)AA	8.9/8.7			
	136.619422/136.619500	136.6229215	10(3,7)-10(2,8)AE	7.7/7.5	2.61/2.21	1.4/1.3	blend SO
		136.6229926	10(3,7)-10(2,8)EA	7.8/7.7			
	136.622625/136.622469	136.6260716	10(3,7)-10(2,8)EE	7.6/7.9	5.43/4.90	2.1/1.8	blend SO
	136.625672/136.625594	136.6291861	10(3,7)-10(2,8)AA	7.7/7.9	5.57/3.89	2.6/1.2	blend SO
	137.374938/137.375000	137.3784982	20(2,18)-20(1,19)AE	7.8/7.6	1.20/1.15	2.3/2.1	blend H <sub>2</sub> CS
	137.376844/137.376688	137.3804028	20(2,18)-20(1,19)EE	7.8/8.1	2.32/2.56	2.0/1.7	blend H <sub>2</sub> CS
	137.378750/137.378359	137.3823075	20(2,18)-20(1,19)AA	7.8/8.6	2.28/2.32	2.5/2.1	blend H <sub>2</sub> CS
	137.578953	137.5823391	17(3,14)-16(4,13)AA	7.4	0.69/0.76	3.0/1.5	
	137.581625	137.5849649	17(3,14)-16(4,13)EE	7.3	1.46/1.17	2.1/1.3	
	137.584219/137.584141	137.5875691	17(3,14)-16(4,13)AE	7.3/7.5	0.88/0.85	1.7/1.3	
		137.5876125	17(3,14)-16(4,13)EA	7.4/7.6			
	145.540031	145.544368	16(1,15)-16(0,16)AE	8.9	0.79/1.23	-/1.5	blend HC <sub>3</sub> N( $v=0$ )
		145.5444822	16(1,15)-16(0,16)AE	9.2			
		145.5444826	16(1,15)-16(0,16)EA	9.2			
	145.542859/145.542781	145.547165	16(1,15)-16(0,16)EE	8.9/9.0	1.84/2.65	2.0/1.6	blend HC <sub>3</sub> N( $v=0$ )
		145.5472034	16(1,15)-16(0,16)EE	8.9/9.1			
	145.545984/145.545453	145.5499245	16(1,15)-16(0,16)AA	8.1/9.2	1.39/1.72	6.1/1.9	blend HC <sub>3</sub> N( $v=0$ )
		145.549962	16(1,15)-16(0,16)AA	8.2/9.3			
	145.671484/145.671344	145.675602	5(3,2)-5(2,3)AE	8.5/8.8	1.50/1.93	1.8/1.7	

Table 6. (Continued)

	145.6756179	5(3,2)-5(2,3)AE	8.5/8.8			
145.676000/145.676063	145.67992	5(3,2)-5(2,3)EA	8.1/7.9	3.08/3.98	2.7/2.2	
	145.679936	5(3,3)-5(2,3)EA	8.1/8.0			
	145.6803779	5(3,2)-5(2,3)EE	9.0/8.9			
	145.680397	5(3,2)-5(2,3)EE	9.0/8.9			
145.678359/145.678281	145.6826427	5(3,2)-5(2,3)AA	8.8/9.0	2.02/2.78	2.8/1.9	
	145.682677	5(3,2)-5(2,3)AA	8.9/9.0			
146.150875	146.155157	4(3,2)-4(2,2)EE	8.8	1.28/1.43	2.1/2.5	blend CH <sub>3</sub> OH
	146.1551727	4(3,2)-4(2,2)EE	8.8			
-/146.155141	146.15944	4(3,1)-4(2,2)AE	8.5/8.8	-/0.79	-/1.4	blend CH <sub>3</sub> OH
	146.15946	4(3,1)-4(2,2)AE	8.5/8.9			
146.162469/146.161938	146.1662056	4(3,1)-4(2,2)EE	7.7/8.8	2.04/3.32	2.7/2.3	
	146.166246	4(3,1)-4(2,2)EE	7.7/8.8			
	146.1665605	4(3,1)-4(2,2)AA	8.4/9.5			
	146.166606	4(3,1)-4(2,2)AA	8.5/9.6			
	146.1673419	4(3,1)-4(2,2)EA	10.0/11.1			
	146.167381	4(3,2)-4(2,2)EA	10.1/11.2			
146.401047/146.400750	146.405165	3(3,1)-3(2,1)EE	8.4/9.0	0.99/1.39	1.6/1.0	
	146.4051889	3(3,1)-3(2,1)EE	8.5/9.1			
146.402500/-	146.407078	3(3,0)-3(2,1)AE	9.4/-	0.82/-	2.8/-	
	146.4071003	3(3,0)-3(2,1)AE	9.4			
146.410359/146.409984	146.4142596	3(3,0)-3(2,1)AA	8.0/8.8	1.19/1.51	5.2/1.5	blend CH <sub>3</sub> OCH <sub>3</sub>
	146.414314	3(3,0)-3(2,1)AA	8.1/8.9			
146.410359/146.410891	146.4153293	3(3,0)-3(2,1)EE	10.2/9.1	1.19/1.30	0.43,1.4	blend CH <sub>3</sub> OCH <sub>3</sub>
	146.415382	3(3,0)-3(2,1)EE	10.3/9.2			
	146.4165244	3(3,0)-3(2,1)EA	12.6/11.5			
	146.416572	3(3,1)-3(2,1)EA	12.7/11.6			
146.575859/146.575703	146.580107	3(3,1)-3(2,2)EE	8.7/9.0	0.97/1.43	2.4/3.5	
	146.5801265	3(3,1)-3(2,2)EE	8.7/9.0			
	146.581174	3(3,1)-3(2,2)AE	10.9/11.2			
	146.5811959	3(3,1)-3(2,2)AE	10.9/11.2			
146.583484/146.584094	146.5883559	3(3,1)-3(2,2)AA	10.0/8.7	1.30/1.31	3.7/1.7	blend SO <sub>2</sub> , CH <sub>3</sub> OCHO( <i>v</i> <sub>18</sub> =1)
	146.588412	3(3,1)-3(2,2)AA	10.1/8.8			
-/146.585922	146.590267	3(3,0)-3(2,2)EE	-/8.9	-/1.51	-/1.6	blend SO <sub>2</sub> , CH <sub>3</sub> OCHO( <i>v</i> =0, <i>v</i> <sub>18</sub> =1)
	146.590323	3(3,0)-3(2,2)EE	5.6/9.0	1.94/1.51	-/1.6	
146.673672/146.673281	146.677588	4(3,2)-4(2,3)AE	8.0/8.8	2.04/2.80	2.9/2.1	
	146.6776074	4(3,2)-4(2,3)AE	8.0/8.8			
	146.677951	4(3,2)-4(2,3)EE	8.7/9.5			
	146.6779635	4(3,2)-4(2,3)EE	8.8/9.6			
146.680453	146.6847103	4(3,2)-4(2,3)AA	8.7	1.58/2.52	2.8/1.7	blend CH <sub>3</sub> OCHO( <i>v</i> <sub>18</sub> =1)
	146.684759	4(3,2)-4(2,3)AA	8.8			
146.684953	146.6889964	4(3,1)-4(2,3)EE	8.3	0.84/0.98	2.9/1.7	
	146.68904	4(3,1)-4(2,3)EE	8.4			
146.697859/146.697703	146.702061	3(2,1)-2(1,2)AE	8.6/8.9	1.52/2.22	2.3/1.6	blend CH <sub>3</sub> OCHO( <i>v</i> =0)
	146.7020756	3(2,1)-2(1,2)AE	8.6/8.9			
	146.702446	3(2,1)-2(1,2)EA	9.4/9.7			
	146.7024544	3(2,1)-2(1,2)EA	9.4/9.7			
146.700516/146.700297	146.7047162	3(2,1)-2(1,2)EE	8.6/9.0	2.20/3.12	1.6/2.0	
	146.704743	3(2,1)-2(1,2)EE	8.6/9.1			
146.702969/146.702891	146.7071671	3(2,1)-2(1,2)AA	8.6/8.7	1.50/2.02	2.1/2.0	
	146.707233	3(2,1)-2(1,2)AA	8.7/8.9			
146.861734/146.861594	146.865928	5(3,2)-5(2,4)EA	8.6/8.8	0.85/1.31	3.3/1.9	
	146.8659748	5(3,3)-5(2,4)EA	8.7/8.9			
146.868219	146.8725451	5(3,3)-5(2,4)EE	8.8	2.78/3.60	2.2,5.8	

Table 6. (Continued)

						1.7,7.3	
	146.872547	5(3,3)-5(2,4)EE	8.8				
146.873031/146.872953	146.8773085	5(3,3)-5(2,4)AA	8.7/8.9	1.17/1.99	2.7/1.4		
	146.877349	5(3,3)-5(2,4)AA	8.8/9.0				
147.020516	147.024205	7(1,7)-6(0,6)EA	7.5	4.63/6.29	4.4/3.8,2.0		
	147.024206	7(1,7)-6(0,6)AE	7.5				
	147.0248967	7(1,7)-6(0,6)EE	8.9				
	147.024902	7(1,7)-6(0,6)EE	8.9				
	147.0255949	7(1,7)-6(0,6)AA	10.4				
	147.025599	7(1,7)-6(0,6)AA	10.4				
147.199438/147.199359	147.203752	6(3,4)-6(2,5)AE	8.8/8.9	1.47/2.07	1.6/2.0		blend
	147.2037627	6(3,4)-6(2,5)AE	8.8/9.0				CH <sub>3</sub> OCHO( <i>v</i> <sub>18</sub> =1)
	147.2038037	46(12,35)-	8.9/9.1				
		45(13,33)EE					
147.202484	147.2068019	46(12,34)-	8.8	2.83/4.06	2.5/1.5		
		45(13,32)EE					
	147.2068073	6(3,4)-6(2,5)EE	8.8				
	147.206816	6(3,4)-6(2,5)EE	8.8				
	147.2074288	46(12,35)-	10.1				
		45(13,33)EA					
147.206453/147.206297	147.210399	46(12,35)-	8.0/8.4	1.92/2.53	2.6/2.0		
		45(13,32)AE					
	147.2104546	46(12,34)-	8.1/8.5				
		45(13,33)AE					
	147.2107089	6(3,4)-6(2,5)AA	8.7/9.0				
	147.21074	6(3,4)-6(2,5)AA	8.7/9.0				
150.159328/150.159094	150.1625706	25(4,21)-25(1,24)AE	6.5/6.9	2.11/1.73	3.8/2.7		
	150.1625707	25(4,21)-25(1,24)EA	6.5/6.9				
	150.1628123	25(4,21)-25(1,24)EE	7.0/7.4				
	150.1630537	25(4,21)-25(1,24)AA	7.4/7.9				
150.587969/150.587750	150.5923227	21(2,19)-21(1,20)AE	8.7/9.1	1.58/1.22	1.7/1.9		blend CH <sub>3</sub> OCH <sub>3</sub>
	150.5923228	21(2,19)-21(1,20)EA	8.7/9.1				
150.589797	150.594406	21(2,19)-21(1,20)EE	9.2	2.26/1.75	2.3/1.6		blend CH <sub>3</sub> OCH <sub>3</sub>
150.591641/150.591563	150.5964893	21(2,19)-21(1,20)AA	9.7/9.8	1.81/1.24	1.5/1.1		blend CH <sub>3</sub> OCH <sub>3</sub>
150.873859/150.873719	150.8758548	21(2,20)-20(3,17)AA	4.0/4.2	0.73/0.66	2.1/3.5		blend CH <sub>3</sub> OH
150.987703/150.987625	150.9920974	10(3,8)-10(2,9)EA	8.7/8.9	2.86/3.19	2.2/1.5		blend U-41
	150.9921683	10(3,8)-10(2,9)AE	8.9/9.0				
150.990984/150.990906	150.995391	10(3,8)-10(2,9)EE	8.7/8.9	4.36/4.42	2.1/1.7		
150.994188	150.9986491	10(3,8)-10(2,9)AA	8.9	3.22/3.27	2.1/1.5		
151.507063/151.506688	151.5110971	14(2,12)-13(3,11)AA	8.0/8.7	0.98/1.09	3.6/1.4		
151.509125	151.51348	14(2,12)-13(3,11)EE	8.6	2.24/2.03	1.7/1.6		
151.511500	151.5158562	14(2,12)-13(3,11)AE	8.6	1.20/0.98	1.8/1.4		
	151.5158698	14(2,12)-13(3,11)EA	8.6				
151.586266/151.586344	151.5907862	14(2,13)-14(1,14)EA	8.9/8.8	2.54/2.47	2.3/2.0		
151.586266/151.586344	151.5907867	14(2,13)-14(1,14)AE	8.9/8.8	2.54/2.47	2.3/2.0		
151.589625/151.589547	151.5939197	14(2,13)-14(1,14)EE	8.5/8.6	3.54/3.05	2.0/1.7		
151.592672	151.597053	14(2,13)-14(1,14)AA	8.7	2.52/2.25	1.9/1.6		
CH <sub>3</sub> COCH <sub>3</sub>	131.999656/131.999359	132.0032346	13(0,13)-12(1,12)AE	8.1/8.8	0.71/0.63	4.0/-	
		132.0032346	13(1,13)-12(0,12)AE	8.1/8.8			
		132.0032794	13(0,13)-12(1,12)EA	8.2/8.9			
		132.0032794	13(1,13)-12(0,12)EA	8.2/8.9			
132.007375/132.007438	132.0105977	13(1,13)-12(0,12)EE	7.3/7.2	1.74/1.34	2.2/1.9		blend
							CH <sub>3</sub> OCHO( <i>v</i> =0)
	132.0105977	13(0,13)-12(1,12)EE	7.3/7.2				
132.014391/-	132.0178755	13(1,13)-12(0,12)AA	7.9/-	0.73/-	7.2/-		
	132.0178755	13(0,13)-12(1,12)AA	7.9/5.9				
138.572063/-	138.5760885	11(3,8)-10(4,7)EE	8.7/-	0.53/-	4.2/-		
138.589375/-	138.5931203	11(4,8)-10(3,7)EE	8.1/-	0.56/-	3.3/-		
150.395313/150.395234	150.3992893	24(7,17)-24(6,18)AA	7.9/8.1	0.98/0.89	1.9/0.38		blend
							CH <sub>3</sub> OCHO( <i>v</i> =0)

Table 6. (Continued)

150.507328/150.506719	150.3992894	24(8,17)-24(7,18)AA	7.9/8.1	1.05/0.55	-	blend H <sub>2</sub> CO
	150.5112514	14(1,13)-13(2,12)AE	7.8/9.0			
	150.5112515	14(2,13)-13(1,12)AE	7.8/9.0			
	150.5113151	14(2,13)-13(1,12)EA	7.9/9.2			
150.530219/150.530297	150.5113151	14(1,13)-13(2,12)EA	7.9/9.2	1.62/0.86	3.7/2.6	blend U-39
	150.5346294	14(2,13)-13(1,12)EE	8.8/8.6			
	150.5346294	14(1,13)-13(2,12)EE	8.8/8.6			
	150.5579044	14(1,13)-13(2,12)AA	9.4/-			
150.553172/-	150.5579044	14(2,13)-13(1,12)AA	9.4	0.86/-	5.1/-	blend CH <sub>3</sub> OCHO( <i>v</i> =0)
	150.682578/150.682438	150.6869086	23(7,17)-23(6,18)EE			
151.634719/151.635094	150.6869086	23(6,17)-23(5,18)EE	8.6/8.9	0.89/0.60	3.7/2.7	
	151.6394264	15(1,15)-14(0,14)AE	9.3/8.6			
	151.6394264	15(0,15)-14(1,14)AE	9.3/8.6			
	151.6394718	15(1,15)-14(0,14)EA	9.4/8.7			
151.642500/151.642344	151.6394718	15(0,15)-14(1,14)EA	9.4/8.7	1.34/0.39	3.9/-	
	151.6465978	15(0,15)-14(0,14)EE	8.1/8.4			
	151.6465978	15(1,15)-14(0,14)EE	8.1/8.4			
	151.6465978	15(0,15)-14(1,14)EE	8.1/8.4			
151.649297/-	151.6465978	15(1,15)-14(1,14)EE	8.1/8.4	1.06/-	3.1/-	
	151.6536789	15(1,15)-14(1,14)AA	8.7/-			
	151.6536789	15(0,15)-14(0,14)AA	8.7/9.3			

Table 7. The tentative lines in this observations.

Species	Obs. freq. (HC/CR) [GHz]	Rest. freq. [GHz]	Transition	$V_{\text{LSR}}$ [km/s]	$T_{\text{a}}$ [K]	Width [km/s]	Comments
S <sup>18</sup> O	145.873984/145.873609	145.8738078	3(4)-2(3)	-0.4/0.4	1.60/0.82	10.9/9.1	blend CH <sub>3</sub> CH <sub>2</sub> CN ( <i>v</i> <sub>13</sub> / <i>v</i> <sub>21</sub> ) (Esplugues et al. 2013)
OC <sup>33</sup> S	132.097781/-	132.101384	11-10	8.2/-	0.99/-	3.4/-	blend CH <sub>3</sub> OCHO( <i>v</i> =0) CDMS (Tercero et al. 2010)
<sup>18</sup> OCS	136.905078/-	136.908755	12-11	8.1/-	0.57/-	6.5/-	(Tercero et al. 2010)
<sup>18</sup> O <sup>13</sup> CS	136.573938/-	136.5777664	12-11	8.4/-	0.96/-	10.1/-	CDMS
SiS	145.218969/145.218125	145.2269975	8-7	16.6/18.3	1.45/0.80	7.1/7.1	(Tercero et al. 2011)
o-H <sub>2</sub> C <sup>34</sup> S	137.067297/137.067453	137.0775425	4(1,3)-3(1,2)	22.4/22.1	0.58/0.63	2.8/1.6	(Tercero et al. 2010)
H <sup>13</sup> CCCN	132.243438/132.243203	132.246378	<i>J</i> =15-14, <i>F</i> =14-13	6.7/7.2	5.01/4.61	-	blend CH <sub>3</sub> OCHO( <i>v</i> =0)
H(C)OCN	151.577031/-	151.581402	16(1,16)-15(1,15)	8.6/-	0.73/-	2.7/-	
CH <sub>2</sub> DCN	138.323328/-	138.3270249	8(1,8)-7(1,7)	8.0/-	0.71/-	4.6/-	
CH <sub>3</sub> <sup>13</sup> CN	147.052859/147.052938	147.05656	8(4)-7(4)	7.5/7.4	1.35/0.91	8.0/-	blend H35α
	147.086063	147.09054	8(2)-7(2)	9.1	1.51/0.94	5.3/4.8	
CH <sub>3</sub> OH ( <i>v</i> <sub>12</sub> =1)	136.700531/136.700750	136.703454	23(4) <sup>-</sup> -24(5) <sup>-</sup>	6.4/5.9	1.19/1.46	3.8/2.2	blend CH <sub>3</sub> CCH
		136.704668	23(4) <sup>+</sup> -24(5) <sup>+</sup>	9.1/8.6	1.19/1.46	3.8/2.2	
	151.278328/151.278547	151.282794	14(-2)-15(-3)E1	8.9/8.4	4.17/1.69	5.1,2.2/3.9	
CH <sub>3</sub> <sup>18</sup> OH	137.928016/-	137.931708	3(1,3)-2(1,2)A	8.0/-	0.70/-	1.9/-	CDMS

**Table 8.** The leakage lines in this observations.\*

Label	Candidate species	Obs. freq. (HC/CR) [GHz]	Transition	Rest freq. [GHz]	Comments
X-1	CH <sub>3</sub> OCH <sub>3</sub>	131.404219/131.404531	6(1,6)-5(0,5)EA	131.4050391	DC
			6(1,6)-5(0,5)AE	131.4050401	DC
			6(1,6)-5(0,5)EE	131.4057961	DC
X-2	HNCO	131.415891/131.415969	6(1,6)-5(1,5),F=5-5	131.3934248	DC,blend CH <sub>3</sub> NCO
			6(1,6)-5(1,5),F=5-6	131.3941370	
			6(1,6)-5(1,5),F=7-6	131.39426190	
			6(1,6)-5(1,5),F=5-4	131.39428210	
			6(1,6)-5(1,5),F=6-5	131.3942897	
			6(1,6)-5(1,5),F=6-6	131.3950019	
X-3	SO <sub>2</sub>	131.533406/131.533250	16(5,11)-17(4,14)	131.27493	DC
X-4	<sup>33</sup> SO <sub>2</sub>	131.614656	14(2,12)-14(1,13),F=29/2-31/2	131.1863884	DC
			14(2,12)-14(1,13),F=27/2-25/2	131.18660810	DC
			14(2,12)-14(1,13),F=29/2-27/2	131.1895759	DC
			14(2,12)-14(1,13),F=29/2-29/2	131.1899456	DC
			14(2,12)-14(1,13),F=27/2-27/2	131.1901653	DC
			14(2,12)-14(1,13),F=27/2-29/2	131.1905351	DC
			14(2,12)-14(1,13),F=31/2-31/2	131.19205980	DC
			14(2,12)-14(1,13),F=25/2-25/2	131.1922796	DC
			14(2,12)-14(1,13),F=31/2-29/2	131.1956171	DC
			14(2,12)-14(1,13),F=25/2-27/2	131.1958369	DC
X-5	SO <sub>2</sub>	133.805359/133.805813	8(2,6)-8(1,7)	134.004860	ADC
X-6	CH <sub>3</sub> OCHO	136.423781/136.424094	11(5,6)-10(5,5)A	135.9885	DC
X-7	<sup>13</sup> CS	138.673609/138.674000	3-2	138.739335	ADC
X-8	CH <sub>3</sub> OH	145.107797/145.107875	3(0) <sup>+</sup> -2(0) <sup>+</sup> ,vt=0	145.103185	ADC
			3(1)-0(0)E1,vt=1	145.103185	ADC
X-9	CH <sub>3</sub> OH	145.113375/145.113594	3(-1)-2(-1)E2,vt=0	145.097435	ADC
			3(1)--(0)E1,vt=1	145.097435	ADC
X-10	CH <sub>3</sub> OH	145.117188/145.117344	3(0)-2(0)E1,vt=0	145.093754	ADC
			3(0)-0(0)E1,vt=1	145.093754	ADC
X-11	OCS	145.224688/145.224469	11-10	133.7859	Image
X-12	CH <sub>3</sub> OH( <i>v</i> <sub>12</sub> = 1)	147.266344/147.265734	7(1)-6(0)E1,vt=1	147.9436730	DC
			35(-9)-35(10)E1,vt=1	147.944291	DC
X-13	C <sub>2</sub> H <sub>5</sub> CN	147.452891/147.452516	17(0,17)-16(0,16)	147.7567110	DC
	CH <sub>3</sub> CN( <i>v</i> <sub>8</sub> = 1)	147.452891/147.452516	8(1)-7(-1),F=8-8,l=1	147.7591845	DC
X-14	CH <sub>3</sub> OCHO	147.479594/147.479984	28(5,23)-28(5,24)A	147.7291239	DC
			28(5,23)-28(5,24)A	147.729318	DC
			12(7,6)-11(7,5)A	147.7306066	DC
			12(7,6)-11(7,5)A	147.730607	DC
			12(7,5)-11(7,4)A	147.730751	DC
			12(7,5)-11(7,4)A	147.7307717	DC
			12(7,6)-11(7,5)E	147.731209	DC
			12(7,6)-11(7,5)E	147.731334	DC
			12(5,8)-11(5,7)E	147.728224	DC
			7(3,5)-7(2,6)EA	147.7274357	DC
			7(3,5)-7(2,6)AE	147.7280999	DC
			7(3,5)-7(2,6)EE	147.731357	DC
			7(3,5)-7(2,6)AA	147.7349473	DC
X-15	CH <sub>3</sub> OCHO	147.493406/147.493188	12(7,5)-11(7,4)E	147.717696	DC
X-16	CH <sub>3</sub> OCH <sub>3</sub>	149.935469/149.935922	5(5,0)-6(4,2)EA	149.8772306	ADC
			5(5,1)-6(4,2)AE	149.8787933	ADC
			<i>J</i> =17-16,F=16-15	149.877008	ADC
	H <sup>13</sup> CCCN	149.935469/149.935922	<i>J</i> =17-16,F=17-16	149.87700940	ADC
X-17	SO	150.433844/150.434234	4(3)-3(2)	138.1786	Image
X-18	C <sub>2</sub> H <sub>5</sub> CN	152.258531/152.258688	17(4,13)-16(4,12)	152.552899	DC

**Table 9.** The leakage lines in this observations.\*

Label	Obs. freq. (HC/CR) [GHz]	$T_a$ [K]	Width [km/s]	Label	Obs. freq. (HC/CR) [GHz]	$T_a$ [K]	Width [km/s]
U-1	131.432688/131.432453	0.93/0.84	3.3/5.5	U-26	138.136859/138.137609	0.65/0.57	1.9/2.4
U-2	131.552094/131.552172	0.89/0.65	2.7/2.6	U-27	138.204453/138.204219	0.66/0.55	1.5/1.7
U-3	131.558953/-	0.81/-	16.2/-	U-28	138.534453/-	0.60/-	2.5/-
U-4	131.563234/-	0.67/-	7.9/-	U-29	138.559547/-	1.05/-	7.5/-
U-5	131.675625/131.675234	0.74	4.0/2.0	U-30	145.302750/-	1.25/-	10.0/-
U-6	-/132.023922	-/0.62	-/1.6	U-31	145.832250/145.831797	1.03/0.92	9.8/3.1
U-7	132.042844/132.042844	0.91/1.15	4.4,9.2/4.0,4.1	U-32	146.330016/-	1.44/-	4.9/-
U-8	132.392453/132.392906	0.68/0.73	7.8/8.2	U-33*	147.109703/-	1.24/-	8.4/-
U-9	132.403891/-	0.81/-	6.2/-	U-34	147.322969/-	1.22/-	3.3/-
U-10	132.715500/-	0.72/-	4.7/-	U-35	147.508516/-	0.81/-	3.3/-
U-11	133.211438/-	0.79/-	7.6/-	U-36	147.526531/147.526141	0.78/-	3.2/3.7
U-12	133.407156/133.408219	0.78/0.70	7.5/3.1	U-37	150.464828/150.465203	0.98/0.50	4.9/2.9
U-13	133.441172/-	0.90/-	2.9/-	U-38	150.521891/150.521672	0.98/0.61	2.4/1.8
U-14	133.485438/133.485438	0.89/0.84	1.9/2.4	U-39	150.534188/150.534109	1.05/0.75	7.2/3.2
U-15	133.502375/-	1.05/-	7.2/-	U-40	150.699750/150.699672	0.96/0.64	2.6/3.8
U-16	133.642453/-	1.16/-	9.0/-	U-41	150.979922/-	1.10/-	11.3/-
U-17	133.827859/-	0.81/-	3.8/1.8	U-42	151.269094/-	1.28/-	7.5/-
U-18	-/133.858453	-/0.93	-/4.4	U-43	151.548188/151.548953	0.76/0.56	3.0/-
U-19	133.862656/133.862344	0.65/0.85	2.5/3.3	U-44	151.623047/-	0.96/-	4.8/-
U-20	136.478109/-	0.73/-	11.2/-	U-45	151.757859/-	1.01/-	4.9/-
U-21	136.753469/136.752859	0.76/0.62	3.1/5.4	U-46	152.103953/152.105250	0.87/0.51	4.2/5.3
U-22	137.044563/-	1.02/-	9.7/-	U-47 <sup>†</sup>	152.139203/152.139813	1.51/0.61	10.3/11.5
U-23	137.071344/137.070875	0.69/0.54	3.3/2.7	U-48	152.222375/-	1.04/-	4.8/-
U-24	137.432234/137.432234	0.86/0.53	2.6/0.87	U-49 <sup>†</sup>	152.362984/-	0.87/-	6.4/-
U-25	137.511891/-	0.56/-	2.7/-				

\* This line is also reported as U-line in Lee et al. (2001). <sup>†</sup> This line is also reported as U-line in Ziurys & McGonagle (1993).